A row-by-row axial turbine process model based on a one-dimensional thermofluid network approach

Prepared by:

Roelof JH Pottas

PTTROE001

Department of Mechanical Engineering

University of Cape Town

Supervised by:

Professor Pieter G Rousseau

November 2016

Submitted to the Department of Mechanical Engineering at the University of Cape Town in partial fulfilment of the academic requirements for a Master of Science degree in Mechanical Engineering.

Abstract

Keywords: axial turbine, simulation model, 1D model

Candidate: Roelof JH Pottas

Supervisor: Professor Pieter G Rousseau

Faculty: Engineering

Degree: Master of Science

Title: A row-by-row axial turbine process model based on a one-dimensional thermofluid network approach

A detailed turbine process model has been developed, based on a stage-by-stage discretisation using 1D flow elements. The complete turbine is represented by these flow elements in which the fundamental mass, energy and momentum conservation equations for compressible flow through 1D "stationary channels" and 1D "rotating channels" were solved. The required closure relations were obtained from the various loss coefficients for turbine stators, rotors and leakage flows which were characterised using correlations available in the literature. Several of the commonly applied loss calculation methods were investigated. A test case of a real turbine obtained in the literature was used to validate the model. Three models with different discretisation schemes were tested. In each of these schemes the stator and rotor flow passages were represented by a different number of elements along the radial direction. A number of hypothetical anomalies that often occur in industrial turbines were applied to the test case to demonstrate how the modelling approach can be applied in practice. The model agrees well with the test data for the nominal case and several of the off-design cases. For the nominal case the maximum deviation in total pressure of <2% occurs after the first stage and there is little variation between the results obtained with the three different models. The total enthalpy values are predicted within an accuracy of <1%, again with similar results obtained by the three different models. All three models predict the efficiency well for a broad range of relative mass flow rates. A slight improvement in the prediction of losses is observed in the models that use more elements to represent each stator and rotor passage.

Declaration

I, Roelof Johannes Hendrik Pottas, know the meaning of plagiarism and declare that all the work in the document, save for that which is properly acknowledged, is my own. This dissertation has been submitted to the Turnitin module and I confirm that my supervisor has seen my report and any concerns revealed by such have been resolved with my supervisor.

Signed by candidate

Roelof JH Pottas

2016-16-11

Acknowledgements

I sincerely thank the Lord for giving me perseverance, my wife Antoinette for her support and patience, my academic supervisor, Prof Pieter Rousseau, for his guidance and valuable time, my industrial mentor, Mr Gary de Klerk, for his advice and valuable time and the Eskom Power Plant Engineering Institute for granting me the opportunity to study.

Table of contents

List of figures

List of tables

List of nomenclature

General symbols

α	angle measured from the z-axis
β	angle in the r-θ plane
φ	angle in the z-θ plane
ψ	angle in the r-z plane
γ	ratio of specific heats
ρ	density
τ	surface forces
ω	shaft rotation speed (rps)
A	area
B	body forces
c	absolute velocity
C_p	constant pressure heat capacity
E	element number
g	gravitational acceleration
h	specific enthalpy
ΔH	enthalpy drop(stage)
m	mass

$\dot{m}$	mass flow rate
$\hat{m}$	unit direction of mass flow rate
M	Mach number
N	node number
$\hat{n}$	area normal unit vector
p	static pressure
p_0	total/stagnation pressure
$\dot{Q}$	rate of heat transfer
r	radial distance
Re	Reynolds number
s	specific entropy
$\hat{s}$	fluid vector parallel to flow path
t	time
T	temperature (K)
T_0	total/stagnation temperature
u	specific internal energy
U	blade tangential velocity
v	relative velocity
$\forall$	volume
$\dot{W}$	rate of work done

t/c	thickness/chord ratio
X	change in specific angular momentum
Y_{loss}	pressure loss coefficient

Subscripts

L	loss
0	total/stagnation property
in	inlet value
avg	average value
out	outlet value
abs	absolute value
rel	relative value
θ	tangential direction
z	z-direction
r	r-direction
o	refers to the origin
n	normal-direction
blade	a variable of turbine geometry(eg. blade angle φ_{blade})
flow	a variable of the flow(eg. flow angle φ_{flow})

Superscripts

‘	refers to the control volume
-	above a term indicates the term is a vector
^	above a term indicates the term is a unit vector

Abbreviations

1D	1-dimensional
2D	2-dimensional
3D	3-dimensional
AM	Ainley and Mathieson method
AMDC	Dunham and Came method
CFD	computational fluid dynamics
CS	control surface
CV	control volume
HCF	high cycle fatigue
HP	high pressure (turbine)
LP	low pressure (turbine)
NRV	non return valve
VWO	valve wide open

Definition of angles

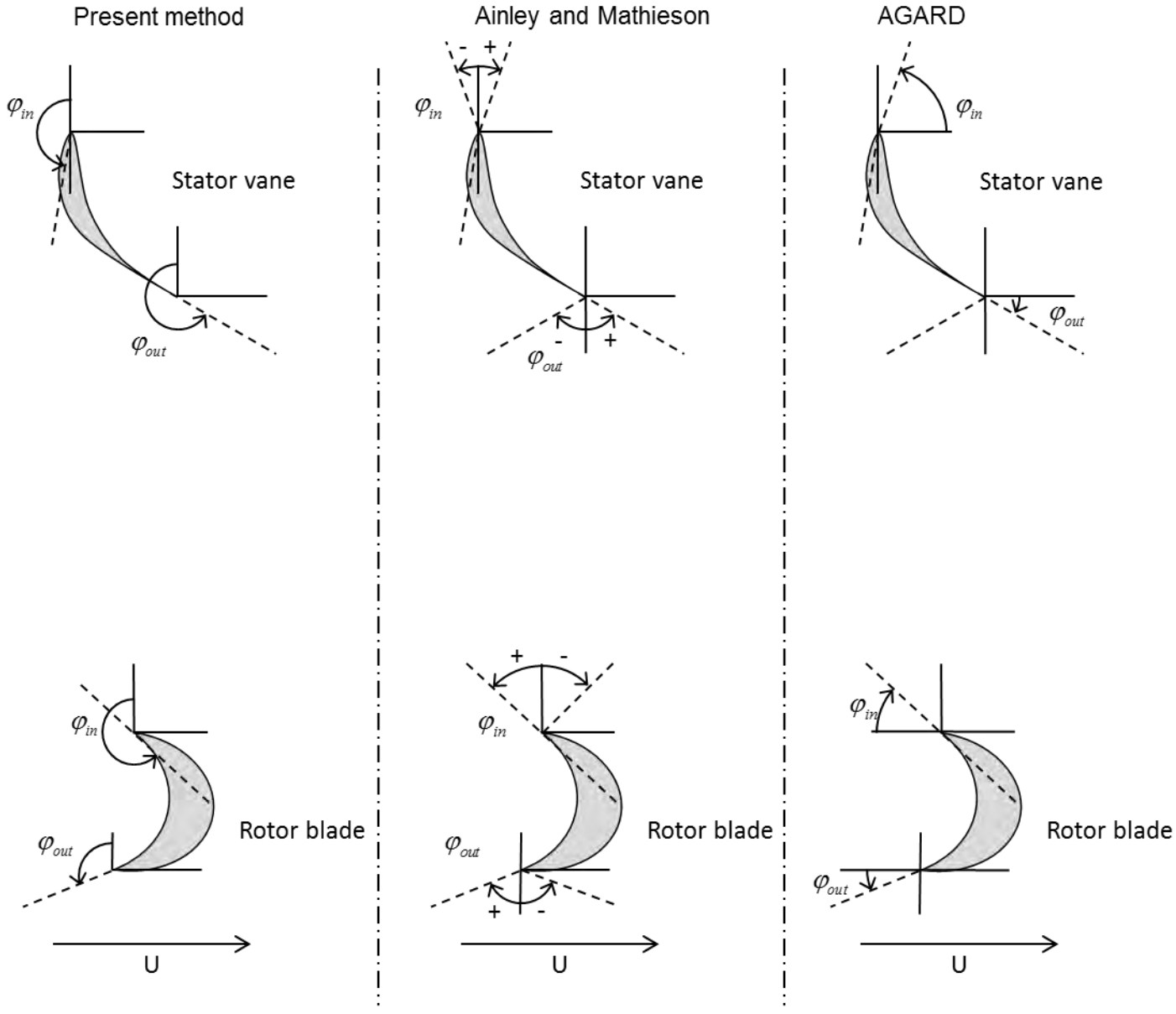

Figure 1. Definition of and comparison with angles used in the present method and various literature sources.

Chapter 1. Introduction

1.1 Background

Power utilities depend on the optimal operation of their equipment in order to achieve production and financial targets. The steam turbines used in fossil fired and nuclear plants are no different and often require detailed assessment in order to identify problems and find solutions. Whilst the performance of any steam turbine is initially determined by its design, level of sophistication and quality of manufacture and installation, its performance as part of an operational plant is determined by the level to which the initial performance can be maintained throughout its lifecycle. Three major factors that will influence this are the surface condition of steam path elements, the quantity of steam that bypasses the blade rows without doing work and any physical deformation of steam path elements that will affect or modify the expansion of the steam. Figure 2 and Figure 3 are examples of deterioration that affect the blade surface condition and blade geometry. Although some design features may induce or contribute to deterioration, the supplier of the equipment has no control over how the machine is operated and maintained. Therefore, the responsibility to maintain the efficiency of units in operation over their lifetime rests with the owner of the plant (Sanders, 1996).

Figure 2. Deposits on a turbine blade (Daniel, 2014).

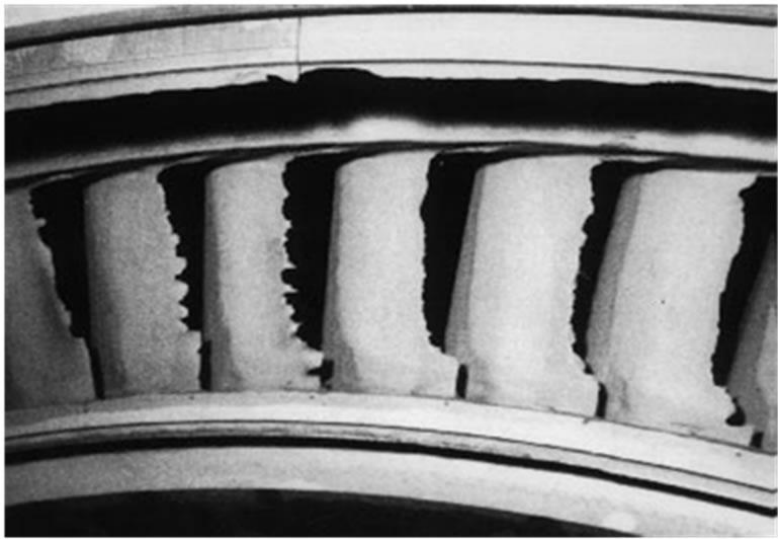

Figure 3. Turbine stator blades that have been eroded (Martínez, et al., 2012).

Part of operating a steam turbine involves understanding its performance, whether it is for the purpose of monitoring, control and diagnostics or for long term assessment of turbine performance. Plant engineers around the world are also faced with numerous reliability problems related to ageing turbine fleets. Engineers are required to assess the level of risk associated with an operational problem so that suitable recommendations can be made to production staff and maintenance requirements can be adequately motivated to management. Often the plant engineer only has at his disposal hand calculations based on turbine curves or generalised turbine analysis correlations based on test data for defined operational regimes. These are usually based on broadly applicable assumptions. These tools do not always provide the engineer with the accuracy or confidence to diagnose problems and formulate recommendations.

The plant engineer may need to investigate the effects of off-design or abnormal conditions such as (Cooke, 1983):

- Heaters out of service or degraded in performance.
- Emergency bypass of the turbine following a load rejection.
- Capacity of auxiliary systems to handle emergency heat loads caused by seal failure.
- Steady state extremes for transient system analysis.
- The economic impact of modifications to the plant.

Various tools exist to perform these calculations which range from hand calculations to detailed three-dimensional (3D) computational fluid dynamics (CFD) studies. These models can be used for design synthesis, real time simulations and monitoring.

Simplified models like the one in Figure 4, typically map input variables to outputs while omitting many intermediate variables. Characteristic maps are often not very accurate or not available and they are not well suited to the exploratory aspect of simulation (Leonard & Adam, 2008). Simplified calculations do not provide the necessary accuracy required for real time simulation and control (Chaibakhsh & Ghaffari, 2008).

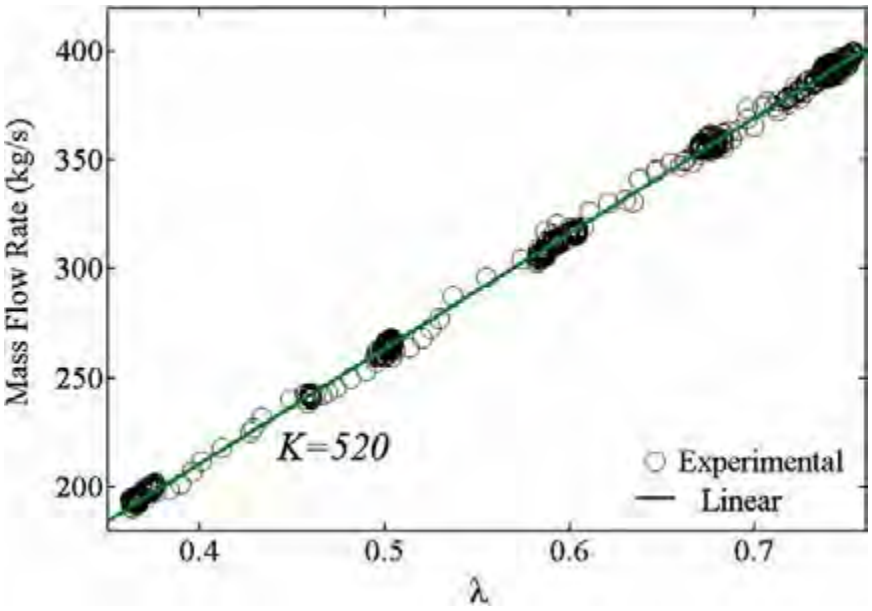

Figure 4. An example of how an empirical relationship is derived from experimental data (Nair, 2015).

At the other end of the detail spectrum, full 3D CFD analysis is a resource intensive activity that does not lend itself well to be applied as a general plant engineering tool in a practical manner. In Figure 5 an example of the results of a 3D CFD calculation obtained from literature is provided to illustrate the level of detail that can be achieved with CFD. Proper CFD analysis requires an expert in the field to perform the work and it is therefore reserved for detailed studies where the time and effort can be justified by the expected outcomes. This kind of calculation is also not suitable for integration into a complete cycle process model with varying operational parameters as each unique case needs to be set up and meshed manually. Typically such methods are used to study a single or limited number of blade passages in order to estimate the unsteady forces on blades (Denton & Dawes, 1998).

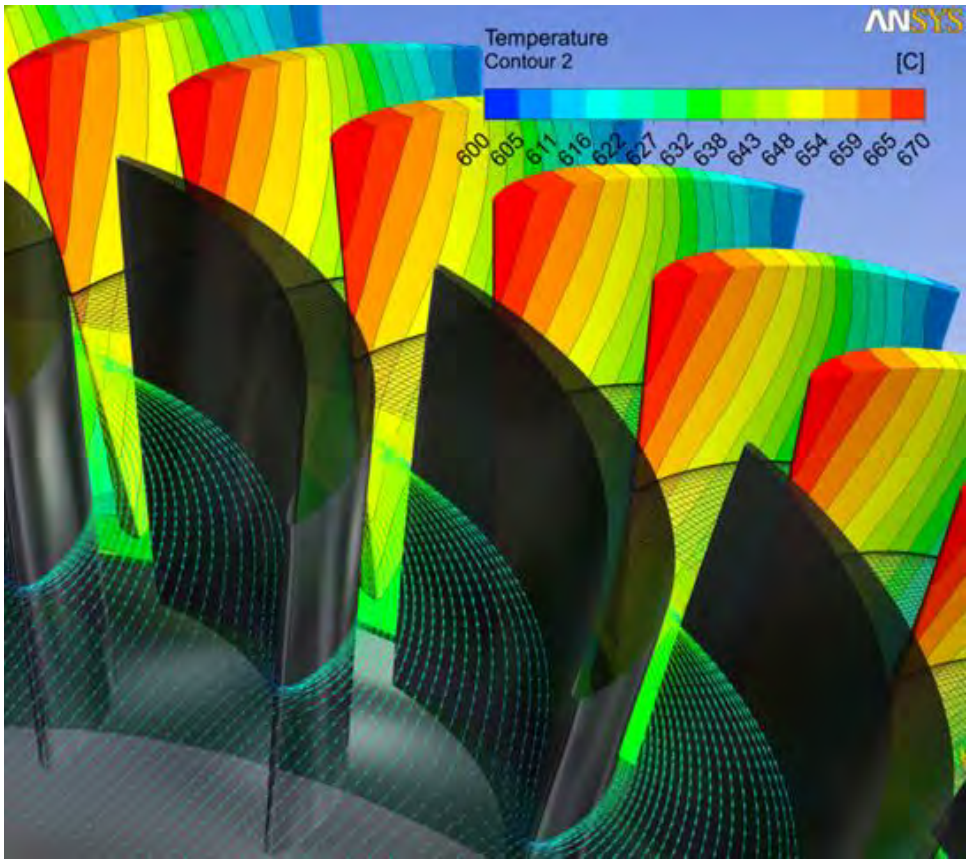

Figure 5. An example of velocity vectors and thermal contours obtained from CFD analysis (Anon., 2015).

On the other hand, one-dimensional (1D) simulation tools based on mass, energy and momentum balances allow for a very general modelling application which may include physical phenomena such as bleeds, heat transfers, water ingestion and fouling (Leonard & Adam, 2008).

1.2 Hypothesis

The hypothesis for this study is that a sufficiently accurate and detailed axial turbine process model can be developed for the purposes described above, based on a discretised stage-by-stage basis using 1D components, without having to resort to full 3D CFD analysis. In such a model each stage will be represented by one or more control volumes (CV) in which the fundamental mass, energy and momentum conservation equations for compressible flow through a one-dimensional "rotating channel" is solved. The required closure relations will include the various loss coefficients which can be characterised using correlations available in the literature.

1.3 Purpose and scope

The overall purpose of this study is to contribute towards the development of an axial turbine process model that can be applied in a plant engineering environment to investigate the causes of operational problems or anomalies experienced in industrial turbines. The purpose is not to demonstrate all possible problems that can be encountered in the industrial environment, but to rather maintain a generic approach. Thus it is also not envisaged as a solution to specific problems. The model will be developed so that it can be utilised as an independent turbine model or integrated into a complete power plant process model, however it is not within the scope to demonstrate how it is integrated into a larger model. It is anticipated that most of the industrial turbine related problems envisaged here can be sufficiently described through steady state analysis. Two-phase flow will not form part of the scope. The model will therefore only be applicable to compressible gas flows. A turbine case study will be identified to form the basis for the development of the model and to validate the model. In the development of the methodology it will be endeavoured to strike a suitable balance between the computational resources required and the accuracy and flexibility with which the method can be applied in an industrial setting.

1.4 Objectives

The specific objectives of this study are as follows:

- Development of a methodology for the solution of the fundamental mass, energy and momentum conservation equations for compressible gas flow through a 1D “rotating channel”.
- Determining the level of discretisation required for application of the model to a real-life turbine.
- Identification and implementation of the required closure relations for the various loss coefficients based on correlations available in the literature and/or refinements based on the operational data.
- Validation of the model by comparison with real-life turbine data for steady-state operation.
- Demonstration of the model by application to hypothetical case studies.

Chapter 2. Literature review

2.1 Historical overview

The complex nature of turbine performance and loss mechanisms has been the subject of enormous efforts in research over many decades. The result is that machines with efficiency in excess of 90% are now common, but during the early years of development loss mechanisms were barely taken into account. It was only after the advent of gas turbines for aeronautical applications that serious consideration was given to performance. During this period several of the performance prediction methods, such as those pioneered by Howell, and Ainley and Mathieson, were developed and are still in use today (Denton, 1993).

The requirement to predict the performance came from the need to develop new turbine designs and improvements to existing designs. Studying the turbine performance at design - and various off-design conditions allowed for improvements in the overall performance of the design to be explored during the early design stages. Figure 6 is an example of a modern multi-stage industrial steam turbine, showing the rotor assembled in the bottom half of the casing.

Figure 6. A modern multi-stage industrial steam turbine (Siemens, 2016).

2.2 Two dimensional cascades

The principle of operation of any turbomachine rests on the change in the angular momentum of the working fluid as it moves through individual blade rows (Dixon, 2005). When studying these flows the first simplification to be made is to look at the flow through a two-dimensional (2D) cascade. A 2D cascade is a row of stationary blades used in wind tunnel tests intended to investigate effects in real turbines.

The force applied to the 2D profile can be derived for the axial and tangential components of the flow by application of the momentum equation. Energy losses can be described by relating the loss in total pressure to the change in static pressure and the change in velocity of the fluid (Dixon, 2005). Many of the loss models still in use today were derived from experimental test results of 2D cascades.

This 2D approach may be extended to axial turbines by making the assumption that the flow conditions at the mean radius fully represent the flow along the entire length of the blade. The assumption is therefore made that losses obtained from 2D cascade tests can approximate losses in a real turbine. For stages where the ratio of the blade height to mean radius is small, i.e. short blades, this approach can provide a reasonable approximation. However, for long blades such as the final stages of a steam turbine, it is important to consider 3D effects of the flow (Dixon, 2005).

2.3 Determining a suitable general approach

Models based on empirically derived losses have been developed into very accurate tools for predicting turbine performance as the models are tuned by each manufacturer to suit existing designs as well as extrapolated to new designs. In this way accuracies of ±2% can typically be achieved (Denton, 1993). There is a risk that this causes an impression that the models capture flow physics which may lead to the models being applied outside their valid range (Denton, 1993). However, the methodology has proved invaluable and with improved understanding of the flow physics and continuous development, empirical methods can play an important role in the prediction of turbine performance.

It appears that since the 1980's when numerical solutions of the 3D flow became a reality much of the focus of research has shifted to this approach for use as a design, optimisation and simulation tool. Today it is possible to simulate flows through a complete turbine consisting of

several stages of stationary and rotating blades by applying 3D CFD. This is not a simple exercise and requires expert knowledge and skilled application of turbulence models, boundary conditions and mesh generation to obtain useful results. The time invested in 3D CFD analysis is several orders of magnitude longer than for 1D and 2D analysis (Leonid, et al., 2005) thus rendering it impractical as a general engineering tool. 3D CFD models have to calculate the losses by modelling the secondary flows and often require unsteady analysis especially of the unsteady interactions between stages to accurately predict the losses. Secondary flows in the stage are dependent on the inlet boundary layer thickness. This places a limitation on 3D CFD as the inlet boundary layer thickness has to be guessed at the boundary condition (Denton & Dawes, 1998). It is also recognised that the interaction between primary and secondary gas paths play a significant role in the losses. Thus the CFD model must be able to calculate both gas paths simultaneously, requiring unstructured meshes or multi-block meshes (Denton & Dawes, 1998). The mesh of one CFD model developed by Gardzilewicz, et al. (2003) of the last stage of a turbine required around 2 million finite volumes. The result is that in many cases, plant engineers still apply the simple and proven empirical models as a tool to investigate and solve the day-to-day issues that they are confronted with.

Most of the empirical models reported in open literature have been focussed on gas turbines. A turbine is usually designed to perform optimally at some design point of operation. This is done by matching the blade leading edge angles to the oncoming flow velocity and direction. However, gas turbines may be required to operate at various shaft rotational speeds during start-up, idling and variable power and speed. This results in a mismatch between the velocity vectors and the blade geometry causing additional losses (Moustapha, et al., 1990). In power plant steam turbines, except for starting purposes, the rotor speed is fixed by the grid frequency. When one considers that at reduced loads the pressure and mass flow rate are reduced by the control valves and that consequently the steam volume increases, it can be shown that there is very little variation in the volume flow rate of steam through the machine. The result is that there is very little variation in the steam velocity vectors and the machine efficiency is not necessarily a function of the load. There are some exceptions however, such as very low loads, wet steam conditions and with degradation of the steam path elements (Gill, 1984). In the past many of the gas turbine models have been applied to steam turbines. It was only when Dunham and Came (1970) included allowance for aspect ratio and blade height effects to the Ainley-Mathieson model (1951), that convincing results could be obtained for typical steam turbine designs as opposed to gas turbine designs. With this in mind Craig and

Cox (1970) set out to develop a method that could be used for both gas and steam turbines. They attempted to take into account the full range of Reynolds numbers and aspect ratios encountered in such machines. Their model also dealt with several auxiliary sources of loss which were often omitted from other models (Craig & Cox, 1970).

In order to maintain a generic approach, the necessity of a real gas model cannot be disputed. In the case of a steam turbine, the ideal gas model will result in incorrect calculation of the steam parameters. However, the use of a real gas model comes at a significant cost in calculation time as calculation of especially steam properties can be time consuming.

Pipe network algorithms have been developed to calculate flows in complex networks of pipes. These algorithms are based on the fundamental principles of flow physics namely the conservation of mass, energy and momentum. The conservation equations are closed by using empirical relationships to determine pressure losses in the pipe network. Due to the implementation of fundamental physics some of these programs can also deal with components other than pipes where flow energy is converted to work, or heat is transferred to and from the fluid. For example Flownex uses an implicit pressure correction method to perform thermofluid analysis of a network (Flownex, 2013). The software package has proved itself useful in a broad range of fluid network applications where heat and mass transfer play a role. Typical steady state 1D fluid network models can be solved in a matter of seconds on a modern personal computer.

A balance between the level of detail required for engineering analysis and complexity of the model can be achieved by a method that captures fundamental physics through the turbine stages, but uses empirical relationships to deal with detailed secondary flows that cause losses and instability on a smaller scale.

2.4 Discretisation

Some common methods that model the turbine on a row-by-row basis utilise a control volume to discretise each row by applying characteristics at a mean radius to the control volume (Dixon, 2005). Analytical or lumped volume 0D models may be used to simulate a wide variety of operating conditions, but their extension to physical or technological effects are difficult (Leonard & Adam, 2008). When extending 2D theory to complete machines, Dixon (2005) suggests that for stages where the ratio of the blade height to mean radius is small, this approach can provide a reasonable approximation. However, for long blades such as the final

stages of a steam turbine, it may be necessary to perform the 2D calculation at multiple stations along the blade length or to use full 3D analysis as there is greater variance of the influence of wall effects along the blade length (Dixon, 2005).

In the work done by Leonard & Adam (2008), an attempt was made to account for the distribution of wall effects by applying them according to parametric spanwise curves and averaging to obtain mean contributions of these losses. The contributions were used as source terms in a 1D CV solution of the Euler equations. The model describes the flow along a mean line of the turbine using the blade geometry and angles at mid span. The model is based on the unsteady quasi-1D Euler equations for mass, meridional momentum and energy balances and conservation of momentum in the tangential direction. The 1D formulation requires that all quantities are constant in a cross sectional area of the flow path. Their program calculates the velocity triangles at the blade inlet using the blade speed and volume flow rate during each iteration of the calculation. The velocity triangle at the blade outlet is determined by using the correlations of Ainley and Mathieson (1951). They found that the accuracy of the simulation depends greatly on the suitability of the loss and flow deviation correlations for the type of blade. Equipped with adequate correlations, the model showed excellent agreement when compared with test rig data (Leonard & Adam, 2008).

According to a study performed by Leonid, et al. (2005), it is important to understand the distribution of loss components to be estimated along the radius. Their study was aimed at proving the usefulness of simpler simulation models compared to full 3D analysis, and to assess the limitations of the various methods. Numerical studies included 1D and 2D stage computations and 3D CFD analysis using commercially available software. They illustrated that the use of 1D and 2D models based on validated empirical models provide sufficient accuracy for use in many design problems in practice. In their study of an axisymmetric type model, the Craig-Cox method (Craig & Cox, 1970) for profile and secondary loss analysis was utilised and the secondary losses were bundled at the blade tip and root through an algorithm. The blade was broken up into several stations along the blade length and the profile loss at each station was characterised. The secondary loss was calculated at each station according to the local profile loss and then concentrated at the blade root and tip by using a parabolic distribution. A tip leakage loss was also included in the calculation. As an illustration the tip clearance was varied in both the 1D and 2D models. Although both models showed the same trends, the accuracy of the 2D model was significantly higher. They attributed this to the more accurate

estimation of pressure distribution towards the periphery built into the 2D model (Leonid, et al., 2005).

Their results showed that even though the 1D and 2D calculations account for the same parameters, accuracy of the 1D calculation was significantly lower at smaller aspect ratio due to the approximation of pressure distribution towards the peripheral diameter. Results showed that computations performed with 2D models provide reliable results over a wide interval of operating conditions and parameter variation (Leonid, et al., 2005).

When comparing the results of 2D, 3D and test rig analysis it was found that both models predicted the nozzle row exit with good agreement to rig data. However the models were less successful in determining conditions at the rotating blade exit and both deviate for the test rig data in this region. The authors concluded that the 2D model is limited in capturing all flow separation effects, but that it was quite sufficient in estimating kinematic and power parameters of a stage. The 3D CFD model required significant tuning to obtain results comparable with the test rig data. The authors tested various meshes and turbulence models, but could only resolve the model by adjusting the blade geometry (Leonid, et al., 2005).

Slawomir, et al. (2007) presented a numerical model on the flow through a steam turbine last stage where distributions of flow parameters play a significant role due to the length of the blades. They specifically considered the wet steam flow field in the last stage of a steam turbine. As with many other authors they found a strong emphasis on the relationship between discretisation of the computational domain and the quality of the results. Three methods of calculation were tested and compared namely a simple streamline curvature method (SCM) and two CFD codes. For the SCM, the loss coefficients were calculated along the blade length by using circumferentially mass averaged values of the flow parameters and blade geometry. They found qualitative similarities between the distributions of loss coefficients and calculated velocities between the SCM and CFD methods.

This motivates the hypotheses that with spanwise discretisation of the 1D model and with correct application of the loss coefficients a qualitatively similar result can be achieved in the present work.

2.5 Sources of loss

When discussing the sources of loss associated with turbine flows, one needs to consider the geometrical complexity of turbine construction together with the complex flow patterns that

develop due to the steep pressure gradients present within the turbine. The basic construction of a turbine stage consists of a static nozzle or stators fixed to the turbine casing and a rotating row of blades fixed to the turbine shaft. The turbine is made up of several stages arranged in series, Figure 7.

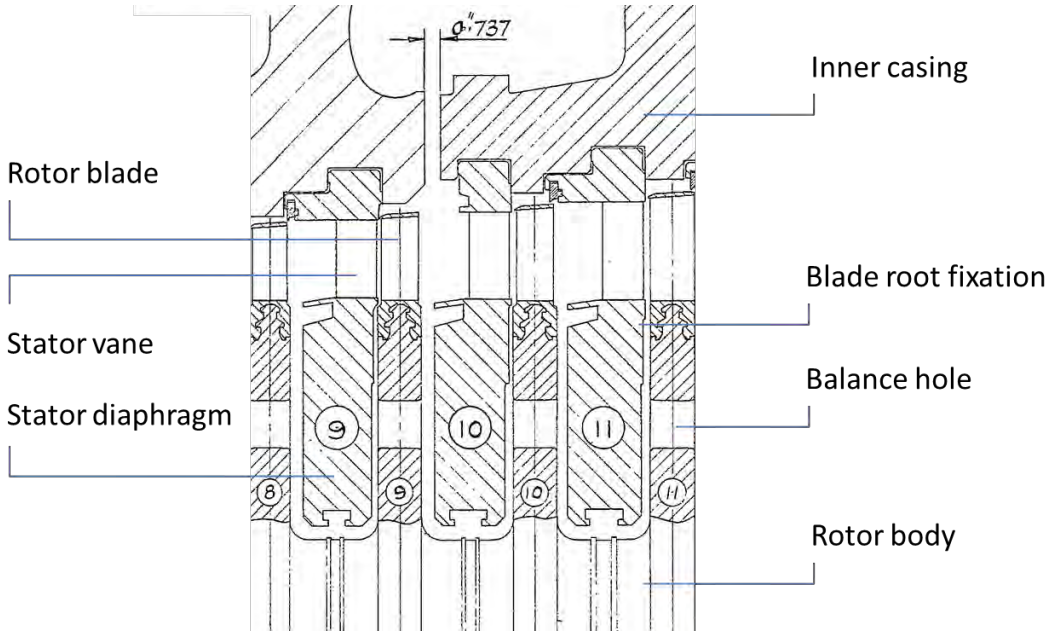

Figure 7. Cross section of three turbine stages.

Due to the machine having stationary and moving parts inside a pressurised casing, sealing is required where the rotor shaft protrudes from the casing, but also in between stages.

Fundamentally, the losses can be attributed to dissipation of energy and the associated generation of entropy by viscous fluid shearing that occurs on a microscopic level. On a macroscopic level viscous fluid shearing is always associated with a flow structure. Typical examples of regions where flow structures associated with losses occur are boundary layers and flow vortexes where steep velocity gradients occur.

When one considers the turbine blade passage flow field, boundary layers occur on blade surfaces and endwall surfaces. Vortexes are generated in areas where sudden changes in the geometry occur, such as where the blade protrudes from the hub. Further disturbances to the flow are caused by suction near the turbine bleed points and jets caused by interstage seals that are entrained into the main flow.

Historically turbine researchers have grouped the various sources of loss into categories that could be associated with specific geometrical features and therefore isolated for experimental analysis. This approach was pioneered by Ainley and Mathieson (1951) and the convention has been adopted by most researchers who followed a similar approach to quantifying the losses. The losses are typically lumped into profile loss, secondary loss and tip leakage/clearance loss. When modelling a complete turbine, auxiliary losses must also be considered.

2.5.1 Profile loss

The losses associated with the 2D blade profile are called profile loss. These losses would occur on infinitely long blades, arranged in a cascade. They are the result of surface drag in the boundary layer, the reduction of flow area due to an increasing boundary layer thickness, pressure drag of the profile and areas of flow separation, and the separation and wake induced by the finite thickness of the blade trailing edge.

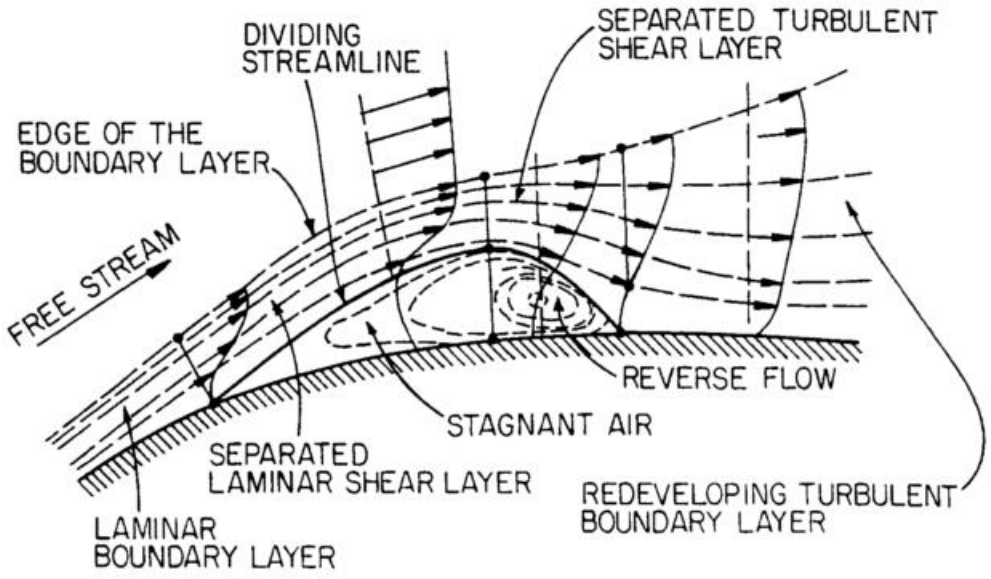

Figure 8. Illustration of boundary layer velocity profiles and streamlines. (Ning, 2000)

Depending on the pressure gradients, there may also be areas of the boundary layer that separate from the blade surface. Such separated flow is associated with an increase in pressure drag. In some cases the separated flow can reattach to the blade causing an enclosed separation bubble to form on the blade surface, Figure 8 (Ning, 2000).

2.5.2 Secondary loss

Suitably named, the next category off loss was named secondary loss. Secondary loss refers to losses associated with the 3D nature of flow within the blade passage. The three dimensionality of the flow is a result of pressure gradients within the blade passage and geometrical characteristics of the passage. Traditionally the secondary losses were defined as the difference between the total loss and the profile loss for a turbine cascade where there are no leakage flows. The main feature of the secondary flow field is the horse-shoe vortex that forms at the blade root and tip and is then transported through the blade passage by the flow. The horse-shoe vortex forms as the boundary layer flow is rolled up into a cylinder by the blade protruding into the flow path. The cylinder bends around the blade leading edge as it is transported into the blade passage forming one clockwise and one counter-clockwise vortex inside the blade passage.

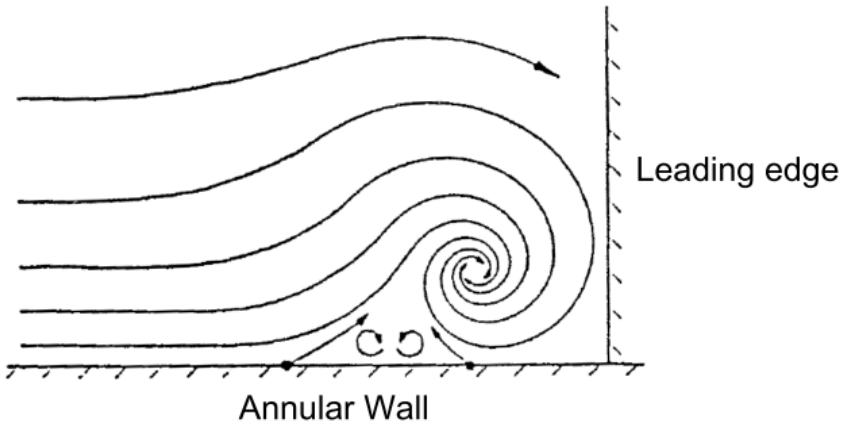

Figure 9. Illustration of the formation of a horse-shoe vortex at the blade leading edge (Dahlquist, 2008).

The second main feature is the passage vortex that develops within the passage and is driven by the pressure gradient between the pressure and suction sides respectively of two adjacent blades (Ning, 2000).

The losses associated with these two flow structures are further complicated by their interaction with one another. The horse-shoe vortex can either act to strengthen the passage vortex or wrap around it forming a counter rotating swirl depending on whether it is the clockwise or counter-clockwise part of the horse-shoe vector.

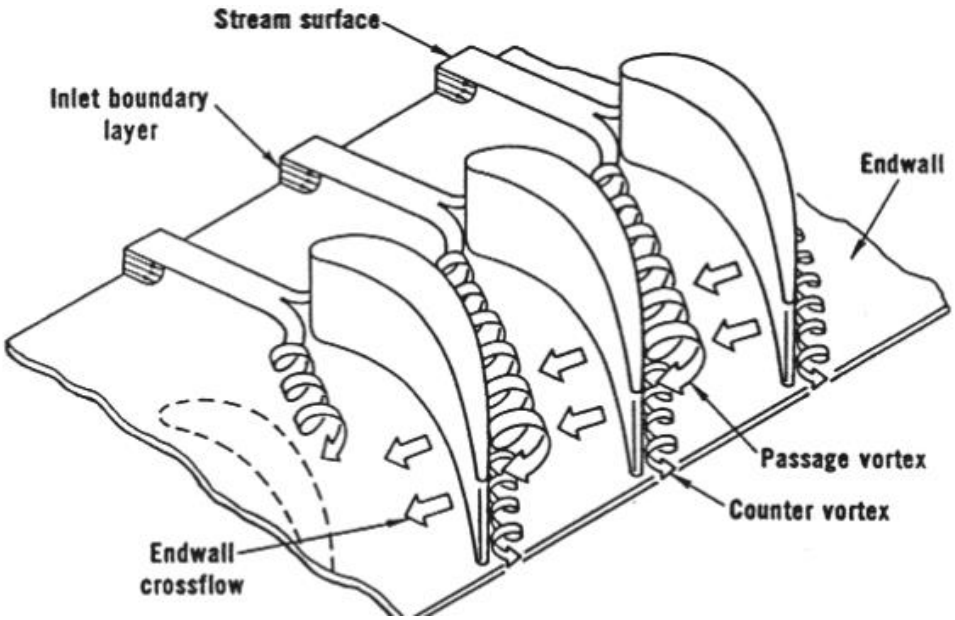

Figure 10. Illustration of the interaction between the horseshoe vortex and the passage vortex (Ning, 2000).

2.5.3 Tip leakage/clearance losses

The third parameter that is associated with loss inside the blade passage is the leakage losses. Tip leakage losses are caused in the rotating blade row where there is a leakage between the moving blade and stationary turbine casing. Fluid is forced through the clearance by the pressure gradient across the blade tip and does not perform any useful work. Some turbine stages may be equipped with shroud bands to improve sealing. Leakage losses also incorporate the effects that are caused by the leakage jet as it is entrained into the main passage flow.

2.5.4 Auxiliary losses

Other sources of loss that must be considered occur between turbine stages. This is mainly leakage between stationary and rotating parts that result in some of the steam bypassing the main blade passage and not being useful to perform work. Also flow disturbances caused by overlap of turbine blades, entrainment of steam jets from leakage flows into the main flow and diffusion of the flow as the passage area increases (Craig & Cox, 1970).

2.6 Review of loss models

2.6.1 Ainley and Mathieson

The authors Ainley and Mathieson (1951) developed a method of turbine performance estimation that is still one of the most commonly used methods today and is used by many engineers to predict turbine performance or assess deviations from design performance. It was developed during the 1950's and is based on experimental data that was available in open literature at the time. During the development of the method only those variables were considered that could be proven by statistical experimental evidence to be essential to predict the performance to within ±2% (Ainley & Mathieson, 1951).

The losses included are the profile loss, tip clearance loss and secondary loss for nominal and off-design cases. Variations in Reynolds number and outlet Mach number are also considered. The method is applied by following only one flow path through the turbine at a reference diameter and applying loss correlations to the geometrical and flow characteristics at that diameter. The authors attribute the accuracy of the method to the correlations being derived from data obtained from a broad range of turbines. However, this also implies a limitation as all the turbines made use of conventional blade profiles and therefore the applicability to designs deviating significantly from this cannot be guaranteed (Ainley & Mathieson, 1951). Due to the age of the correlations it must be considered that the blade geometries of today differ significantly from that time and this may impact on the accuracy of the results when applied to modern machines (Dahlquist, 2008). In the work done by Kacker and Okapuu (1982), the authors noted that while the Ainley-Mathieson method predicted the variation of efficiency with specific speed, it could not adequately predict the variation of velocity ratio for high velocity ratios.

2.6.2 Dunham and Came

Dunham and Came (1970) reviewed the correlations of Ainley and Mathieson (Ainley & Mathieson, 1951) during the 1970's and made some improvements. The primary weakness of the Ainley-Mathieson method was found to be when it was applied to small-scale or unconventional types of turbines. The modifications were primarily done on the secondary and tip leakage losses and corrections for the Reynolds number and exit Mach number were included. Their model shows good ability to predict secondary losses for both low aspect ratio

blades and low reaction stages. The authors state that their correlations can predict the flow field to an accuracy of ±3% and the total-to-total efficiency to within ±2% (Dahlquist, 2008).

2.6.3 Kacker and Okapuu

Kacker and Okapuu (1982) performed another review and update of the Ainley and Mathieson paper (Ainley & Mathieson, 1951) about a decade after the work by Dunham and Came (1970). The aim of their paper was to verify the applicability of the correlations to more modern designs of turbines and to develop new correlations where an improved understanding of the flow in a turbine showed some weak points in the previous models. Their updated correlations were tested against 33 turbines covering a wide range of sizes and typical designs of that time. In the sum of losses equation, the blade Reynolds number is only considered to affect the profile loss coefficient and the trailing edge loss coefficient is separated from the other loss terms. This was done since the authors could not find any relationship between some of the parameters such as trailing edge losses and tip clearance losses for example. An extension to the profile loss equation is introduced to allow for a negative inlet angle and a factor of 2/3 is introduced to better predict the profile losses associated with turbines of that era. Furthermore the impact of shock losses at blade leading edges and the channel flow acceleration due to compressibility effects are considered. The distribution of incident Mach number along the length of the blade, which is caused by the radial variation in gas properties, is implemented according to a simple distribution of flow properties along the length of the blade. Further analysis of test data at high subsonic Mach numbers showed that the profile loss coefficients determined from tests carried out at lower subsonic speeds can over predict the loss. This is attributed to local suppression of flow separation and a thinning of the boundary layer when passage exit conditions approach sonic velocities. In addition to corrections for profile, secondary and tip leakage losses, they also developed a separate correlation for the loss generated by the trailing edge thickness based on an extensive survey of published and in-house cascade results. A new parameter to handle the channel flow acceleration and shockwaves were included. Their method is reported to be accurate to within ±1.5% efficiency (Kacker & Okapuu, 1982).

2.6.4 Craig and Cox

The Craig-Cox method (Craig & Cox, 1970) for prediction of turbine stage losses is claimed by the authors to be accurate to within ±1.25%. The authors make specific mention of the

shortcomings of the Ainley-Mathieson method with regards to steam turbine modelling and set out to develop a method suitable for both steam and gas turbines. The method also deals with auxiliary sources of loss that are often omitted in other methods. The correlations for profile and secondary losses were developed from test data of a linear cascade test, while other loss correlations were derived from specific turbine tests and from annular air tests. Craig and Cox also grouped the losses into two groups namely:

Group 1. Profile, secondary and annular loss in the rotor and stator.

Group 2. Tip leakage loss in rotor, leakage loss in the stator and balance hole, lacing wire, wetness, disc and partial admission losses.

Group 1 losses are evaluated based on relative blade outlet velocities. Group 2 losses are evaluated as a net deficit in stage efficiency as this was the simplest way in which they could be derived from test data. Profile loss is not constant along the span of the blade and can be calculated at stations along the blade height. Secondary loss can be calculated separately for the root and the tip. The losses that occur in-between rows of blades, such as lap, annulus and cavity losses are considered to be one dimensional and not variable along blade height. Because it was not known how the losses from group 2 are absorbed into the main flow, they were incorporated in a mixing zone downstream of the rotor outlet (Craig & Cox, 1970).

The authors also looked at the independence of variables that are chosen. An example is given that if the effect of Reynold's number is to be evaluated experimentally, invariably the Mach number or aspect ratio must also be varied, yet these would be considered independent stage characteristics. The correlation developed is tested against more than 100 specific cascade tests in order to confirm that the correct choice of independent variables has been made.

The authors focus on the contributions of auxiliary losses such as diffusion of the flow between passages, wall cavities associated with leak-offs and seals, overlap between stages, balance holes and glands.

In the Craig-Cox method the losses from group 1 are considered to be variable along the blade path and should not be calculated at just one diameter, but rather at three diameters, namely root, mean and tip, and then an average value should be calculated with a parabolic loss distribution (Craig & Cox, 1970).

2.6.5 Spencer, Cotton and Cannon

Spencer, Cotton and Cannon (1963) presented a method for determining the performance of modern steam turbines by reading typical parameters from graphs and tables. The performance at design flow is predicted accurately by applying the following variables to a series of graphs and tables:

- Volume flow rate.
- Pressure ratio.
- Initial temperature and pressure.
- Governing stage design.
- Exhaust loss.
- Mechanical losses.
- Generator losses.

The expected accuracy when applying the method is not stated. The equations used to develop the tables and graphs are also provided in an appendix and include useful empirical equations for predicting stage efficiency and shaft packing leakages (Spencer, et al., 1963).

2.6.6 Benner et al.

In a more recent study performed by Benner et al. (2006), previous correlations by the authors and some of the more commonly employed correlations were reviewed based upon data from open literature, their own experimental data and a modern understanding of flow physics. Data from 34 linear cascade tests performed between 1977 and 2003 were employed.

From this work followed a new loss breakdown scheme that redefines secondary loss and a correlation to suit this scheme was developed. This stemmed from a physical problem that they observed with the original definition that would imply negative losses for very large incidence angles. Traditionally the secondary loss was defined as the difference between the profile loss value at the midspan and the total loss measured for a cascade with no tip leakage. Thus the assumption is made that the profile loss is constant across the blade span with secondary losses superimposed on it. From oil film flow visualisation studies performed by Benner et al. (1997), the authors noted that there are two main areas on the blade surface where loss is generated by different mechanisms. They divided the blade surface into two regions namely the primary and the secondary regions. The primary region is bounded by the passage vortex separation lines and the blade leading and trailing edges as illustrated in Figure 11.

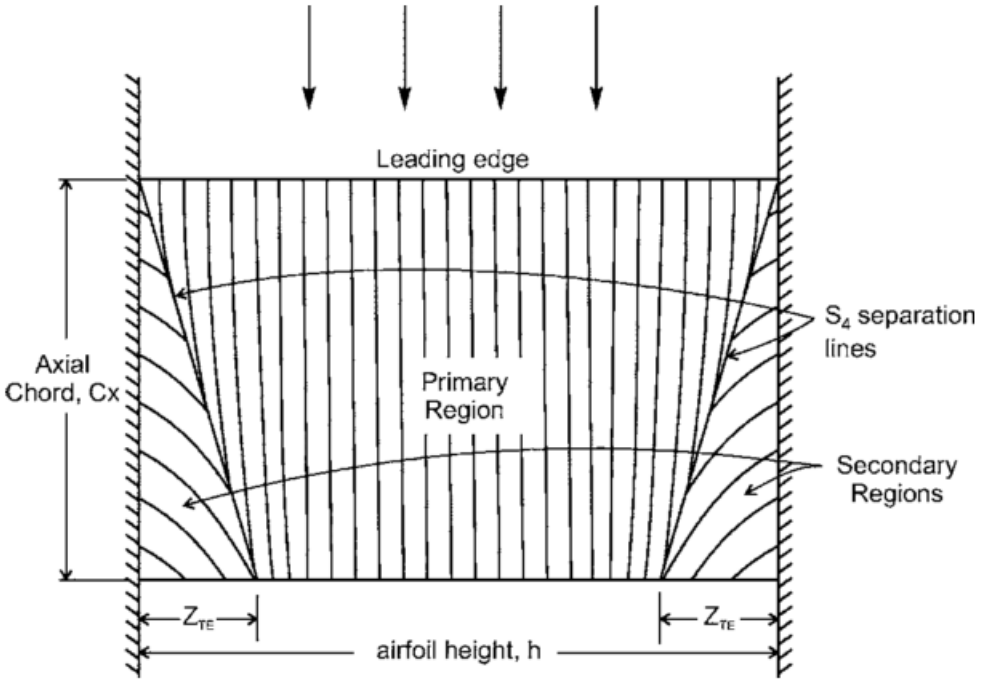

Figure 11. The regions of the loss breakdown scheme proposed by Benner et al (2006).

Thus according to the new scheme, the profile loss is defined as the loss generated in the boundary layer in the primary region where the secondary loss has little influence on the boundary layer. The secondary loss is then defined as the difference between the total loss and the profile loss. Thus the secondary loss includes surface boundary layer losses in the secondary region as opposed to the traditional scheme where this was attributed to the profile loss. The new definition of the secondary loss takes into account the penetration depth of the passage vortex and this is calculated from a separate correlation (Benner, et al., 2006).

It is suggested that a profile loss correlation such as that of Kacker and Okapuu (1982) is used to calculate the profile loss in conjunction with the new correlation for secondary loss. The loss breakdown scheme assumes that the secondary flows from each of the endwalls do not merge at the blade midspan. Like the older loss schemes this precludes cases where the secondary flows are likely to meet such as low aspect ratio geometries. The authors cannot define a lower limit for the aspect ratio as merging of the secondary flows is also a function of other flow parameters (Benner, et al., 2006).

The new correlation also accounts for recent improvements in turbine blade design as only data from the past few decades were used. Important factors that influence the end wall losses were

identified to be the total airfoil loading and loading distribution, flow acceleration, endwall surface area and inlet boundary layer vorticity (Benner, et al., 2006).

2.7 Limitations of simplified models

Many of the loss correlations are derived from experimental data obtained from tests on linear cascades of blades in a wind tunnel. Therefore, it must be considered that the models may not include all the effects that will occur in a real turbine. Craig and Cox (1970) separated the differences into two categories. First the aerodynamic differences:

- Different working fluid.
- Different Reynolds number.
- Different scale of the blade.
- Different surface roughness.
- Different Mach number.

The differences mentioned here can be corrected for if the information is available using standard aerodynamic theory of wind tunnel tests. The second category contains more fundamental differences:

- Uniform inlet flow in a cascade as opposed to flow containing wakes and disturbances from upstream stages and stage leakage.
- Linear layout in a cascade as opposed to annular flow in a turbine.
- Stationary walls relative to the blades in a cascade as opposed to moving walls in a turbine.

In the case of the second category these effects can simply not be captured in cascade tests (Craig & Cox, 1970). The results of such tests must be compared with actual performance data and the magnitude of the errors must then be derived.

The commonly used prediction methods reviewed above categorise the losses as profile loss, secondary loss and tip leakage loss and attempt to predict each loss independently of the others. These historical labels of the various loss sources have remained even though it is widely recognised that the loss mechanisms are rarely independent (Denton, 1993). Tip leakage for example, which arises from flow over the tips of rotor blades, clearly could have a strong influence on the endwall loss as it constitutes a major disturbance in the flow in the vicinity of the endwall (Denton, 1993).

New developments in experimental apparatus and numerical predictions have allowed better insight into the complex character of loss mechanisms, especially the three-dimensional effects and unsteadiness. Although great strides have been made in numerical solutions, their inherent complexity means that often in practice, correlations are still used for performance predictions. The correlations also do not capture the effect of new design features that did not exist when the methods were developed. It is therefore advisable to not rely on these prediction methods excessively without considering their basic principles and assumptions (Denton, 1993).

An overview of the various empirically derived loss prediction methods was performed by Ning (2000). Although the purpose of his thesis was not to determine which correlations are the best in general, he found that there can be significant deviations in the results provided by various correlations. His study shows that the trends between various loss models, Dunham-Came, Kacker-Okapuu, Moustapha-Kacker and Craig-Cox, are similar for impulse type blades. The Craig-Cox model gives the most accurate results close to the design point but over-predict the loss at off-design conditions. This is an important observation for steam turbines where off-design incidences are not as significant as with gas turbines. For completeness however, and to ensure that a broad range of steam- and gas turbine related issues can be modelled, the off-design losses will not be excluded. It is also noteworthy because Craig and Cox (1970) is the only work that explicitly looks at steam turbines and gas turbines and provides corrections for both these types.

When predicting the performance based on the effect of pressure loss characteristics, ultimately a pressure loss could be attributed to an almost infinite number of minute contributors. In contrast with this the need for simplicity of the model requires a minimum of variables to be used. Thus any method derived will ultimately be a balance between simplicity and accuracy (Ainley & Mathieson, 1951). Ainley and Mathieson considered only those variables that could be proven through statistical experimental data to affect the performance estimation to within ±2%. The threshold was considered to be in line with the expected accuracy of the experimental measurements of the data used (Ainley & Mathieson, 1951).

At design point, all the models mentioned above use the pitch-to-chord ratio to calculate the profile loss, except for Craig-Cox, that uses pitch-to-camber line length ratio. The acceleration of flow is captured by velocity ratio in the Kacker-Okapuu and Moustapha-Kacker models, while the Craig-Cox model uses the areas of the blade passage. For the design profile loss the Kacker-

Okapuu, Moustapha-Kacker and Craig-Cox models have similar results while the Dunham-Came model estimates the losses almost 30% higher (Ning, 2000).

Secondary losses are calculated as a function of the blade aspect ratio and blade loading in all of the models considered. In addition to that the Moustapha-Kacker, Kacker-Okapuu, and Craig-Cox models also take into account flow acceleration. All the models show that the losses are proportional to the blade loading and also provide the expected result that an increase in blade aspect ratio will reduce secondary losses. However, there is quite a large variation in the magnitude of the losses predicted. In an example provided, they found that a 25% increase in aspect ratio of a nozzle blade equates to a 10% reduction in loss according to the Craig-Cox model, while the Dunham-Came model predicts a reduction of 27% (Ning, 2000).

Tip leakage losses calculated with these models also show significant variation and even cases where the trends are dissimilar. At off-design conditions the Dunham-Came, Kacker-Okapuu and Moustapha-Kacker models predict an increasing trend related to the increasing incidence angle, while the Craig-Cox model could have a downward trend depending on the inlet and outlet velocity ratio in this case (Ning, 2000).

From these works it is clear that when applying these loss models, the type of turbine modelled must have similar geometrical features as the cascade or turbines used to develop the models. In meanline efficiency prediction methods that utilise sums of large numbers of loss coefficients, some of these losses may prove to be quantitatively imperfect, but the errors cancel because of the manner in which they are combined. According to Kacker and Okapuu, the final proof of a loss system must be its ability to correctly predict the efficiencies of well documented turbines. However, for the purpose of detailed modelling with the aim of obtaining highly accurate results, this factor could negatively affect the results and must be taken into account during analysis.

2.8 Applications of turbine models

The required level of complexity of a simulation model is determined by the task that it needs to fulfil. Often generalised models can provide sufficient detail for a specific application, while in other cases precise results are required. For example, the turbine controller may use a simplified model to predict the general trends with the aid of black box components and obtain the required information. Investigations into component level failures may require very precise

and detailed results. Some applications may also require transient behaviour to be studied, but most thermodynamic properties can be investigated using steady state models (Zimmer, 2008).

Turbine controllers often include a model of the turbine so that the controller can analyse a specific state and pre-empt the response of the machine to changes made by the controller or faults detected by the turbine protection system. For example, if a load rejection is detected, the controller has to switch from load control to speed control while intercepting the turbine at nominal speed. The controller needs to pre-empt the possible overshoot that may result from the sudden loss of load in order to effectively intercept the speed. This is done by applying the current conditions to a model that will predict the expected acceleration.

When analysing possible failure modes, turbine modelling can be applied to determine cues that can be used to detect a state of failure or impending failure. The protection system can then be programmed to issue a trip signal to the turbine if any of these signals exceed the safe limit. If the protection is against over pressure in a certain device, the turbine model can be used to determine the allowable delay through the protection system that will ensure that the maximum pressure reached will remain within the allowable limits. For example, if the HP turbine exhaust flow is blocked by a blockage in the reheat pipework, the pressure in the exhaust area and reheat pipework will continue to rise after a trip signal was issued until the pressures are equalised. The maximum pressure that will be reached can thus be determined by careful modelling of the system.

Another possible failure mode that lends itself to turbine modelling is the case where a turbine extraction Non Return Valve (NRV) fails to close in the event of reverse flow from a feed water heater. Such an event can arise when the turbine governor valves react to a load rejection. The resulting pressure drop in the turbine can cause condensate in the extraction system to flash over to steam and supply the turbine with steam that will add to the momentum and increase the probability of an overspeed event. By modelling cases for the various extractions, the turbine designer can determine which of the extractions require redundant NRV's to ensure adequate protection (Zimmer, 2008).

During failure investigations, knowledge of the expected flow characteristics at various load points can be used in root cause analysis. In one example where LP turbine inlet blades on a non-reheat turbine failed due to high cycle fatigue (HCF) it was shown that an earlier change in the operation of the machine contributed to this failure. In this case, the live steam temperature was reduced by 10^{o}C temporarily while further investigations into creep damage

found in the control valve chests were undertaken. It was found that the slight increase in wetness at the HP turbine exhaust was sufficient to contribute to the failure.

Similarly, an investigation into LP turbine last stage blade failure also due to high cycle fatigue, could be contributed to periods where the unit was operated at low load with poor vacuum. In this case it was shown that reverse flow was occurring in the stage and that the resulting flow instabilities could contribute to the excitation of the resonant frequency of the blade (Mazur, et al., 2008).

Many factors can lead to deterioration of the turbine performance during operation. Erosion of blades, deposition of salts on blades and wear of internal seals can only be detected by visual inspection and physical measurement on the turbine internals, or via detailed analysis of the turbine performance (Beebe, 2003). Many other failure modes can only be detected by non-destructive testing and thus the turbine will eventually have to be shut down and opened. Performance monitoring is the one method where the optimum time for performing restorative work can be determined where degradation affects fuel consumption or power output. In this way the decision to shut down for an overhaul can be based on sound technical evidence and economic evaluation. Once restorative work or modifications have been done, continuing monitoring of the performance can be used to justify future work (Beebe, 2003).

Condition monitoring techniques for steam turbines focus largely on mechanical tests such as vibration monitoring and oil analysis. Performance analysis is a less well known method of assessing the condition of turbines in service. Often performance analysis is the only method of detecting and monitoring certain modes of degradation. Because of the critical importance and large expenses associated with servicing steam turbines in the power generation sector, plant owners need to take all available information into account when assessing the technical and economic justification of taking these machines out of service. Performance analysis is the only method that can detect and diagnose problems such as deposition, erosion of blading and internal steam leakages (Beebe, 2003). Performance analysis allows the decision makers to determine the optimum time for restorative maintenance to be performed if the deterioration affects the consumption of fuel and/or the production of power.

It is possible to determine the performance from mechanical measurements made on steam turbine components during service outages; however it is clearly preferable to diagnose the issue prior to opening the turbine. Therefore, the decision to open a casing can be made if there is compelling evidence that justifies the action.

One of the main tests used to monitor steam turbine internal condition is the valve wide open (VWO) test. With the steam parameters set to a suitable datum value, typically rated values, the valves are fully opened as this is the only truly repeatable setting. From this point deviations in steam parameters through the various turbine stages can be identified. In one example an operator noticed that the control valves were running in the fully open position while the turbine was on its rated load. Most turbines have a larger capacity than the rating on the nameplate and in this case a VWO test confirmed that there was an increased steam consumption required to maintain the set load (Beebe, 2003).

In another example where a decreased VWO output was noted, the problem could be isolated to a specific section in the turbine by appropriate installation of measuring equipment. The reduction in output was attributed to blockage in the main steam strainers which could be serviced without opening the entire casing, thus saving significant cost to repair (Beebe, 2003).

One machine showed a significant reduction in VWO output and with the use of enthalpy drop efficiency calculations and stage pressure drop it was postulated that there was significant blade deposition in the intermediate section. During the shutdown procedure, the steam temperature was reduced to allow steam cooling of the turbine. The inspection revealed very little deposition. However upon returning the machine to service, it was found that the VWO output had returned to normal. This could be attributed to the steam washing effect achieved during forced cooling of the machine (Beebe, 2003).

From these examples it can be seen that condition monitoring can have a major impact on the technical and economic justification of outages. It is therefore important that the models and measurements are of an appropriate quality for the purpose. 1D models can contribute to condition monitoring at a suitable level of detail. Full 3D analysis would in some cases still be required during detailed investigations. By prior identification of problems and careful planning, outage time and cost can be reduced (Beebe, 2003).

2.9 Chapter summary

In the literature study several approaches to modelling the turbine process were investigated ranging from 1D simplified calculations to 3D CFD. Based on the literature it was apparent that a 1D approach is indeed a suitable methodology to achieve the objective of developing a model that can provide sufficient detail for engineering investigations while maintaining a level of

simplicity. Some authors have reported good results by discretising the calculation along the blade length, especially for long blades with a high aspect ratio.

The sources of loss in the turbine have been reviewed and several of the commonly applied loss calculation methods were investigated. These loss models typically bundle losses together that are dependent on the same variables and so the main fluid path losses can be modelled by the three main losses. Additional losses may be incurred due to complexity of real turbine geometry outside of the main steam path and these losses are included only when they apply to a specific turbine design. In the next chapter, the development and implementation of the model based on a 1D network approach will be discussed.

Chapter 3. Model development and implementation

3.1 Model fundamentals

3.1.1 Working principle and physical layout

A turbine may be defined as a form of heat engine in which the energy of the fluid is transformed into kinetic energy through nozzles and the kinetic energy of the resulting jet is in turn converted into force doing work on rings of blading mounted on a rotating part (Church, 1950). This is typically achieved in several stages of expansion from the turbine inlet to the exhaust. Figure 12 is a picture of a typical steam turbine being assembled with the internals visible.

Figure 12. A typical steam turbine being assembled (MAN Turbomachinery, 2016).

Figure 13 shows a typical flow path through a single stage of an axial turbine together with the relevant velocity vectors and velocity triangles at the inlet and outlet of the rotor blades.

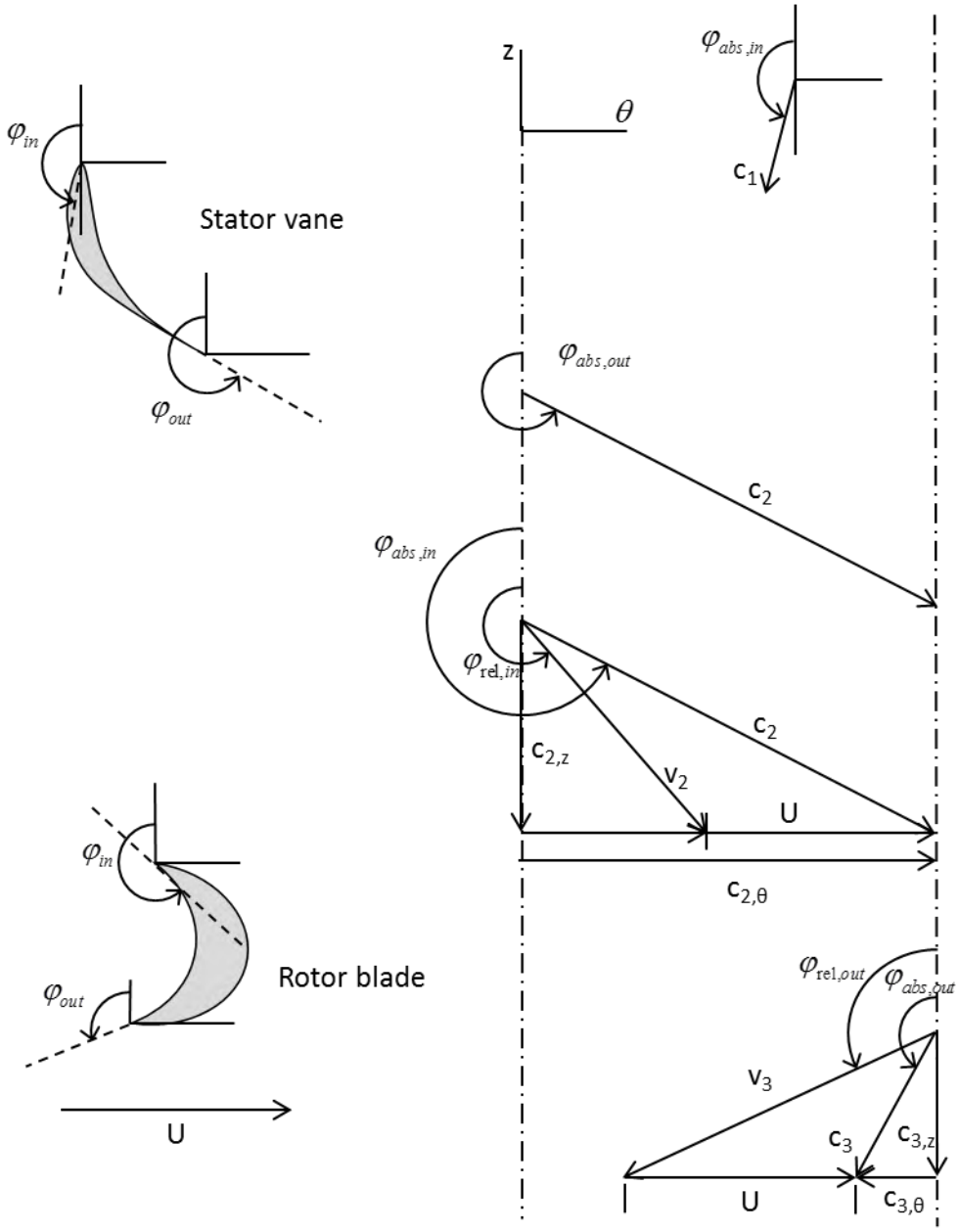

Figure 13. Axial turbine stage geometry and associated velocity diagram.

The nominally axial inlet flow is accelerated and redirected in the tangential direction by a turbine nozzle- or stator row. The flow then passes through a moving rotor row that guides the flow into the opposite tangential direction. The flow exits the rotor row with a nominally axial absolute velocity. The change in the tangential direction of the absolute velocity across the rotor stage represents the transfer of momentum from the fluid to the rotor and work done by the fluid on the rotor.

3.1.2 Fundamental definitions

To fully understand the process it is necessary to define absolute and relative velocities and to describe the thermodynamic relationship between static- and total properties for superheated steam.

Total enthalpy is defined as the static enthalpy plus the kinetic energy of the fluid:

$$h_0 = C_p T_0 = C_p T + \frac{1}{2} c^2 \tag{3.0}$$

$$h_0 = h + \frac{1}{2} c^2 \tag{3.1}$$

The relationship between absolute and relative velocity is obtained through the following velocity transformation:

$$\bar{c} = \bar{v} \ + \bar{U} \tag{3.1}$$

For compressible flow, the relationship between total- and static temperature and total- and static pressure is a function of the Mach number and the heat capacity ratio, γ :

$$\frac{T_0}{T} = 1 + \frac{\gamma - 1}{2} M^2 \tag{3.2}$$

$$p_0 = p\left(\frac{T_0}{T}\right)^{\frac{\gamma}{\gamma - 1}} \tag{3.3}$$

The flow process through the stator and rotor of a single stage is represented in Figure 14 on a Mollier diagram to illustrate the change in static and total enthalpy and pressure.

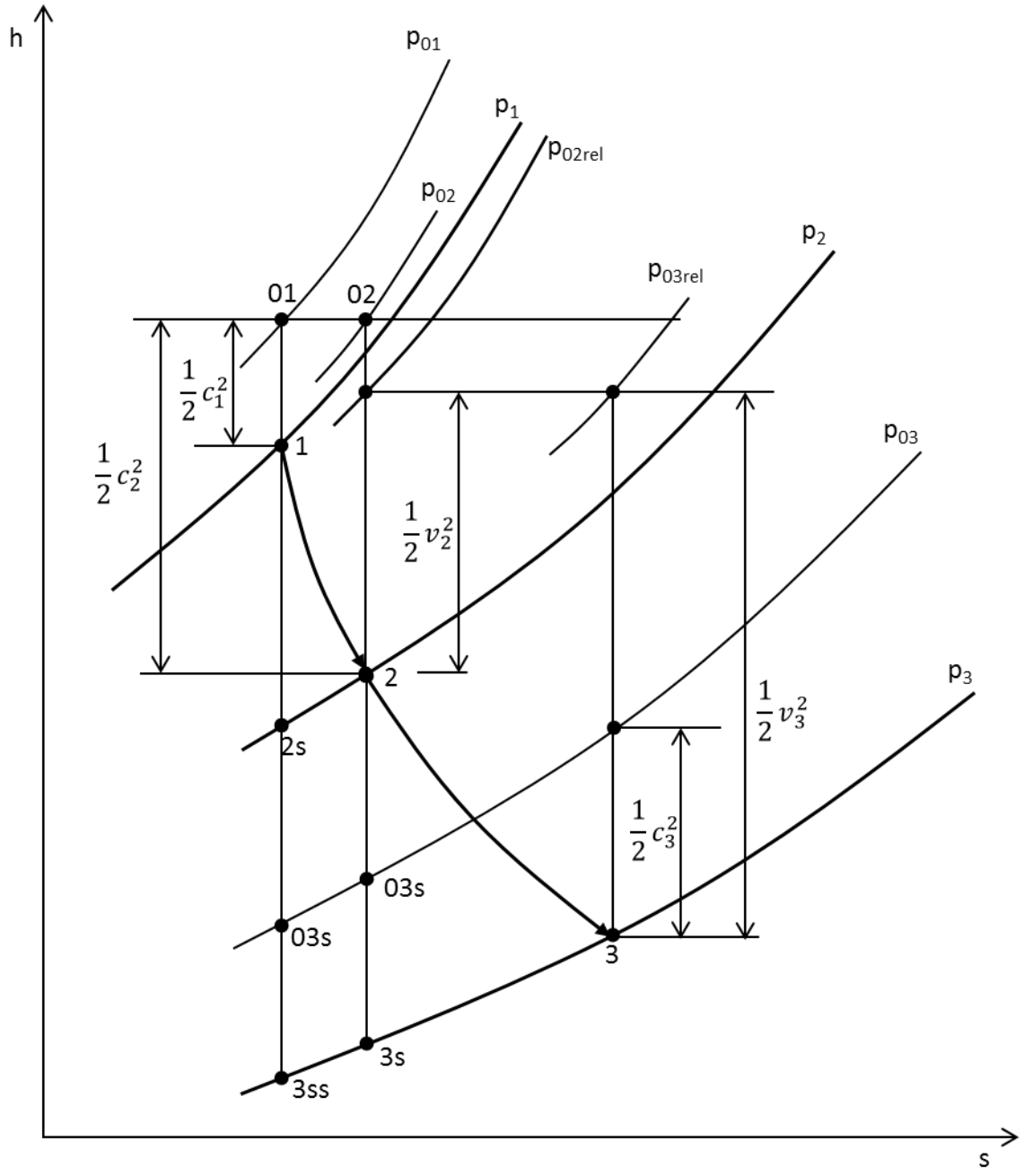

Figure 14. The expansion process through a typical turbine stage consisting of a stator(points 1-2) and rotor(points 2-3).

The process illustrated in Figure 14 will be analysed using fundamental conservation equations, but it is important to first understand how the turbine geometry and fluid angles are described so that a generic methodology can be developed.

3.1.3 Definition of coordinate system

The velocity diagrams in Figure 13 represent a 2D section through the turbine stage. Turbine profile data is usually supplied in the form of 2D cross sections of the blade at a few positions along the radial direction. Upon closer inspection of Figure 15 it becomes apparent that the flow is not necessarily 2D. Because of the expansion of the fluid there is also an increase in diameter of the turbine internal geometry along the length of the machine. The angle φ represents the stator and rotor angles in a 2D cross section of the blades, while ψ represents the angle of radial expansion of the inner casing of the turbine measured from the positive z-direction.

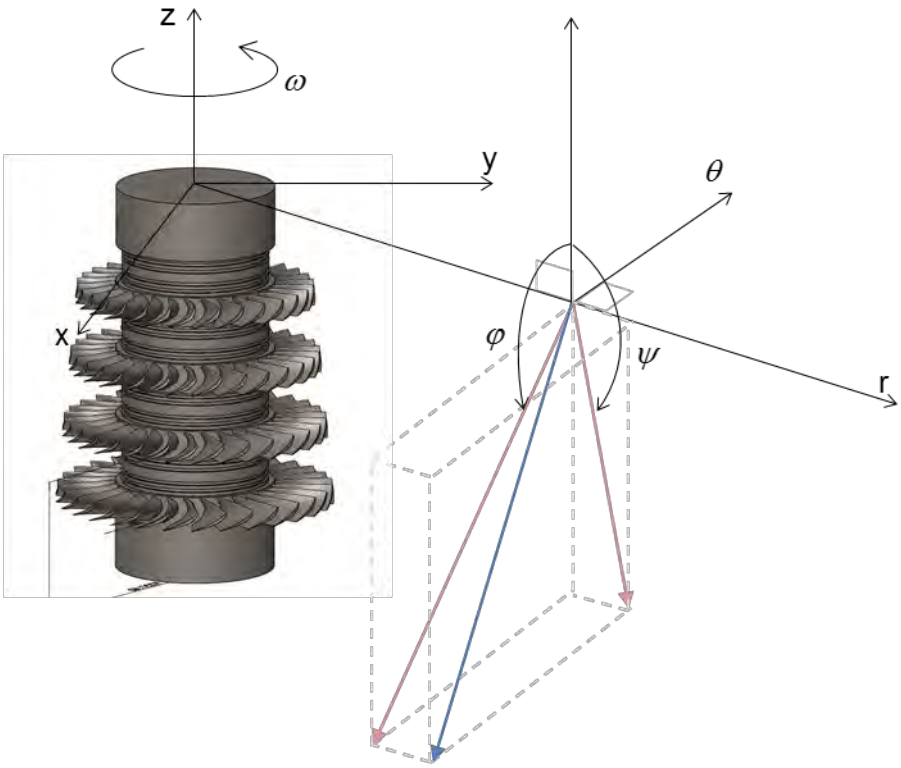

Figure 15. Diagram illustrating the projections of the flow vector to a plane parallel to a blade cross section and a plane parallel to a length-wise cross section of the turbine.

The geometric angles are defined for:

$$0 \le \varphi \le 2\pi$$
$$0 \le \psi \le 2\pi \tag{3.4}$$

The angles φ and ψ represent the axial turbine geometry well. However when analysing the resulting fluid vector, it is preferable to describe the flow in terms of a cylindrical coordinate system. In Figure 16 the fluid vector passing through the turbine is described in terms of a cylindrical coordinate system.

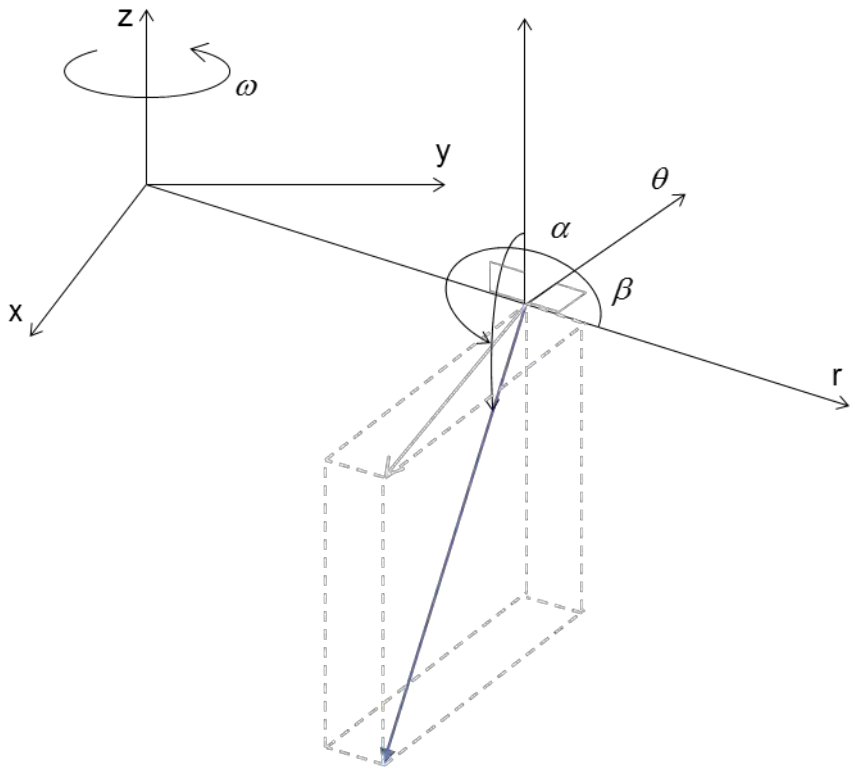

Figure 16. Figure of basic coordinate system with rotation around the z-axis. The vector to describe flow is also defined.

The rotation of the shaft is limited to one axis by its bearings. The z-direction represents this rotational axis and so the radial vector is always perpendicularly aligned to the z-direction. The velocity vector is defined by two angles, α and β. With:

$$\begin{aligned} 0 \le \alpha \le \pi \\ 0 \le \beta \le 2\pi \end{aligned} \tag{3.5}$$

This definition of the flow vector is generic and can be applied to any turbomachine. In Figure 17 the outlet flow of a radial machine is described using the same cylindrical coordinate system.

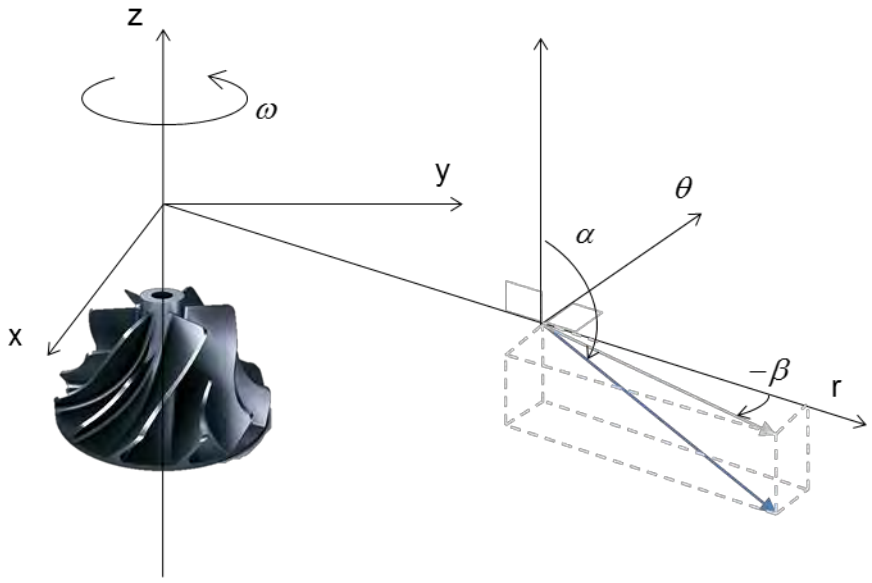

Figure 17. In the case of a radial machine, the same definitions apply. In this case the radial component of the flow dominates. (Impeller image from (Anon., 2015))

3.2 Conservation equations for a one-dimensional flow element

3.2.1 One-dimensional approximation

Figure 18 shows the typical flow domain through a single blade passage of an axial turbine. In the present model the flow channel between any two blades will be represented by a 1D flow element.

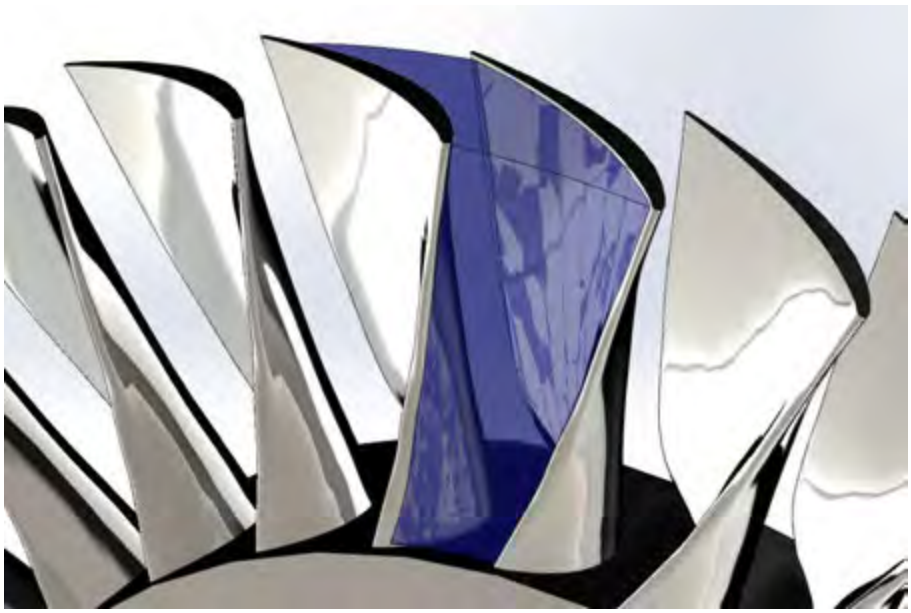

Figure 18. A representation of the flow domain between two blades coloured blue.

In a 1D flow element, the flow through any cross section of the element is described uniformly. Thus the inlet and exhaust areas and mean angles as well as the length and volume of the element fully describe its geometry. The flow element between two stator vanes are stationary and the flow element between two rotor blades rotate with the rotor.

While the fluid passes through this 1D flow element it is subjected to a thermofluid process. The fluid enters the element, is redirected, accelerated and performs useful work before it exits the element. If the flow element is defined to be a control volume, this process is governed by the laws of conservation because, mass, momentum and energy must be conserved.

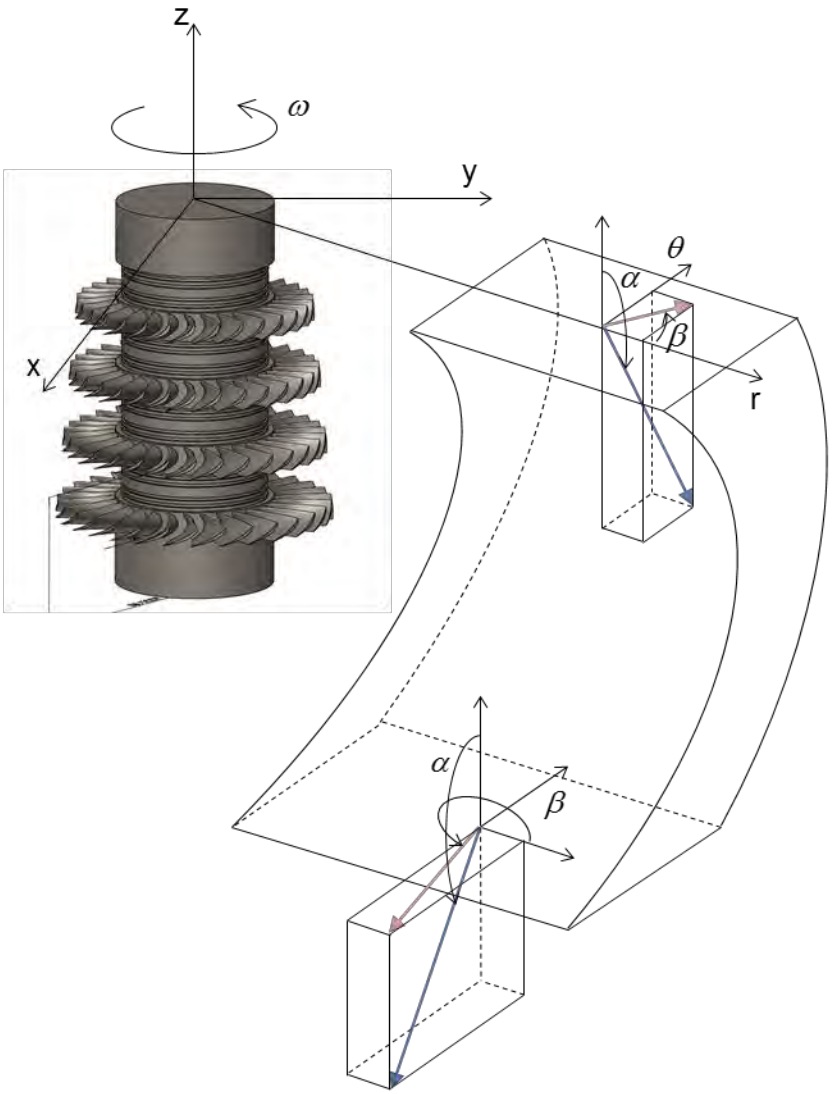

Figure 19. An example of how the flow vector through a 1D element of a rotor blade passage changes from inlet to outlet.

3.2.2 Conservation of mass

The conservation of mass means that the mass flow rates at all points in the element must be continuous so that it can be integrated with a control volume approach. Thus mass only enters and exits the control volume at its external boundaries. So for the control volume we can write (White, 2003):

$$\int_{CV} \frac{d\rho}{dt} d\forall + \int_{CS} \rho\left(\bar{v}.\hat{n}\right) dA = 0 \tag{3.6}$$

The analysis is simplified by defining the control volume surface to have only a number of 1D inlets and outlets. If we define $\hat{n}$ as the outward normal unit vector on the control surface, then $\bar{v}.\hat{n} = v_n$ for outflow and $\bar{v}.\hat{n} = -v_n$ for inflow (White, 2003). We can therefore write:

$$\int_{CV} \frac{d\rho}{dt} d\forall + \sum_i \left(\rho_i v_{n,i} A_i\right)_{out} - \sum_i \left(\rho_i v_{n,i} A_i\right)_{in} = 0 \tag{3.7}$$

which is equivalent to writing for the mass flow rates:

$$\int_{CV} \frac{d\rho}{dt} d\forall + \sum_i \left(\dot{m}_i\right)_{out} - \sum_i \left(\dot{m}_i\right)_{in} = 0 \tag{3.8}$$

In the steady state case, this can be further simplified to the sum of mass flow rates into and out of the control volume.

$$\sum_i \left(\dot{m}_i\right)_{out} - \sum_i \left(\dot{m}_i\right)_{in} = 0 \tag{3.9}$$

This mass flow rate is derived from the relative velocity of the flow and so the mass flow rate is actually a relative mass flow rate. Because the flow element representing the stator blade row are stationary and the flow element representing the rotor blade row rotate with the rotor, equation (3.9) will only be valid if the relative mass flow rate and the absolute mass flow rate can be used interchangeably. For the application of an axial turbomachine, the assumption is made that the cross sectional areas of flow are perpendicular to the axis of rotation such that the normal vector to the inlet areas has a zero component in the θ-direction. Because $\bar{U}$ perpendicular to the unit vector of area it can be determined from the velocity triangles that:

$$\int_A \rho \bar{v}.\hat{n} dA = \int_A \rho \bar{c}.\hat{n} dA \tag{3.10}$$

So mass flow rate from stationary and rotating elements can be summed directly at their connecting nodes.

$$\dot{m}_{rel} = \dot{m}_{abs} = \dot{m} \tag{3.11}$$

3.2.3 Conservation of momentum

The present model includes blade passages that are moving, or more specifically, rotating around the turbine axis. It is the angular momentum that represents work done on the fluid

and so linear momentum analysis alone is not sufficient to describe the physics that applies to a rotating control volume.

The analysis of angular momentum is performed in the non-inertial or rotational, reference frame. Keep in mind that the stagnation properties have been defined in the inertial reference frame and remain so in the non-inertial analysis. This is achieved by calculating stagnation properties from absolute velocities and not relative velocities.

The linear momentum equation is derived from Newton's second law and is given by (White, 2003).

$$\int_{CS} \tau dA + \int_{CV} B\rho d\forall - \int_{CV} \bar{a}_{rel} dm = \frac{d}{dt}\left(\int_{CV} \bar{v}\,\rho d\forall \right) + \int_{CS} \bar{v}\,\rho\left(\bar{v}.\hat{n}\right) dA \tag{3.12}$$

where

$$\bar{a}_{rel} = \frac{d^2R}{dt^2} + \frac{d\omega}{dt} \times \bar{r} + 2\omega \times \bar{r} + \omega \times \left(\omega \times \bar{r}\right)$$

$\frac{d^2R}{dt^2}$ is the acceleration of the non-inertial origin of coordinates *xyz.*

$\frac{d\omega}{dt} \times \bar{r}$ is the angular acceleration effect.

$2\omega \times \bar{r}$ is the Coriolis acceleration.

$\omega \times \left(\omega \times \bar{r}\right)$ is the centripetal acceleration.

Equation (3.12), can be developed for transient flows in a rotating channel with compressible flow and then integrated for an infinitesimal control volume to obtain the following equation for linear momentum conservation (Rousseau, 2013).

$$\frac{p_{avg}}{p_{0avg}}\left(p_{0,out} - p_{0,in}\right) + \frac{1}{2}\rho_{avg} c_{avg}^2 \frac{1}{T_{0avg}}\left(T_{0,out} - T_{0,in}\right) + \Delta p_{0L} + \rho_{avg} g\left(z_{out} - z_{in}\right) = \rho_{avg}\omega X \tag{3.13}$$

X represents the change in specific angular momentum through the element. Note that this equation was derived for a non-inertial reference frame with no linear acceleration of the origin. For stationary control volumes, $\omega = 0$ so the last term disappears and the equation becomes equivalent to the equation for the inertial frame.

Angular momentum conservation is also analysed through a control volume analysis. The equation is given by (White, 2003):

$$\sum M_o = \frac{d}{dt}\left(\int_{CV} (\bar{r} \times \bar{v}) \rho d\forall \right) + \int_{CS} (\bar{r} \times \bar{v}) \rho (\bar{v}.\hat{n}) dA \tag{3.14}$$

Equation (3.14) can be developed by noting that the origin has no linear acceleration, neglecting second order body force terms and integrating over the length of the control volume to obtain the integral form in terms of mass flow rate given by (Rousseau, 2013):

$$\begin{aligned} M_z = {} & \rho\forall \left(\frac{d\bar{v}}{dt} r \sin\beta \sin\alpha + \dot{\omega}^2 r \right) + \left(\left(p_{out} A_{out} r_{out} - p_{in} A_{in} r_{in} \right) - \rho g A r (z_{out} - z_{in}) \right) \sin\alpha \sin\beta \\ & + \dot{m} \left(\omega \left(r_{out}^2 - r_{in}^2 \right) + \left(v_{out} r_{out} \sin\alpha_{out} \sin\beta_{out} - v_{in} r_{in} \sin\alpha_{in} \sin\beta_{in} \right) \right) \end{aligned} \tag{3.15}$$

In the case of a turbine the control volume is rotating around the *z*-axis and the inlet and outlet area vectors are oriented in such a way as to be in the *rz*-plane. In other words the area vector has a zero component in the θ-direction. One way to visualize such surfaces is to say that they are surfaces that can be formed by a machining operation on a lathe. The result is that the static pressure acting on the inlet and outlet surface cannot contribute to the moment about the axis of rotation. The element is rotating and thus the gravitational term would be changing sign at the frequency of rotation. Since the gas density is relatively low the gravitational term can also be neglected in this analysis to obtain the moment about the *z*-axis given by (Rousseau, 2013):

$$M_z = \rho\forall \left(\frac{d\bar{v}}{dt} r \sin\beta \sin\alpha + \dot{\omega}^2 r \right) + \dot{m} \left(\omega \left(r_{out}^2 - r_{in}^2 \right) + \left(v_{out} r_{out} \sin\alpha_{out} \sin\beta_{out} - v_{in} r_{in} \sin\alpha_{in} \sin\beta_{in} \right) \right) \tag{3.16}$$

In the steady state case, the net change in specific angular momentum, X, can be written as (Rousseau, 2013):

$$X = \omega \left(r_{out}^2 - r_{in}^2 \right) + \left(\sin\alpha_{out} \sin\beta_{out} v_{out} r_{out} - \sin\alpha_{in} \sin\beta_{in} v_{in} r_{in} \right) \tag{3.16}$$

3.2.4 Conservation of energy

The final conservation law that is applied is the first law of thermodynamics which describes the conservation of energy (White, 2003).

$$\dot{Q}-\dot{W}=\frac{\partial}{\partial t}\left(\int_{CV}\left(\bar{u}+\frac{1}{2}c^2+gz\right)\rho d\forall\right)+\int_{CS}\left(\bar{h}+\frac{1}{2}c^2+gz\right)\rho\left(\bar{v}.\hat{n}\right)dA \tag{3.17}$$

$\dot{Q}$ is the total rate of heat transfer to the fluid.

$\dot{W}$ is the total rate of work done by the fluid.

By substituting total enthalpy from the definition, equation (3.1), integrating over the length of the control volume, we obtain the equation given by (Rousseau, 2013):

$$\dot{Q}+M_z\omega=\forall\frac{\partial}{\partial t}\left(h_0-\frac{p}{\rho}\right)+\dot{m}\left(h_{0,out}-h_{0,in}\right) \tag{3.18}$$

3.2.5 Definition of turbine loss coefficient

In order to complete the linear momentum conservation equation (3.13), a pressure loss term is required. The pressure loss term is the key to ensuring that the simplified 1D model takes the complex flow phenomena that lead to losses into account. In their work, Ainley and Mathieson (1951) defined the pressure loss coefficients such as the profile loss, secondary loss and leakage loss, for turbine stages appear at the exit of the stage. This convention was also followed by other authors who revised their work and also many other authors who developed different loss models. The pressure loss coefficient relates to kinetic energy that is lost during the process and can be defined by the total pressure lost in a process.

$$Y_{loss}=\frac{p_{0,in}-p_{0,\text{out}}}{p_{0,out}-p_{out}} \tag{3.19}$$

If we define the total pressure loss as:

$$\Delta p_{0,loss}=p_{0,in}-p_{0,\text{out}} \tag{3.20}$$

We can write equation (3.20) in terms of the fluid Mach number:

$$\Delta p_{0,loss}=Y_{loss}p_{out}\left(\frac{p_{0,\text{out}}}{p_{out}}-1\right) \tag{3.21}$$

$$\Delta p_{0,loss}=Y_{loss}p_{out}\left((1+\frac{\gamma-1}{2}M_{out}^2)^{\frac{\gamma}{\gamma-1}}-1\right) \tag{3.21}$$

The total pressure loss is thus a function of the velocity and therefore if the density is known, of the mass flow rate. Thus we can rewrite the mass flow rate as a function of the total pressure at the inlet and at the exhaust (see paragraph 3.4.5 for detail):

$$\dot{m} = f\left(p_{0,in}, p_{0,\text{out}}\right) \tag{3.22}$$

The loss coefficient in equation (3.19) is defined at the stage exit, but other loss models exist that defines losses at the inlet of a control volume or using the average pressures. In order to ensure that the model remains generic, all three definitions of pressure loss are included in the model. Examples are the losses caused by cavities and surface friction losses respectively. The total pressure loss then becomes the sum of all the losses applicable to a specific flow element.

$$\Delta p_{0,loss} = Y_{loss,in}\left(p_{0in} - p_{in}\right) + Y_{loss,avg}\left(p_{0avg} - p_{avg}\right) + Y_{loss,\text{out}}\left(p_{0out} - p_{out}\right) \tag{3.23}$$

3.3 Thermofluid network approach

Now that the flow through a 1D control volume has been described we can look at the complete turbine and consider that it is made up of a system of 1D flow elements; nozzle rows,

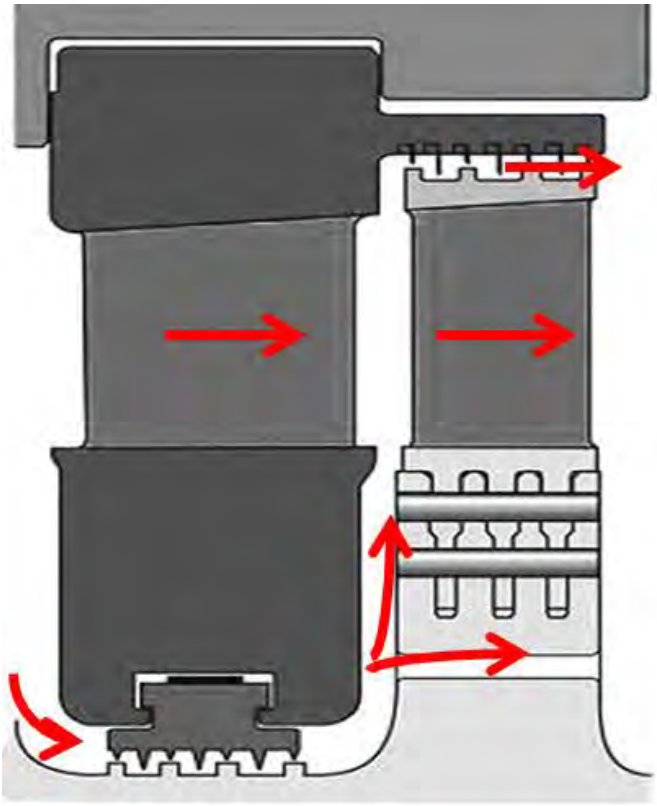

Figure 20. An example of how individual flow paths are developed from the turbine geometry.

rotor rows, sealing strips and other passages where the flows interact. In Figure 20 a cross section of a single stage is illustrated. The arrows indicate individual flow paths in the stage. Each of these flow paths can be represented by a unique control volume. By connecting each of the 1D control volumes through nodes a network of control volumes can be developed that describes all the flow paths in the turbine.

This results in a network, illustrated in Figure 21, of discretised nodes and elements with the elements forming the connections between nodes. In the present model a pressure correction scheme is utilised to solve the pressure, temperature and velocity distribution throughout the network.

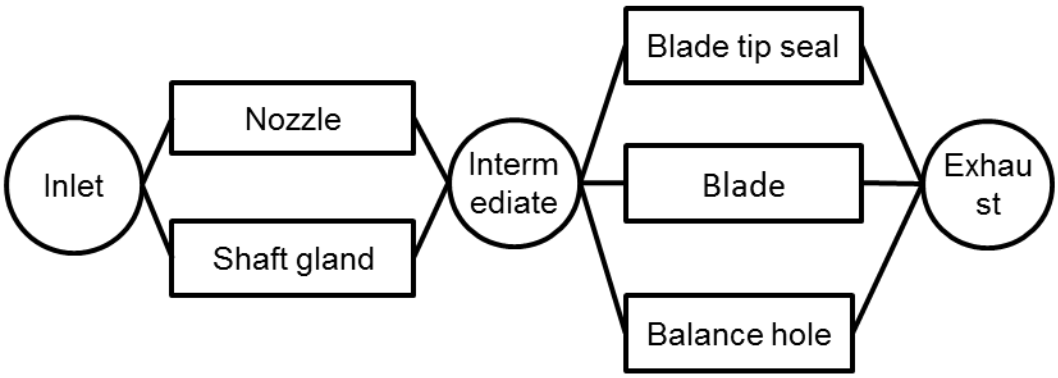

Figure 21. Representative network model

By substituting the equation for conservation of momentum into the equation for conservation of mass, an expression can be developed for each node wherein nodal pressures are the unknowns. The properties of the flow that are required to complete the equations are calculated using the initial guess values and are updated within each iteration. Therefore, the fluid properties are treated as constants within each iteration while solving for the total pressures. The mass flow rates are then calculated from the pressure loss equation for each element. Once the pressure and mass flow rate distributions have been determined, an energy balance is performed at each node to account for work done on the fluid.

3.3.1 Nodes, elements and connectivity

The method envisaged here reminds one of the type of method first developed by Hardy Cross in 1936 (Greyvenstein & Laurie, 1994). In the Hardy Cross method, pipe network flow problems are solved by describing the network in terms of loops and calculating pressure drops and flow

rates for each loop. The advent of computers has allowed the concept to be developed further to include methods where the equations for nodes and elements are considered. Node methods are also used in CFD to calculate flows by solving the Navier-Stokes equations (Greyvenstein & Laurie, 1994). The present method is a node method solved numerically through a Newton-Raphson method. The elements are used to describe flow physics of each individual control volume where the boundaries to these control volumes are connected by nodes. The nodes are then used to ensure that the complete flow field represented by individual elements is continuous so that mass flows and momentum from connected elements are balanced.

The summing procedure can be performed simultaneously for all nodes by using the unique description of the flows given in the connectivity matrix.

The basic procedure then becomes:

- Guess initial temperature and pressure distribution and calculate initial mass flow rates.
- Calculate pressures at nodes by simultaneously solving continuity and conservation of momentum.
- Calculate new mass flow rates.
- Repeat the procedure until convergence is reached.
- Perform an energy balance using the calculated mass flow rates.
- Calculate new temperatures from the energy balance.
- Repeat the procedure from the start until the convergence is reached.

The temperature is assumed to remain constant during the simultaneous solution of the mass flow rates.

3.3.2 Computational mesh

A mass flow rate is described by each element and elements are therefore directional. The inter-connectivity between elements and nodes can be described by a connectivity matrix which becomes very useful for the simultaneous solution of the conservation equations. Because the network is not structured the numbering of elements and nodes is arbitrary. A simple network and connectivity matrix is shown in Figure 22 and Table 1 to illustrate the method:

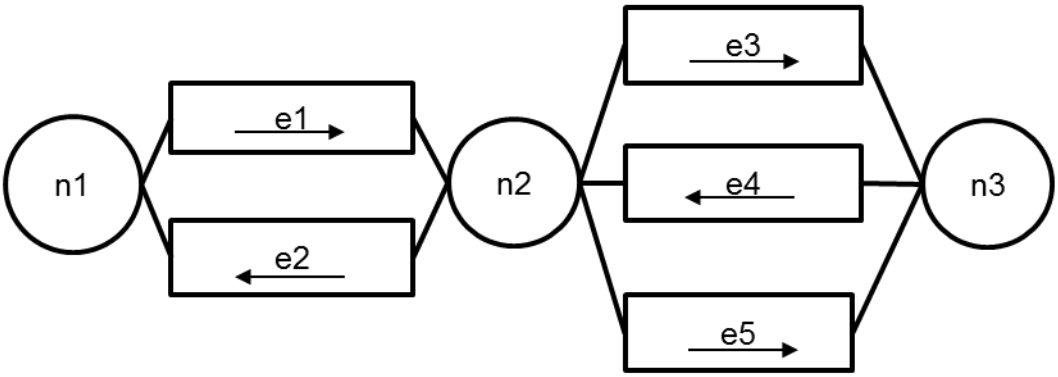

Figure 22. The network model in terms of nodes and elements.

Table 1 Example connectivity matrix.

	E_1	E_2	E_3	E_4	E_5
N_1	-1	1	0	0	0
N_2	1	-1	-1	1	-1
N_3	0	0	1	-1	1

In the example it can be seen that the elements have a direction assigned to them. This is merely an assumed direction and the implication is that if the calculated flow is in the opposite direction, the resulting mass flow rate will have a negative sign. In a matrix format each row represents a node and each column represents an element. If an element is connected to a node, the corresponding position in the matrix is assigned a value of '1'. The next evaluation is to determine if the element flows into or out of the node. The '1' value is then given a sign accordingly, so that flows out of a node are designated by a '-1' in the connectivity matrix.

3.3.3 Discretisation on a row-by-row basis

In the discussion above a single stage of the turbine was discretised into flow elements to represent the main parts of a stage namely; a nozzle flow, a rotor flow, a labyrinth seal flow and a tip leakage flow. This scheme can be expanded to include all the stages of the turbine

connected by nodes in-between each stage to create a model of the complete turbine discretised on a row-by-row basis.

3.3.4 Discretisation along the length of a blade

In the discussion above it was also assumed that the flow path between each set of blades would be represented by a single 1D flow element. However, as described in the literature review, it may be appropriate in some cases to also discretise along the length of the blade because blade angles and velocity triangles can vary significantly from root to tip. The resulting flows are not necessarily approximated well by a single 1D element based only on the geometrical parameters at the mean diameter. A model can be developed by discretising the blade passage further into several 1D elements based on the geometrical parameters at the mean diameter of each element. Such a discretisation scheme may improve the accuracy of the predicted losses. It may also prove to be useful in off-design cases where deformation of the flow path is limited to specific regions of the blade, like erosion of the tip area for example. Discretisation along the blade length is illustrated in Figure 23 and the representative network model for a stage with such a discretisation scheme is illustrated in Figure 24.

Figure 23. A representation of how the flow domain between two blades can be further discretised along the length of the blade into multiple 1D elements.

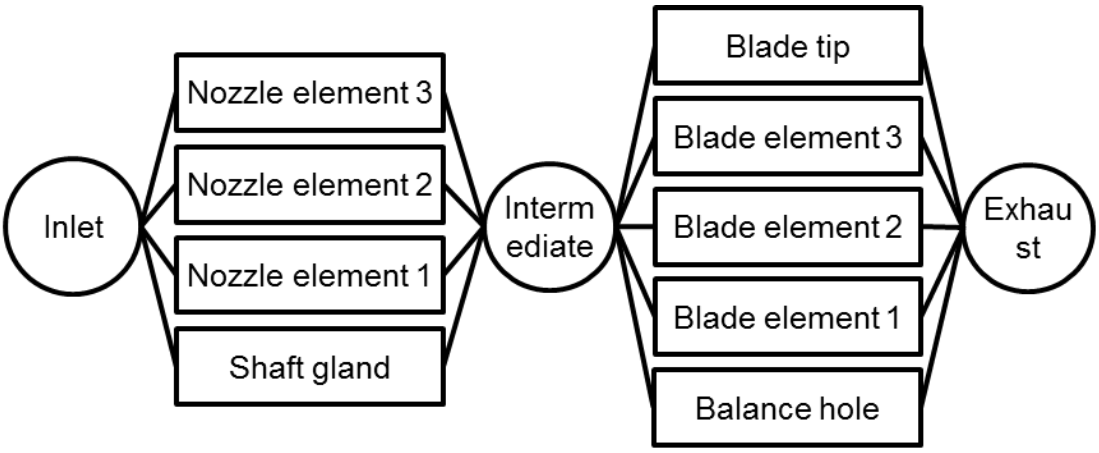

Figure 24. A representative network model of a turbine with several flow elements along the length of the blade.

3.4 Program algorithm

3.4.1 Model development

The model is developed and coded in Scilab. Although commercial network solvers are available, control over all aspects of the implementation for this specific application is best achieved by developing the code from scratch. Scilab is free and open source software that provides a powerful platform for numerical computation of engineering and scientific applications. Scilab is widely used in secondary and higher education institutions for teaching mathematics, engineering sciences and automatic control engineering. The turbine program is made up of several sub programs and functions to input the data, process the data, define the applicable functions, run the pressure correction subroutine, run the energy balance subroutine and finally to process the results. This process is summarised at the end of the chapter in Figure 26.

3.4.2 Application of Momentum and mass conservation to the network

Application of the combined momentum and mass conservation equations in the network can be explained with the aid of the simple generic example network in Figure 25. In this figure nodes are represented by circles and elements are represented by squares. The arrows represent the direction of flows through the elements that has to be assumed when setting up the network. This may differ from the result that will be calculated. The example network represents nodes with single and multiple inlets and outlets as well as single and multiple elements in parallel.

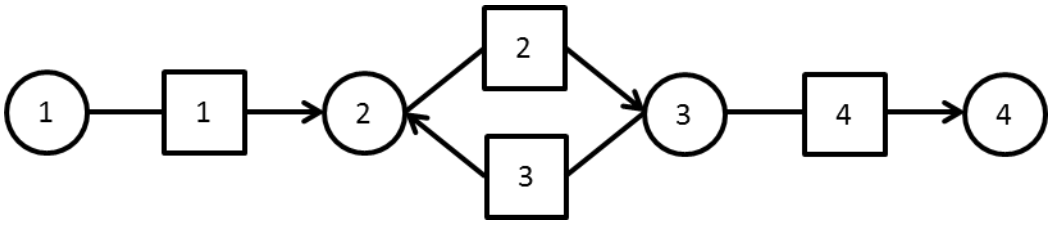

Figure 25. Example network

One can describe the connections between nodes and elements in the network with a connectivity matrix. A 1 or -1 represent a connection of an element into and out of a node respectively. For any matrix element, C_{NE}, N represents the node number and E the element number.

Table 2. A connectivity matrix developed for the example network in Figure 25.

	E_1	**E_2**	**E_3**	**E_4**
N_1	-1	0	0	0
N_2	1	-1	1	0
N_3	0	1	-1	-1
N_4	0	0	0	1

	E_1	**E_2**	**E_3**	**E_4**
N_1	C_{11}	C_{12}	C_{13}	C_{14}
N_2	C_{21}	C_{22}	C_{23}	C_{24}
N_3	C_{31}	C_{32}	C_{33}	C_{34}
N_4	C_{41}	C_{42}	C_{43}	C_{44}

Once the network has been defined in this way, initial values of all the variables in the conservation of mass and momentum equations are guessed. Continuity and conservation of momentum is then simultaneously applied to the network and a set of equations is developed for every node in the network. This set of equations can then be solved for the unknown variables. This process is described in detail below.

In paragraph 3.2.5, the relationship between the mass flow rate and pressure loss term was illustrated. If we substitute equation (3.22) into the momentum equation we obtain a relationship between nodal pressures and element mass flows for the network. This equation will be developed in paragraph 3.4.5, but for the moment we can consider the resulting equation to consist of a mass flow rate, a coefficient of the $\left(p_{0,out} - p_{0,in}\right)$ term plus the additional terms, summed and called 'const' for each element:

$$\dot{m}_E = coeff_E\left(-\sum C_{NE} p_{0,N}\right) + const_E \tag{3.24}$$

Conservation of mass is applied at every internal node of the network, equation (3.9) to each node in the network to obtain:

$$\sum_E C_{NE}\dot{m}_E = 0 \tag{3.25}$$

Equation (3.24) is tested for elements 1 and 3 with appropriate values, C_{NE}, from the connectivity matrix:

$$\begin{aligned}\dot{m}_1 &= coeff_1\left(-C_{11}p_{0,1} - C_{21}p_{0,2} - C_{31}p_{0,3} - C_{41}p_{0,4}\right) + const_1\\ &= coeff_1\left(p_{0,1} - p_{0,2}\right) + const_1\end{aligned} \tag{3.26}$$

$$\begin{aligned}\dot{m}_3 &= coeff_3\left(-C_{13}p_{0,1} - C_{23}p_{0,2} - C_{33}p_{0,3} - C_{43}p_{0,4}\right) + const_3\\ &= coeff_3\left(p_{0,3} - p_{0,2}\right) + const_3\end{aligned}$$

Equation (3.25) is tested in a similar manner for node 2 and 3:

$$\begin{aligned}&C_{21}\dot{m}_1 + C_{22}\dot{m}_2 + C_{23}\dot{m}_3 + C_{24}\dot{m}_4 = 0\\ &\dot{m}_1 - \dot{m}_2 + \dot{m}_3 = 0\end{aligned} \tag{3.27}$$

$$\begin{aligned}&C_{31}\dot{m}_1 + C_{32}\dot{m}_2 + C_{33}\dot{m}_3 + C_{34}\dot{m}_4 = 0\\ &\dot{m}_2 - \dot{m}_3 - \dot{m}_4 = 0\end{aligned}$$

Now if we substitute equation (3.24) into (3.25) for each internal node we get:

$$\sum_E C_{NE}\left[coeff_E\left(-\sum_N C_{NE} p_{0,N}\right) + const_E\right] = 0 \tag{3.28}$$

Equation (3.28) is tested for the example network for all the internal nodes:

$$\begin{aligned}
&C_{21}\left[\, coeff_1\left(-C_{11}p_{0,1}-C_{21}p_{0,2}-C_{31}p_{0,3}-C_{41}p_{0,4}\right)+const_1\,\right]+\\
&C_{22}\left[\, coeff_2\left(-C_{12}p_{0,1}-C_{22}p_{0,2}-C_{32}p_{0,3}-C_{42}p_{0,4}\right)+const_2\,\right]+\\
&C_{23}\left[\, coeff_3\left(-C_{13}p_{0,1}-C_{23}p_{0,2}-C_{33}p_{0,3}-C_{43}p_{0,4}\right)+const_3\,\right]=0
\end{aligned}$$

$$\begin{aligned}
&C_{31}\left[\, coeff_1\left(-C_{11}p_{0,1}-C_{21}p_{0,2}-C_{31}p_{0,3}-C_{41}p_{0,4}\right)+const_1\,\right]+\\
&C_{32}\left[\, coeff_2\left(-C_{12}p_{0,1}-C_{22}p_{0,2}-C_{32}p_{0,3}-C_{42}p_{0,4}\right)+const_2\,\right]+\\
&C_{33}\left[\, coeff_3\left(-C_{13}p_{0,1}-C_{23}p_{0,2}-C_{33}p_{0,3}-C_{43}p_{0,4}\right)+const_3\,\right]=0
\end{aligned}$$

(3.29)

Next, the terms of p_0 that represent the same node are collected so that the equations can be simplified:

$$\begin{aligned}
&\begin{bmatrix} -C_{21}coeff_1C_{11} \\ -C_{22}coeff_2C_{12} \\ -C_{23}coeff_3C_{13} \end{bmatrix} p_{0,1} + \begin{bmatrix} -C_{21}coeff_1C_{21} \\ -C_{22}coeff_2C_{22} \\ -C_{23}coeff_3C_{23} \end{bmatrix} p_{0,2} + \begin{bmatrix} -C_{21}coeff_1C_{31} \\ -C_{22}coeff_2C_{32} \\ -C_{23}coeff_3C_{33} \end{bmatrix} p_{0,3} + \begin{bmatrix} -C_{21}coeff_1C_{41} \\ -C_{22}coeff_2C_{42} \\ -C_{23}coeff_3C_{43} \end{bmatrix} p_{0,4} + \begin{bmatrix} C_{21}const_1 \\ C_{22}const_2 \\ C_{23}const_3 \end{bmatrix} = 0\\
&\begin{bmatrix} -C_{31}coeff_1C_{11} \\ -C_{32}coeff_2C_{12} \\ -C_{33}coeff_3C_{13} \end{bmatrix} p_{0,1} + \begin{bmatrix} -C_{31}coeff_1C_{21} \\ -C_{32}coeff_2C_{22} \\ -C_{33}coeff_3C_{23} \end{bmatrix} p_{0,2} + \begin{bmatrix} -C_{31}coeff_1C_{31} \\ -C_{32}coeff_2C_{32} \\ -C_{33}coeff_3C_{33} \end{bmatrix} p_{0,3} + \begin{bmatrix} -C_{31}coeff_1C_{41} \\ -C_{32}coeff_2C_{42} \\ -C_{33}coeff_3C_{43} \end{bmatrix} p_{0,4} + \begin{bmatrix} C_{31}const_1 \\ C_{32}const_2 \\ C_{33}const_3 \end{bmatrix} = 0
\end{aligned}$$

(3.30)

Equation (3.30) can also be written as:

$$\begin{aligned}
a_{21}p_{01}+a_{22}p_{02}+a_{23}p_{03}+a_{24}p_{04}+b_2=0\\
a_{31}p_{01}+a_{32}p_{02}+a_{33}p_{03}+a_{34}p_{04}+b_3=0
\end{aligned}$$

(3.31)

where:

$$a_{ij} = -\sum_E C_{iE} coeff_E C_{jE}$$
$$b_i = \sum_E C_{iE} const_E \tag{3.32}$$

The result is the same number of equations as the number of unknown pressures to be solved for, because two of the four unknown pressures are boundary values that are known:

$$\Phi_2\left(p_{0,1}, p_{0,2}, p_{0,3}, p_{0,4}\right) = \sum_N a_{2N} p_{0,N} + b_2 = 0$$
$$\Phi_3\left(p_{0,1}, p_{0,2}, p_{0,3}, p_{0,4}\right) = \sum_N a_{3N} p_{0,N} + b_3 = 0 \tag{3.33}$$

The unknowns are solved by using the Newton-Raphson method:

$$\frac{\partial \Phi_2}{\partial p_{0,2}} \Delta p_{0,2} + \frac{\partial \Phi_2}{\partial p_{0,3}} \Delta p_{0,3} = -\Phi_2$$
$$\frac{\partial \Phi_3}{\partial p_{0,2}} \Delta p_{0,2} + \frac{\partial \Phi_3}{\partial p_{0,3}} \Delta p_{0,3} = -\Phi_3 \tag{3.34}$$

where $\Delta p_{0,\mathrm{j}}$ is the pressure correction required to obtain the solution. And where:

$$\frac{\partial \Phi_j}{\partial p_{0,\mathrm{j}}} = \frac{\Phi_j\left(1.01 p_{0,j}\right) - \Phi_i\left(0.99 p_{0,j}\right)}{1.01 p_{0,j} - 0.99 p_{0,j}} \tag{3.35}$$

Equation (3.35) can be written in matrix form:

$$\begin{bmatrix} \frac{\partial \Phi_2}{\partial p_{0,2}} & \frac{\partial \Phi_2}{\partial p_{0,3}} \\ \frac{\partial \Phi_3}{\partial p_{0,2}} & \frac{\partial \Phi_3}{\partial p_{0,3}} \end{bmatrix} \begin{bmatrix} \Delta p_{0,2} \\ \Delta p_{0,3} \end{bmatrix} = \begin{bmatrix} -\Phi_2 \\ -\Phi_3 \end{bmatrix} \tag{3.36}$$

The built-in Scilab function for right-matrix division is used to solve for the pressure correction vector, $\Delta p_{0,j}$. Right-matrix division is analogous to inverting a matrix equation to solve for the unknowns. In equation (3.37), the pressure corrections are added to the initial value of the pressures to obtain a new value of nodal pressures and the process is repeated until the solution converges. During each iteration the new values of nodal pressure are used to update

the mass flow rate associated with the pressure difference between two nodes, from equation(3.24). From the new mass flow rate, the fluid Mach number can be updated and the static pressure, temperature and thus density can be updated. To assist with convergence a relaxation parameter, R, is applied to the pressure correction.

$$\begin{bmatrix} p_{0,2} \\ p_{0,3} \end{bmatrix} = \begin{bmatrix} p_{0,2}{}^{o} \\ p_{0,3}{}^{o} \end{bmatrix} + R \begin{bmatrix} \Delta p_{0,2} \\ \Delta p_{0,3} \end{bmatrix} \tag{3.37}$$

The 'o' superscript denotes the nodal pressure value of the preceding iteration.

3.4.3 Energy conservation calculation

The implementation of energy conservation will also be explained by using the same example in Figure 25. For every element and node the energy balance equation must hold. In the network, nodes are used to sum and balance energy from connected elements while elements are used to describe heat transfer and work performed on the fluid. To this end it is assumed that no work is done and no heat is transferred within a node. So we can simplify equation (3.18) for every node:

$$\dot{m}\left(h_{0,\text{out}} - h_{0,in}\right) = 0 \tag{3.38}$$

or for multiple flows into and out of the node:

$$\sum_{E} \left(\dot{m}_E h_{0,E}\right)_{in,\text{N}} - \sum_{E} \left(\dot{m}_E h_{0,E}\right)_{\text{out,N}} = 0 \tag{3.39}$$

It is assumed that the flows into the node from upstream elements are properly mixed in the node such that all the flows out of the node and into its downstream connected elements have the same enthalpy as the node itself:

$$\sum_{E} \left(\dot{m}_E h_{0,E}\right)_{in,\text{N}} - h_{0,N} \sum_{E} \left(\dot{m}_E\right)_{\text{out,N}} = 0 \tag{3.40}$$

Enthalpy flowing into the node is determined by the heat transfer and work performed on the fluid in the upstream elements. An energy balance can be performed for each upstream element to determine the enthalpy flowing out of the upstream elements and into the node. By substituting equation (3.18), equation (3.40) can also be written for the steady state case as:

$$\sum_{E}\left(\dot{m}_E h_{0,N(upstream)} + \dot{Q}_E + \dot{W}_E\right)_{in,\mathrm{N}} - h_{0,N}\sum_{E}\left(\dot{m}_E\right)_{\mathrm{out,N}} = 0 \tag{3.41}$$

From a programming perspective it means that the calculation requires a distinction between elements that are connected upstream of the node and those connected downstream. The connectivity matrix provides the connections, but utilises an assumed direction of the flows and so would result in an erroneous calculation of nodal enthalpies if the real direction of the flow differs from the assumed direction. It is quite possible for the real direction of the flow to be different to the assumed direction because a term is included in the momentum equation for work done on the fluid which can in effect oppose the pressure gradient. Thus it is necessary to determine what the real direction of the flows are and therefore what the real connectivity matrix is, because clearly, enthalpy flowing into a node and out of a node cannot be dealt with simply by a sign convention.

The following calculations may appear trivial, but because they are repeated in each iteration it is very important that they are performed efficiently. Testing each element using loops and selection statements for example would be too time consuming and significantly retard the solving time. Therefore it was endeavoured to perform all calculations by only utilising matrix operations.

To determine what the real direction of the flow is, as opposed to the assumed direction, we can calculate a unit vector of flow direction using the calculated mass flow rate vector for the network and elementwise division. Positive unit vectors indicate that the flow is indeed in the same direction as the assumed flow direction and vice versa:

$$\hat{\dot{m}} = \frac{\dot{m}_E}{\left|\dot{m}_E\right|} \tag{3.42}$$

This real flow direction can now be used to calculate a real connectivity matrix. This is done for each node by calculating the unit flow direction multiplied by the connectivity to obtain the real connectivity matrix.

$$C_N^{real} = C_N.\hat{\dot{m}} \tag{3.43}$$

Next the real connectivity matrix is separated into two matrixes that represent the 'in' flows and 'out' flows for the nodes, namely; $C^{real,in}$ and $C^{real,\text{out}}$. In Scilab this is implemented by deleting positive and negative terms from the matrices respectively using a simple calculation:

$$\begin{aligned} &C_{NE}^{real,in} = \left(C_{NE} + 1\right)/2 \\ &and \\ &C_{NE}^{real,out} = -\left(C_{NE} - 1\right)/2 \end{aligned} \tag{3.44}$$

It is also important to note that the energy conservation problem has a boundary value at the inlet only and therefore the unknown nodal enthalpies include the outlet node or nodes. So it is necessary to determine which nodes are sources of mass flow and which nodes are sinks of mass flow. Sources are nodes where mass flow enters into the network and sinks are nodes where mass flow leaves the network. Again this may seem trivial because a turbine has a defined inlet and exhaust. However, the network solution of the mass flow rate is based on the pressure gradient and the work done on the fluid. Depending on the magnitude of those variables, the mass flow rate could be positive or negative for an arbitrary network. This means that the solution can include reverse flows in a turbine, although losses associated with such flows have not formed part of the scope of the present work. The program checks if the mass balance at each node is positive, negative or zero. Positive indicates that the node has more mass flowing in, thus it is a source. Internal nodes will have a mass balance value of zero, because of continuity. The calculation is done by multiplying the each row of the connectivity matrix with the mass flow rate vector resulting in the mass balance for each node.

$$massbalance_N = \sum_N C_{NE}^{real} \dot{m}_E \tag{3.45}$$

A method has thus been developed to determine $N_{upstream}$ for each node in terms of the actual flow direction. Equation (3.41) for each node then becomes:

$$\sum_{NE}\left(C_{NE}^{real,in}\dot{m}_E C_{NE}^{real,out} - C_{NE}^{real,\text{out}}\dot{m}_E\right)h_{0,\text{N}} + \sum_{NE}\left(C_{NE}^{real,in}\left(\dot{Q}_E + W_E\right)\right) = h_{0,\text{BC}} \tag{3.46}$$

The equation can be tested for the network by using the example network. Assuming a pressure drop from node 1 to node 4, the variables are:

$$C = \begin{bmatrix} -1 & 0 & 0 & 0 \\ 1 & -1 & 1 & 0 \\ 0 & 1 & -1 & -1 \\ 0 & 0 & 0 & 1 \end{bmatrix} \tag{3.47}$$

$$\dot{m} = \begin{bmatrix} \dot{m}_1 \\ \dot{m}_2 \\ -\dot{m}_3 \\ \dot{m}_4 \end{bmatrix} \tag{3.48}$$

Thus the unit vector of flow direction is:

$$\hat{\dot{m}} = \begin{bmatrix} 1 \\ 1 \\ -1 \\ 1 \end{bmatrix} \tag{3.49}$$

By applying equation (3.43), the real connectivity with actual fluid directions now become:

$$C^{real} = \begin{bmatrix} -1 & 0 & 0 & 0 \\ 1 & -1 & -1 & 0 \\ 0 & 1 & 1 & -1 \\ 0 & 0 & 0 & 1 \end{bmatrix} \tag{3.50}$$

Next the matrix representing the real flows into and out of nodes is calculated:

$$C^{real,in} = \begin{bmatrix} 0 & 0 & 0 & 0 \\ 1 & 0 & 0 & 0 \\ 0 & 1 & 1 & 0 \\ 0 & 0 & 0 & 1 \end{bmatrix} \tag{3.51}$$

$$C^{real,out} = \begin{bmatrix} 1 & 0 & 0 & 0 \\ 0 & 1 & 1 & 0 \\ 0 & 0 & 0 & 1 \\ 0 & 0 & 0 & 0 \end{bmatrix} \tag{3.52}$$

Finally the inlet enthalpy boundary condition is set. This boundary condition could of course change to any other node that can potentially become the inlet or source node as described above. The program therefore has to check which nodes are sources or sinks during each iteration and apply the boundary condition only to source nodes.

$$h_{0,\text{inletnodes}} = \begin{bmatrix} h_{0,\text{N1}} \\ 0 \\ 0 \\ 0 \end{bmatrix} \tag{3.53}$$

Thus the set of equations (3.46) becomes:

$$\begin{bmatrix} 1 & 0 & 0 & 0 \\ \dot{m}_1 & -\dot{m}_1 & 0 & 0 \\ 0 & \dot{m}_2+\dot{m}_3 & -\dot{m}_2-\dot{m}_3 & 0 \\ 0 & 0 & \dot{m}_4 & -\dot{m}_4 \end{bmatrix} \times \begin{bmatrix} h_{0,\text{N1}} \\ h_{0,\text{N2}} \\ h_{0,\text{N3}} \\ h_{0,\text{N4}} \end{bmatrix} + \begin{bmatrix} 0 \\ \dot{Q}_{E1}+W_{E1} \\ \dot{Q}_{E2}+W_{E2}+\dot{Q}_{E3}+W_{E3} \\ \dot{Q}_{E4}+W_{E4} \end{bmatrix} = \begin{bmatrix} h_{0,\text{N1}} \\ 0 \\ 0 \\ 0 \end{bmatrix} \tag{3.54}$$

Using this set of equations, $h_{0,\text{N}}$ can be solved simultaneously by using right-matrix division in Scilab. Once the nodal enthalpies are known, the fluid temperature can be calculated. This means that the density must be updated and that the mass flow rates calculated previously have changed. It is therefore necessary to perform another iteration of the pressure correction scheme.

3.4.4 Angular momentum equation

After the pressure distribution and thus the mass flow rates have been updated, the velocity of the fluid has changed and needs to be updated. The updated velocity values are required as inputs to the next iteration of the mass-momentum-energy calculation.

The implementation of the velocity calculation will also be explained by using the same example network in Figure 25. To calculate the velocity components in the axial and radial directions, continuity is applied in those directions, but to calculate the tangential component conservation of angular momentum must be applied.

In the network, nodes are again used to sum and balance angular momentum from connected elements while elements are used to describe a change in angular momentum caused by guide vanes or torque applied to the fluid. Thus it is assumed that no angular momentum change

occurs within a node. It is also assumed that the angular momentum at the inlet of an element is independent of the geometry of the element, but always the same as the angular momentum at the node upstream of the element. Equation (3.14) can be simplified for every node by separating the positive and negative parts of the surface integral to describe in and out flows. The equation for the steady state case then simplifies to:

$$\sum_{N} M_{o,\mathrm{N}} = \sum_{E}\left(\left(\overline{r}_E \times \overline{c}_E\right)\dot{m}_E\right)_{out} - \sum_{E}\left(\left(\overline{r}_E \times \overline{c}_E\right)\dot{m}_E\right)_{in} \tag{3.55}$$

Only moments about the z–axis are considered and so the cross-product is simplified:

$$\sum_{N} M_{z,\mathrm{N}} = \sum_{E}\left(\left(\omega_E r_E^2 + v_E r_E \sin\alpha_E \sin\beta_E\right)\dot{m}_E\right)_{out,\mathrm{N}} - \sum_{E}\left(\left(\omega_E r_E^2 + v_E r_E \sin\alpha_E \sin\beta_E\right)\dot{m}_E\right)_{in,N} \tag{3.56}$$

It is assumed that there is no change in angular momentum across the node, so the sum of moments are equal to zero. The specific angular momentum at a certain point in an element with number 'E' can be defined as:

$$L_{\mathrm{E}} = \omega r_E^2 + v_E r_E \sin\alpha_E \sin\beta_E \tag{3.57}$$

Equation (3.56) can be simplified for every node:

$$\sum_{E}\left(\dot{m}_E L_{\mathrm{out,E}}\right)_{in,N} - \sum_{E}\left(\dot{m}_E L_{\mathrm{in,E}}\right)_{out,N} = 0 \tag{3.58}$$

The node has only one outlet connected to one or several elements, so that the specific angular momentum, $L_{in,E}$, of all the flow elements leaving the node are the same and equal to the specific angular momentum at the node L_N. In this way the node is assumed to act as a mixing plane, thoroughly mixing different inlet flows into a uniform outlet flow.

$$\sum_{E}\left(\dot{m}_E L_{\mathrm{out,E}}\right)_{in,N} - L_{\mathrm{N}}\sum_{E}\left(\dot{m}_E\right)_{out,N} = 0 \tag{3.59}$$

Angular momentum flowing into the node is determined by the moment imparted to the fluid in the upstream elements. In the model, an assumption is made that flows exiting stator or rotor rows are defined by the geometrical outlet angle of the vanes or blades of those stages plus a slight deviation that may be caused by less than ideal flow conditions at the trailing edge of the blades (Ainley & Mathieson, 1951). This effect is also known as slippage. Therefore the angular momentum and velocities are calculated from the change in flow angles and radii and

not the change in geometrical angles of the blades from inlet to outlet. Thus all the $L_{out,E}$ terms from stator and rotor elements into downstream nodes can be calculated from the known geometry and flow parameters.

Flows exiting stationary elements that have no vanes or blades, for example, connecting pipes, leakage flows and spaces between rows, are assumed to have zero net change in specific angular momentum from the inlet to the outlet of the element, because there is no surface to realise an external moment around the z-axis and rotating friction in moving seals is neglected. For such an element the specific angular momentum at the inlet and outlet are the same:

$$\dot{m}_E L_{in,E} = \dot{m}_E L_{out,E} \tag{3.60}$$

where as shown above,

$$L_{in,E} = L_{out,N(upstream)} \tag{3.61}$$

It is therefore necessary to add an additional term to equation (3.59) to differentiate between the different ways that L is determined depending on the types of elements that flow into nodes:

$$\sum_{\text{E(}rotors\text{\&stators)}} \left(\dot{m}_E L_{out,E}\right)_{in,N} + \sum_{\text{E(gaps,seals,etc)}} \left(\dot{m}_E L_{out,N(upstream)}\right)_{in,N} = L_N \sum_E \left(\dot{m}_E\right)_{out} \tag{3.62}$$

L_N can be solved for in this equation, but it is first necessary to calculate the $L_{\text{out,E(rotors\&stators)}}$ that flow into the nodes. At the outlet of a stator or rotor element the orientation or normal vector of the area and the angles φ_{out} and ψ_{out} of the flow are known. Thus the normal velocity, v_n, through the outlet surface can be determined by applying continuity and then determine the magnitude of the flow vector with the geometry of the flow path, angles φ_{out} and ψ_{out}. These surfaces have been defined to not have a component in the θ-direction and so the normal vector lies in the rz-plane. Thus, the normal velocity through the surface is the projection of the component of relative velocity vector in rz-plane onto the unit normal vector of the outlet area. The component of the relative velocity vector in the rz-plane is defined by the angle, ψ_{out} and an angle $\beta_{rel,rz}$. The projected velocity component can be calculated by performing the dot-product:

$$\left\|\bar{v}_n\right\| = \left\|\bar{v}_{rz}\right\|\left(\sin\psi\cos\beta_{rel,rz}\sin\alpha'\cos\beta' + \sin\psi\sin\beta_{rel,rz}\sin\alpha'\sin\beta' + \cos\psi\cos\alpha'\right) \tag{3.63}$$

The accent denotes angles attributed to the area normal unit vector. The equation is rearranged to calculate the magnitude of the component of relative velocity vector in the rz-plane:

$$\left\|\bar{v}_{rz}\right\| = \frac{\left\|\bar{v}_{n}\right\|}{\left(\sin\psi\cos\beta_{rel,rz}\sin\alpha'\cos\beta' + \sin\psi\sin\beta_{rel,rz}\sin\alpha'\sin\beta' + \cos\psi\cos\alpha'\right)} \tag{3.64}$$

Next, the components of the relative velocity vector can be determined from the trigonometric relationships:

$$\begin{aligned} \left\|\bar{v}_{z}\right\| &= \left\|\bar{v}_{rz}\right\|\cos\psi \\ \left\|\bar{v}_{r}\right\| &= \left\|\bar{v}_{rz}\right\|\sin\psi \\ \left\|\bar{v}_{\theta}\right\| &= \left\|\bar{v}_{z}\right\|\tan\varphi \end{aligned} \tag{3.65}$$

The relative velocity vector for flows into nodes from stators and rotors is calculated from the vector components and the complete velocity triangle can be described.

Equation (3.62) is solved to determine the specific angular momentum at each node. This is also the specific angular momentum flowing out of the nodes and into elements and so the velocity vector at the inlet to each element will be solved once it is known. Finally the outlet velocity vectors for elements without vanes or blades are calculated by considering that there is no net change in specific angular momentum for these elements.

To calculate the relative velocity at the inlet of an element the definition of specific angular momentum given in equation (3.57) is used. The equation is rewritten for v_{θ}:

$$v_{\theta,in} = \frac{L_{\mathrm{N(upstream)}}}{r_{in}} - \omega r_{in} \tag{3.66}$$

When these equations are applied to the network in Figure 25 a set of equations is obtained that can be solved for L_N:

$$\sum_{E(gaps,seals,ect.)} \left(C_{NE}^{real,in}\dot{m}_E C_{NE}^{real,out\,\prime} - C_{NE}^{real,\mathrm{out}}\dot{m}_E\right)L_N + \sum_{E(stators\&rotors)} \left(C_{NE}^{real,in}\dot{m}_E L_{N(upstream)}\right) = L_{BC} \tag{3.67}$$

The equation is tested for the internal nodes and sinks. The assumption is made that elements 1 and 2 are elements of the type ‘seals or gaps’ and 3 and 4 are of the type ‘stators and rotors’. The pressure drop is assumed to be from node 1 to node 4. The real connectivity matrix is used.

Next the inlet specific angular momentum boundary condition at the nodes determined to be mass sources is set. This boundary condition could of course change to any other node that can potentially become the inlet or source node depending on the direction of flow calculated by the program. The program therefore has to check which nodes are sources or sinks during each iteration and apply the boundary condition only to source nodes.

$$L_{inletnodes} = \begin{bmatrix} L_{N1} \\ 0 \\ 0 \\ 0 \end{bmatrix} \tag{3.68}$$

Thus the set of equations (3.67) becomes:

$$\begin{bmatrix} 1 & 0 & 0 & 0 \\ \dot{m}_1 & -\dot{m}_2 - \dot{m}_3 & 0 & 0 \\ 0 & \dot{m}_2 & -\dot{m}_4 & 0 \\ 0 & 0 & 0 & -\dot{m}_4 \end{bmatrix} \times \begin{bmatrix} L_{N1} \\ L_{N2} \\ L_{N3} \\ L_{N4} \end{bmatrix} + \begin{bmatrix} 0 \\ 0 \\ \dot{m}_3 L_{out,E3} \\ \dot{m}_4 L_{out,E4} \end{bmatrix} = \begin{bmatrix} L_{N1} \\ 0 \\ 0 \\ 0 \end{bmatrix} \tag{3.69}$$

Where the N subscript refers to values out of nodes and the 'E' subscript refers to values out of elements. Using this equation, we can solve for L_N by using right-matrix division in Scilab.

3.4.5 Mass flow rate as a function of total pressure

In paragraph 3.4.2, it was shown how the mass flow rate in a flow element can be written as a function of total pressure at the inlet and the exhaust of the flow element. Since we can write $\dot{m} = f\left(p_{0,in}, p_{0,\text{out}}\right)$ for each element in the network it is possible to write the continuity equation for each node in the network in terms of total pressures. The result is a set of equations where only the total pressures at the nodes are unknown that can be solved simultaneously for all the total pressures in the network:

$$\Delta p_{0,L} = \dot{m}^2 \left[\begin{array}{l} Y_{loss,in} p_{in} \left(\dfrac{\dfrac{1}{\dot{m}^2} + \left(\dfrac{\gamma-1}{2}\right)\left(\dfrac{1}{\rho_{in}^2 A_{in}^2 (\hat{n}.\hat{o})^2 \gamma R T_{in}}\right)}{\left(1+\dfrac{\gamma-1}{2} M_{rel,in}^2\right)^{1-\frac{\gamma}{\gamma-1}}} - \dfrac{1}{\dot{m}^2} \right) + \\ Y_{loss,avg} p_{avg} \left(\dfrac{\dfrac{1}{\dot{m}^2} + \left(\dfrac{\gamma-1}{2}\right)\left(\dfrac{1}{\rho_{avg}^2 A_{avg}^2 (\hat{n}.\hat{o})^2 \gamma R T_{avg}}\right)}{\left(1+\dfrac{\gamma-1}{2} M_{\text{avg},rel}^2\right)^{1-\frac{\gamma}{\gamma-1}}} - \dfrac{1}{\dot{m}^2} \right) + \\ Y_{loss,\text{out}} p_{out} \left(\dfrac{\dfrac{1}{\dot{m}^2} + \left(\dfrac{\gamma-1}{2}\right)\left(\dfrac{1}{\rho_{out}^2 A_{out}^2 (\hat{n}.\hat{o})^2 \gamma R T}\right)}{\left(1+\dfrac{\gamma-1}{2} M_{rel,out}^2\right)^{1-\frac{\gamma}{\gamma-1}}} - \dfrac{1}{\dot{m}^2} \right) \end{array} \right] \quad (3.70)$$

The full development of this equation is provided in Appendix A.

The conservation of momentum equation can be rearranged to write for pressure losses:

$$\Delta p_{0,L} = -\frac{p_{avg}}{p_{0,avg}} \left(p_{0,\text{out}} - p_{0,in} \right) - \frac{1}{2} \rho_{avg} C_{avg}^2 \frac{1}{T_{0,avg}} \left(T_{0,\text{out}} - T_{0,in} \right) - \rho_{avg} g \left(z_{out} - z_{in} \right) + \rho_{avg} \omega X \quad (3.70)$$

substitute (3.70) into (3.70) and rearrange to obtain a function of the form $\dot{m} = f\left(p_{0,in}, p_{0,\text{out}}\right)$ that also conserves momentum :

$$\dot{m} = \frac{-\frac{p_{avg}}{p_{0,avg}}\left(p_{0,\text{out}} - p_{0,in}\right) - \frac{1}{2}\rho_{avg}C_{avg}^2\frac{1}{T_{0,avg}}\left(T_{0,\text{out}} - T_{0,in}\right) - \rho_{avg}g\left(z_{\text{out}} - z_{in}\right) + \rho_{avg}\omega X}{\left|\dot{m}\right|\left[\begin{array}{l} Y_{loss,in}p_{in}\left(\frac{\frac{1}{\dot{m}^2} + \left(\frac{\gamma-1}{2}\right)\left(\frac{1}{\rho_{in}^2 A_{in}^2(\hat{n}.\hat{o})^2\gamma RT_{in}}\right)}{\left(1+\frac{\gamma-1}{2}M_{rel,in}^2\right)^{1-\frac{\gamma}{\gamma-1}}} - \frac{1}{\dot{m}^2}\right) + \\ Y_{loss,avg}p_{avg}\left(\frac{\frac{1}{\dot{m}^2} + \left(\frac{\gamma-1}{2}\right)\left(\frac{v^2}{\dot{m}^2\gamma RT_{avg}}\right)}{\left(1+\frac{\gamma-1}{2}M_{rel,avg}^2\right)^{1-\frac{\gamma}{\gamma-1}}} - \frac{1}{\dot{m}^2}\right) + \\ Y_{loss,\text{out}}p_{\text{out}}\left(\frac{\frac{1}{\dot{m}^2} + \left(\frac{\gamma-1}{2}\right)\left(\frac{1}{\rho_{\text{out}}^2 A_{\text{out}}^2(\hat{n}.\hat{o})^2\gamma RT}\right)}{\left(1+\frac{\gamma-1}{2}M_{rel,out}^2\right)^{1-\frac{\gamma}{\gamma-1}}} - \frac{1}{\dot{m}^2}\right) \end{array}\right]} \tag{3.71}$$

The terms containing p_0 are separated from the rest of the terms which are calculated and updated after each iteration, and solved for.

$$\dot{m} = coeffs.\left(p_{0,out} - p_{0,in}\right) + consts \tag{3.71}$$

where:

$$coeffs = \frac{-\frac{p_{avg}}{p_{0,avg}}}{\left|\dot{m}\right|\left[\begin{array}{l} Y_{loss,in}p_{in}\left(\frac{\frac{1}{\dot{m}^2}+\left(\frac{\gamma-1}{2}\right)\left(\frac{1}{\rho_{in}^2A_{in}^2(\hat{n}.\hat{o})^2\gamma RT_{in}}\right)}{\left(1+\frac{\gamma-1}{2}M_{rel,in}^2\right)^{1-\frac{\gamma}{\gamma-1}}}-\frac{1}{\dot{m}^2}\right)+ \\ Y_{loss,avg}p_{avg}\left(\frac{\frac{1}{\dot{m}^2}+\left(\frac{\gamma-1}{2}\right)\left(\frac{v^2}{\dot{m}^2\gamma RT_{avg}}\right)}{\left(1+\frac{\gamma-1}{2}M_{rel,avg}^2\right)^{1-\frac{\gamma}{\gamma-1}}}-\frac{1}{\dot{m}^2}\right)+ \\ Y_{loss,\mathrm{out}}p_{out}\left(\frac{\frac{1}{\dot{m}^2}+\left(\frac{\gamma-1}{2}\right)\left(\frac{1}{\rho_{out}^2A_{out}^2(\hat{n}.\hat{o})^2\gamma RT}\right)}{\left(1+\frac{\gamma-1}{2}M_{rel,out}^2\right)^{1-\frac{\gamma}{\gamma-1}}}-\frac{1}{\dot{m}^2}\right) \end{array}\right]} \tag{3.71}$$

and

$$consts = \frac{-\frac{1}{2}\rho_{avg}C_{avg}^2\frac{1}{T_{0,avg}}\left(T_{0,\mathrm{out}}-T_{0,in}\right)-\rho_{avg}g\left(z_{out}-z_{in}\right)+\rho_{avg}\omega X}{\left|\dot{m}\right|\left[\begin{array}{l} Y_{loss,in}p_{in}\left(\frac{\frac{1}{\dot{m}^2}+\left(\frac{\gamma-1}{2}\right)\left(\frac{1}{\rho_{in}^2A_{in}^2(\hat{n}.\hat{o})^2\gamma RT_{in}}\right)}{\left(1+\frac{\gamma-1}{2}M_{rel,in}^2\right)^{1-\frac{\gamma}{\gamma-1}}}-\frac{1}{\dot{m}^2}\right)+ \\ Y_{loss,avg}p_{avg}\left(\frac{\frac{1}{\dot{m}^2}+\left(\frac{\gamma-1}{2}\right)\left(\frac{v^2}{\dot{m}^2\gamma RT_{avg}}\right)}{\left(1+\frac{\gamma-1}{2}M_{rel,avg}^2\right)^{1-\frac{\gamma}{\gamma-1}}}-\frac{1}{\dot{m}^2}\right)+ \\ Y_{loss,\mathrm{out}}p_{out}\left(\frac{\frac{1}{\dot{m}^2}+\left(\frac{\gamma-1}{2}\right)\left(\frac{1}{\rho_{out}^2A_{out}^2(\hat{n}.\hat{o})^2\gamma RT}\right)}{\left(1+\frac{\gamma-1}{2}M_{rel,out}^2\right)^{1-\frac{\gamma}{\gamma-1}}}-\frac{1}{\dot{m}^2}\right) \end{array}\right]} \tag{3.71}$$

As illustrated in paragraph 3.4.2 a set of these equations can be solved simultaneously for the p_0 values. Initial guess values are used to calculate *coeffs* and *consts* terms before the first iteration.

3.4.6 Convergence, relaxation and choking

During the solving process many parameters are updated. For example, the direction of the mass flows can change during the solution, thermodynamic properties change and calculated losses change effectively creating a dynamic network that needs to be solved. In order to assist the solution, relaxation of some of the parameters is required. During development of the program it was found that the best results can be obtained by relaxing the solution of the total pressures at the nodes and/or the mass flow rates of the elements. Therefore it is important that convergence of both these parameters must be reached before the solution can be considered complete.

The most complex model required in the present work consisted of 55 flow elements. The networks are easily solved on a personal computer in under one minute.

The model applies a compressible flow solution and therefore it is also necessary to account for choking of flow passages. During each iteration, the program checks the relative velocity Mach number of each flow element at the inlet, outlet and average values and limits it to a value of one. by adjusting the mass flow rate for that element. The pressure correction scheme will continue until convergence is achieved.

3.5 Compatibility of the model with a complete cycle

The network approach described above is a generic approach that is commonly used to model pipe flows and even more complex systems such as plant systems with pipes, valves, heaters, coolers and even elements that perform work on the fluid. The external boundaries of the turbine model are represented by two or more nodes where the boundary conditions are described. These nodes could be connected to additional elements to represent the inlet pipe of the turbine or the upstream valves. At the turbine outlet an element could be connected to represent a diffuser or a condenser and so on. The flow through the inlet pipes and valves could by this method be included in the complete turbine model and solved in one simultaneous solution. Following this philosophy it should be possible to model a complete steam or gas cycle where the turbine model forms an integral part and the entire cycle including the turbine can

be solved simultaneously. Thermofluid network models of the complete steam cycle for power plants exist, but usually utilise a simplified model of the turbine. Demonstrating this is beyond the scope of this project.

3.6 Summary of simplifying assumptions

Some simplifying assumptions have been made about the flows in the turbine in this chapter. These assumptions are made to allow the problem to be solved in a practical manner without affecting the results significantly.

It is assumed that there is no heat transfer between the turbine blades and the fluid. The required physics have been implemented in the program and verified, but not validated or applied to the test case.

It is assumed that the flows from multiple elements into a node are properly mixed when it leaves the node as single or multiple flows.

The cross sectional areas of all the element inlets and outlets are oriented perpendicular to axial direction.

The flow upstream of an element is not influenced by the element geometry. Only when the flow enters an element is it redirected.

Labyrinths and leakage flows are assumed to have no work, heat transfer or angular momentum change.

3.7 Chapter summary

Starting at the basic principles of a turbine and applying the fundamental equations for conservation to the turbine flow passages through the turbine, a methodology has been developed to solve the conservation equations as applied to a turbine consisting of a thermofluid network of stationary and rotating control volumes. The methodology was implemented in Scilab through a pressure correction scheme and an energy balance calculation and the equations closed by applying loss models to determine the pressure losses in each of the discrete turbine control volumes. In the next chapter the loss models will be discussed in detail.

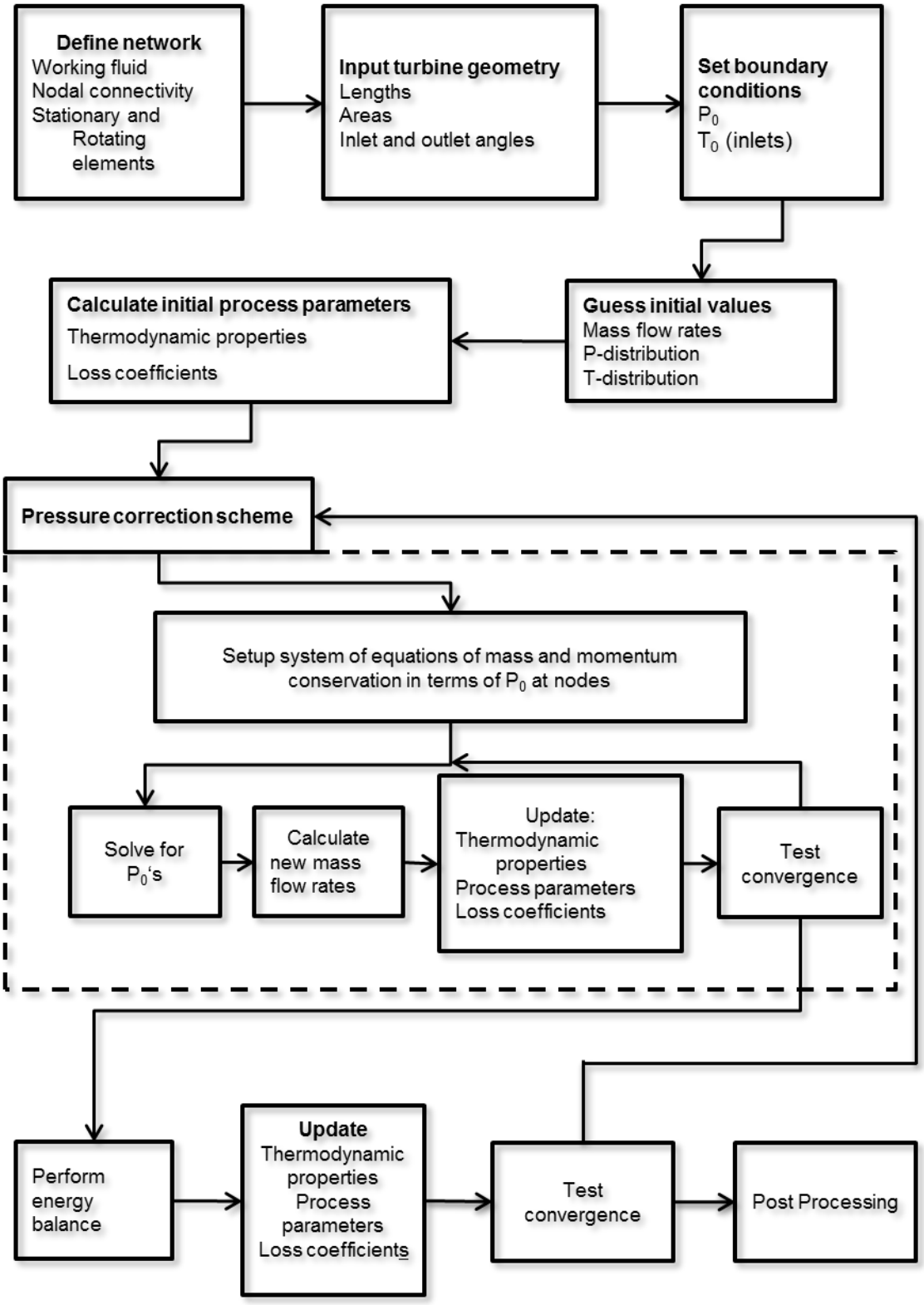

Figure 26. Flow diagram summarising the turbine model program.

Chapter 4. Loss models

4.1 Description of loss models

In section 3.2.5 the pressure loss coefficient, Y_{loss}, was defined in terms of total- and static pressures. In practice the pressure loss coefficient is obtained from wind tunnel measurements of 2D cascades and from data of real turbine stages. Empirical models are then fitted to this data so that they can be used to predict the pressure loss coefficient given certain variables. In the present method the pressure loss coefficient is calculated during each iteration of the pressure correction scheme based on the calculated fluid parameters and turbine geometry.

In general the loss models here use the definition of the blade angles given by Ainley and Mathieson (1951). In Figure 1 a comparison of the various definitions is provided. It is necessary to convert the calculated flow angles to the definition required by the loss model when calculating the loss coefficients.

4.1.1 Profile loss coefficient

The profile and trailing edge loss coefficients are given by Kacker and Okapuu (1982) based on a review of the loss system originally developed by Ainley and Mathieson (1951). These loss coefficients are based on a definition of pressure loss at the outlet of the flow element.

The basic profile loss is first calculated.

$$Y_{P,AMDC} = \left(Y_{P\left(\varphi_{blade,in}=0\right)} + \left| \frac{\varphi_{blade,in}}{\varphi_{flow,\mathrm{out}}} \right| \left(\frac{\varphi_{blade,in}}{\varphi_{flow,\mathrm{out}}} \right) \left(Y_{P\left(\varphi_{blade,in}=\varphi_{flow,\mathrm{out}}\right)} - Y_{P\left(\varphi_{blade,in}=0\right)} \right) \right) \left(\frac{t/c}{0.2} \right)^{\frac{\varphi_{blade,in}}{\varphi_{flow,\mathrm{out}}}} \tag{4.1}$$

A subsonic Mach number correction is calculated. The Mach number can affect the flow by causing shocks at the blade leading edge and by affecting the flow acceleration within the blade channel (Kacker & Okapuu, 1982).

$$Y_{SHOCK} = \left(\frac{r_{hub}}{r_{tip}} \right) 0.75 \left(M_{1,hub} - 0.4 \right)^{1.75} \left(\frac{p_{in}}{p_{out}} \right) \frac{1 - \left(1 + \frac{\gamma - 1}{2} M_{in}^2 \right)^{\frac{\gamma}{\gamma - 1}}}{1 - \left(1 + \frac{\gamma - 1}{2} M_{out}^2 \right)^{\frac{\gamma}{\gamma - 1}}} \tag{4.2}$$

In addition to the Mach number correction, the basic profile loss is also affected by Mach number effects. Flow separation and boundary layer thickness are suppressed at velocities close to sonic. A multiplier is calculated for these effects.

$$K_P = 1 - K_2\left(1 - K_1\right) \tag{4.3}$$

with K_1

$$\begin{aligned} K_1 &= 1 && \textit{for } M_{out} < 0.2 \\ &\textit{and} && \\ K_1 &= 1 - 1.25\left(M_{out} - 0.2\right) && \textit{for } M_{out} > 0.2 \end{aligned} \tag{4.4}$$

and

$$K_2 = \left(\frac{M_{in}}{M_{out}}\right)^2 \tag{4.5}$$

The basic profile loss coefficient is now augmented by the additional multipliers and shock loss.

$$Y_P = 0.914\left(\frac{2}{3}Y_{P,AMDC}K_P + Y_{SHOCK}\right) \tag{4.6}$$

For a Reynolds number based on true chord deviating from $2\text{x}10^5$ an additional multiplier is applied to Y_P.

$$\begin{aligned} f_{(\mathrm{Re})} &= \left(\frac{\mathrm{Re}}{2\times10^5}\right)^{-0.4} && \textit{for } \mathrm{Re} \le 2\times10^5 \\ &= 1 && \textit{for } 2\times10^5 < \mathrm{Re} < 10^6 \\ &= \left(\frac{\mathrm{Re}}{10^6}\right)^{-0.2} && \textit{for } \mathrm{Re} > 10^6 \end{aligned} \tag{4.7}$$

4.1.2 Trailing edge loss coefficient

The trailing edge loss given by Kacker and Okapuu (1982) is applied. The loss is based on the physical blockage effect by the trailing edge in terms of the ratio of trailing edge thickness to throat opening of the cascade. The trailing edge energy coefficient is read off a diagram below and interpolated according to the given equation. This loss coefficient is based on a definition

of pressure loss at the outlet of the flow element. The losses are given in a graph of the trailing edge energy coefficient. The data in these graphs were fit to functions in order to implement them in the program.

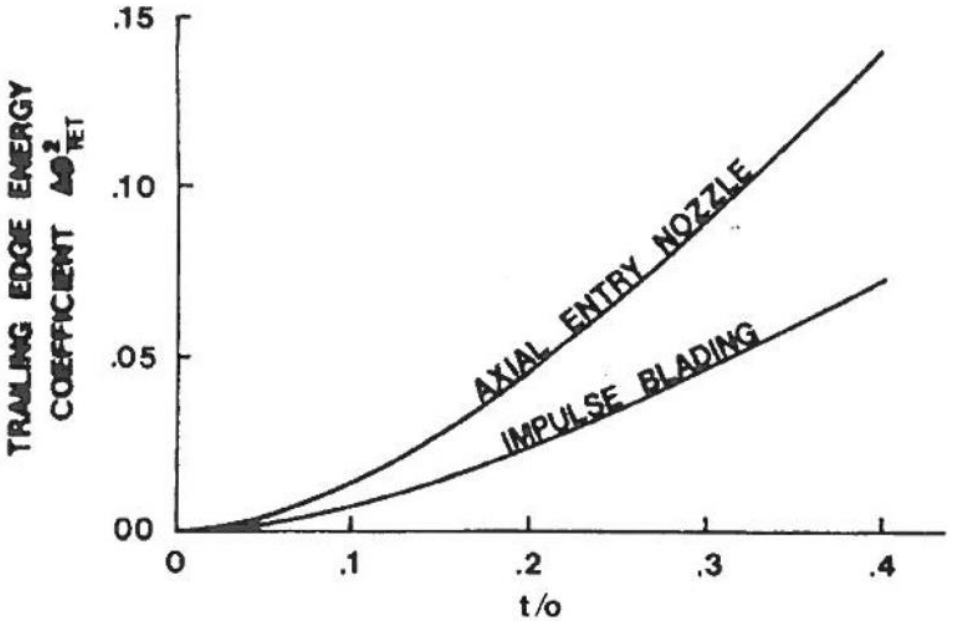

Figure 27. Trailing edge energy coefficient (Kacker & Okapuu, 1982)

$$\Delta\phi^2_{TET} = \Delta\phi^2_{TET(\varphi_{blade,in})} + \left|\frac{\varphi_{blade,in}}{\varphi_{flow,\text{out}}}\right|\left(\frac{\varphi_{blade,in}}{\varphi_{flow,\text{out}}}\right)\left(\Delta\phi^2_{TET(\varphi_{blade,\text{in}}=\varphi_{flow,\text{out}})} - \Delta\phi^2_{TET(\varphi_{blade,in}=0)}\right) \tag{4.8}$$

The energy coefficient is converted to a pressure loss coefficient by equation (4.9) which is also given by Kacker and Okapuu (1982).

$$Y_{TET} = \frac{\left[1-\frac{\gamma-1}{2}M^2_{out}\left(\frac{1}{1-\Delta\phi^2_{TET}}-1\right)\right]^{\frac{-\gamma}{\gamma-1}}-1}{1-\left(1-\frac{\gamma-1}{2}M^2_{out}\right)^{\frac{-\gamma}{\gamma-1}}} \tag{4.9}$$

4.1.3 Secondary loss coefficient

In Benner, et al., (2006) an improved method of calculating the secondary loss is proposed. Firstly, the penetration depth of the blade passage area affected by the secondary flow phenomena is calculated. The secondary loss is applied proportionally to the area affected by the secondary loss and the profile loss calculated above is applied proportionally to the remaining area of the flow passage that is unaffected by the secondary flow. A new secondary loss correlation is then calculated (Benner, et al., 2006).

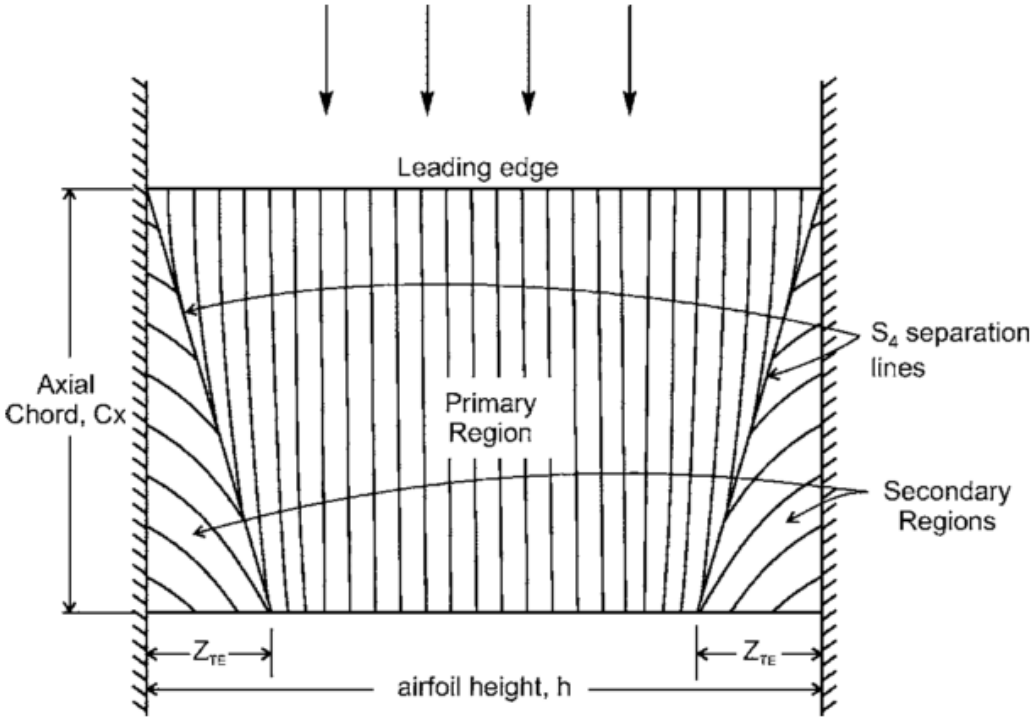

Figure 28. A diagram illustrating the two regions of the passage flow (Benner, et al., 2006).

The non-dimensional penetration depth correlation is given by:

$$\frac{Z_{TE}}{h} = \frac{0.1\left(F_t\right)^{0.79}}{\sqrt{CR}\left(\frac{h}{C}\right)^{0.55}} + 32.70\left(\frac{\delta^*}{h}\right)^2 \tag{4.10}$$

CR Is the convergence ratio, indicator of flow acceleration:

$$CR = \frac{\cos\varphi_{in}}{\cos\varphi_{out}} \tag{4.11}$$

F_t the tangential loading coefficient which represents the airfoil loading:

$$F_t = 2\left(\frac{s}{c_z}\right)\cos^2\varphi_{avg}\left(\tan\varphi_1 - \tan\varphi_2\right) \tag{4.12}$$

$\frac{h}{C}$ the airfoil aspect ratio.

$\frac{\delta^*}{h}$ non-dimensional inlet boundary layer displacement thickness. This parameter represents the ratio of mass flow in the endwall region to the passage mass flow rate. In the present work the value is estimated from data provided by Benner, et al (2006) for several turbines.

Finally two correlations for different aspect ratio blades are given for the secondary loss (Benner, et al., 2006):

$$Y_{secondary} = \frac{0.038 + 0.41\tanh\left(\frac{1.2\delta^*}{h}\right)}{\sqrt{\cos\gamma}\,(CR)\left(\frac{h}{C}\right)\left(\frac{C\cos\varphi_{out}}{C_x}\right)^{0.55}} \; for \frac{h}{C} \le 0.2 \tag{4.13}$$

and

$$Y_{secondary} = \frac{0.052 + 0.56\tanh\left(\frac{1.2\delta^*}{h}\right)}{\sqrt{\cos\gamma}\,(CR)\left(\frac{h}{C}\right)^{0.55}\left(\frac{C\cos\varphi_{out}}{C_x}\right)^{0.55}} \; for \frac{h}{C} > 0.2 \tag{4.14}$$

4.1.4 Labyrinth leakage loss

To model the leakage through the rotor shaft seals, the Saint Venant Wantzel model for a labyrinth seal is applied (Axel, 2003).

$$\dot{m} = C_{ke}C_d A_g \sqrt{\frac{2\gamma}{\gamma - 1}\frac{p_i^2}{RT_0}\left(\left(\frac{p_e}{p_i}\right)^{\frac{2}{\gamma}} - \left(\frac{p_e}{p_i}\right)^{\frac{\gamma+1}{\gamma}}\right)} \tag{4.15}$$

This model assumes that $\Delta p_0 = \Delta p_{0,loss}$ for a seal, because no work is done and no heat is transferred. Therefore the effect of rotational friction within the seal is not incorporated in the model. In the solver, the angular momentum is conserved between the inlet and the outlet of a labyrinth seal by assuming that there is no change in angular momentum. The equation is rewritten for a case with multiple sealing strips. The equation must also be written in the form of a pressure loss coefficient so that it can be implemented in the model. The derivation is provided in Appendix B. This loss coefficient is based on a definition of pressure loss at the outlet of the flow element.

$$Y_{seal} = \frac{\dot{m}^2}{\left(C_{ke} C_d A_g\right)^2 \frac{\left(p_{in} + p_{out}\right)\left(p_{0,\text{out}} - p_{out}\right)}{RT_0\left(z - \frac{2}{\gamma}\ln\left(\frac{p_{out}}{p_{in}}\right)\right)}} \tag{4.16}$$

with z number of seal strips, the discharge coefficient, C_d, and the kinetic carry-over coefficient, C_{ke}, given by Joubert (2003):

$$C_d = \frac{\pi}{\pi - 7\left(\frac{P_i}{P_e}\right)^{\frac{\gamma-1}{\gamma}} + \left(\frac{P_i}{P_e}\right)^{\frac{2\gamma-2}{\gamma}} + 8} \tag{4.17}$$

$$C_{ke} = \frac{1}{\sqrt{1 - \frac{8.52}{\frac{S-L}{cl} + 7.23}}} \tag{4.18}$$

4.1.5 Auxiliary loss

The losses associated with the geometry of the turbine casing and with the geometry of the rotor seal inlet and outlet areas are applied to a flow element placed in the gap between blade rows. The losses are made up of friction losses on the turbine hub and casing and the flow disturbance caused by the cavity in the hub that houses the labyrinth seal. The cavity loss coefficient is based on a definition of pressure loss at the inlet of the flow element, while friction losses are defined by the average values through the element.

The Darcy friction factor is calculated directly by using the Swamee-Jain equation.

$$f = 0.25\left(\log_{10}\left(\frac{\varepsilon}{3.7D} + \frac{5.74}{\mathrm{Re}^{0.9}}\right)\right)^{-2} \tag{4.19}$$

The friction loss coefficient is then calculated by using the hydraulic diameter of the flow element and the length of the flow path.

The cavity loss is given by Craig and Cox (1970). The data in Figure 29 were fit to functions in order to implement them in the program.

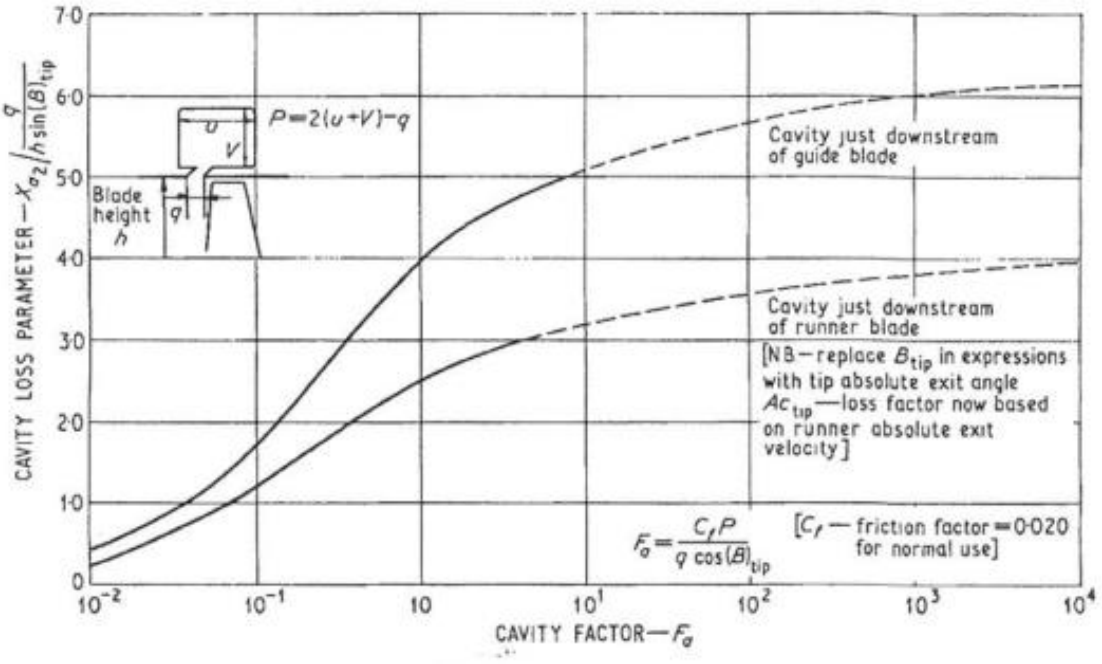

Figure 29. Cavity loss (Craig & Cox, 1970).

4.1.6 Chapter summary

In this chapter an overview of the loss models implemented in the Scilab program and the equations required to calculate them has been given. The next chapter will deal with verification of the model using a commercial thermofluid network software package and validation with a test case of a real turbine.

Chapter 5. Verification and validation

5.1 Model verification

In order to verify that the mathematics and physics have been correctly implemented and that program code is correct, verification tests were performed on the program.

5.1.1 Pressure correction scheme verification

The pressure correction scheme was tested to verify that pressure distributions and fluid parameters in the network are correctly calculated. This was done by comparing the calculated results for a few representative networks with the results obtained for the same networks by a commercial thermofluid network solver. The commercial software package, Flownex, was selected for this purpose because it has been validated extensively by its developers. Through this exercise the programming methodology and application of physics and mathematics were verified to be correct.

The first verification example is a network of three elements in series. The network has four nodes. A pressure drop is applied to the network with air as the working fluid. The same network was generated in Flownex using 'rotating channel' elements. For this exercise it is not necessary to give the channels a rotational speed. Figure 30 shows the network constructed in Flownex.

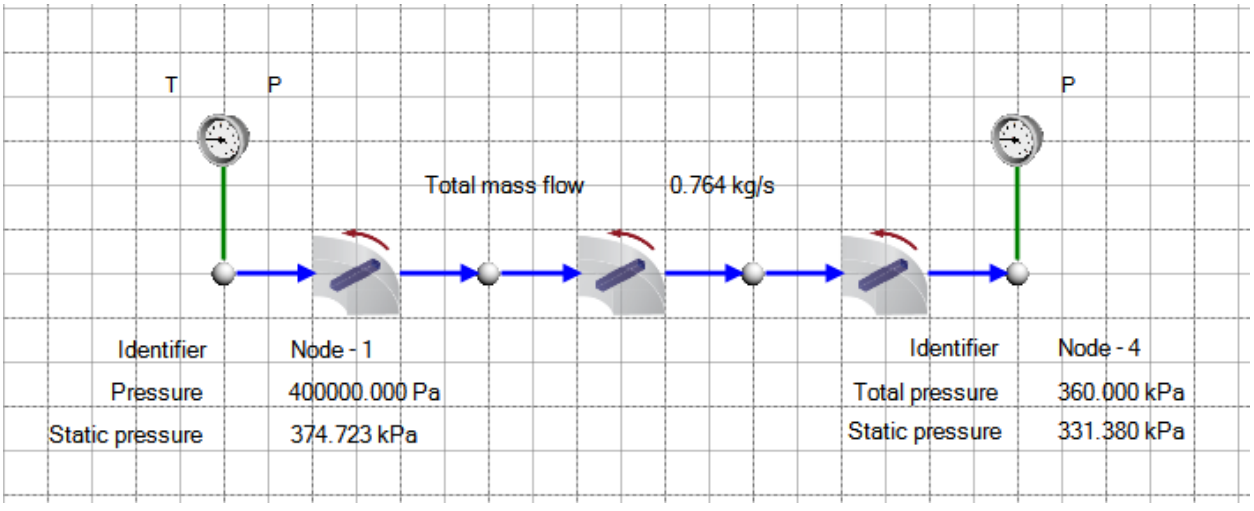

Figure 30. The Flownex network of three elements in series.

The mass flow rate for this network calculated by the program is 0.767kg/s. This compares very well with the mass rate flow of 0.764kg/s calculated by Flownex. In Table 3 the total pressures, static pressures and temperatures calculated by the program and Flownex are compared. The values compare well.

Table 3. A comparison between pressure distributions calculated by the program and by Flownex.

Node	**p_0 Flownex (kPa)**	**p_0 Present model (kPa)**	**%diff**	**p Flownex**	**p Present model (kPa)**	**%diff (kPa)**	**T_0 Flownex (^oC)**	**T_0 Present model (^oC)**	**%diff**
1	400	400	-	374.723	374.383	-9.073 $x10^{-2}$	433.150	433.15	-
2	387.252	387.250	-5.164 $x10^{-4}$	361.006	360.999	-1.939 $x10^{-3}$	433.139	433.15	2.539 $x10^{-3}$
3	373.947	373.950	8.022 $x10^{-4}$	346.599	346.589	-2.885 $x10^{-3}$	433.127	433.15	5.310 $x10^{-3}$
4	360	360	-	331.380	331.360	-6.035 $x10^{-3}$	433.115	433.15	8.081 $x10^{-3}$

The second verification example is a network of four elements arranged in two parallel pairs. The network has three nodes as illustrated in Figure 31. The two elements in the first pair have the same pressure loss coefficient applied to them while the elements in the second pair have different pressure loss coefficients. The program should be able to accurately calculate the pressures at the nodes as well as the pressure drops and mass flow rates through the different elements. In Table 4 the flow rates calculated for each element is compared with the flow rate calculated by Flownex. A maximum deviation of 1.4% is observed in element 3. The total flow rate through the network is calculated to within 0.02% of the result obtained by Flownex. In Table 5 the total and static pressures are compared. The static pressure is calculated to within 0.5% of the results obtained by Flownex.

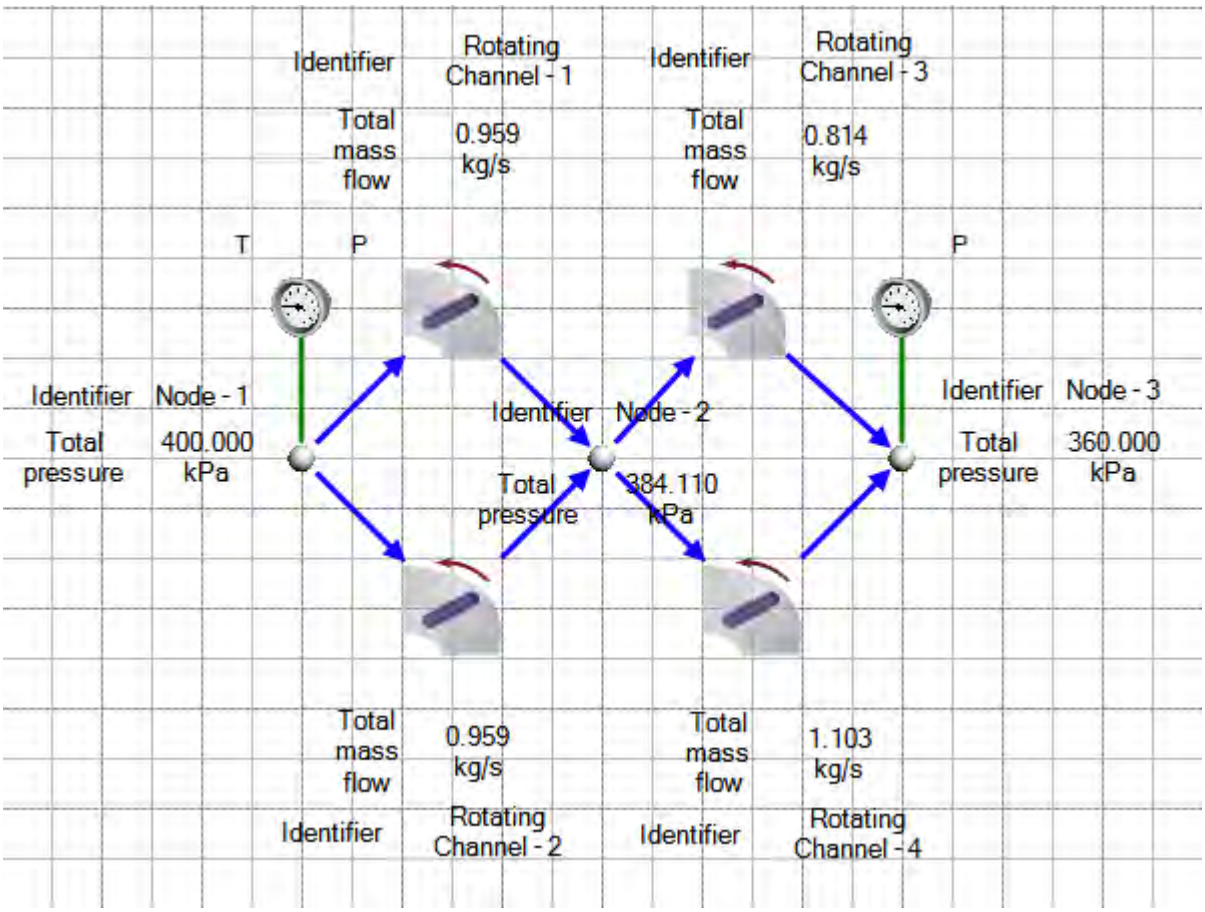

Figure 31. The Flownex network of four elements arranged in two pairs.

Table 4. A comparison between mass flow rates calculated by the program and by Flownex.

Element	**Mass flow rate Flownex**	**Mass flow rate Present model**	**%diff**
1	0.959	0.959	-1.721×10^{-2}
2	0.959	0.959	-1.721×10^{-2}
3	0.815	0.803	-1.428
4	1.103	1.114	1.024

Table 5. A comparison between pressure distributions calculated by the program and by Flownex.

Node	p_0 Flownex (kPa)	p_0 Present model (kPa)	%diff	p Flownex	p Present model (kPa)	%diff (kPa)	T_0 Flownex (^oC)	T_0 Present model (^oC)	%diff
1	400	400	0	368.924	367.282	-0.445	333.150	333.150	0
2	384.110	384.007	-2.681 $x10^{-2}$	350.433	351.264	0.237	333.121	333.150	0.853 $x10^{-2}$
3	360	360	0	322.207	321.656	-0.171	333.079	333.150	2.141 $x10^{-2}$

5.1.2 Angular momentum verification

The velocity vectors are calculated during each iteration of the pressure correction scheme and used as inputs for the next iteration. The calculation of both momentum- and energy conservation requires that the velocities into and out of each element and between elements must be calculated correctly and include summation of momentum from different elements across mixing planes. The velocity calculation was verified for a broad range of cases in order to confirm that the program can deal with all of the aspects of modelling turbine stage velocities including the radial component of the expanding flow as well as the effect that changes in the radial position has on the velocities derived from angular momentum. A quantitative assessment of the results was performed, but for the sake of brevity only the resulting diagrams are presented for the various cases.

In the present case, the turbine modelled, has a constant root diameter which implies an enlarging radial diameter and so the flow is not purely axial-tangential, but 3D. In other words, calculation of the vectors should be possible in any one of the 8 octants of 3D space and the trigonometric relationships must be reflected correctly.

5.1.2.1 Axial flow elements without blades or vanes

In this example the calculation was set up to represent two subsequent stages of purely axial flow elements without blades or vanes. The areas lie in the $r\theta$-plane and are constant. An angular momentum was specified at the inlet boundary and as expected the angular

momentum is conserved as it flows through the elements and through the areas. This is evident in Figure 32 because the tangential component of velocity can be seen to remain constant. The radial component of velocity is zero. The different colours of the vectors are used to illustrate various vectors according to the legend in Table 6.

Table 6. Legend of colours of calculated vectors.

Colour	Type
Yellow	Area normal unit vector.
Green	Velocity component perpendicular to the cross sectional area.
Blue	Relative velocity.
Red	Absolute velocity.
Solid line	Outlet velocity vector.
Dashed line	Inlet velocity vector.

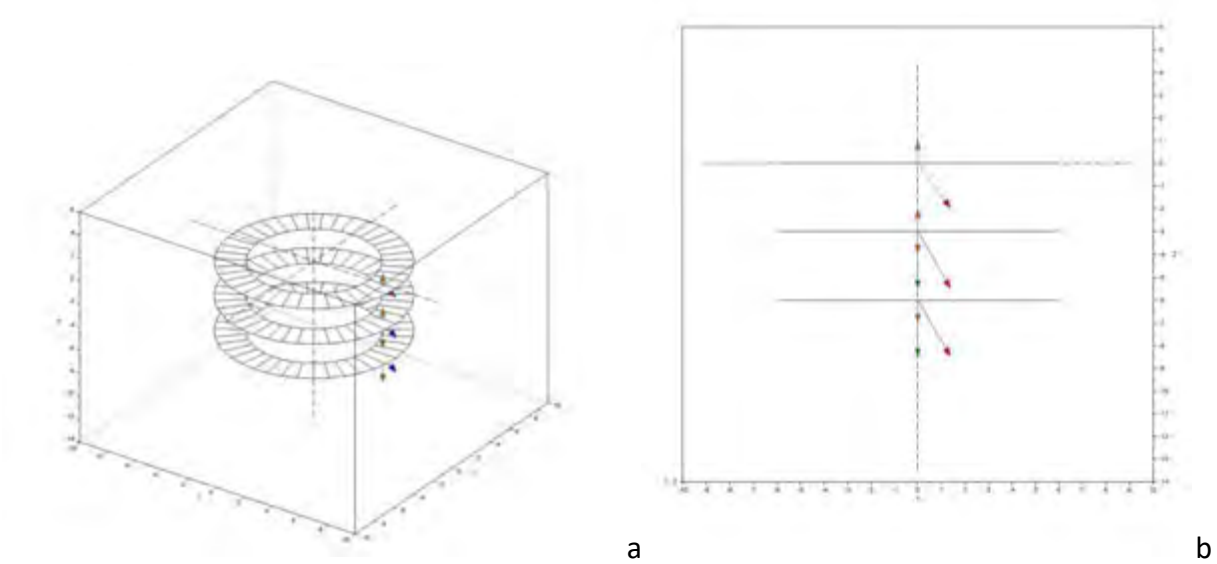

Figure 32. Isometric view a. and front view b. of verification test case axial flow elements without blades or vanes. See Appendix C for full size images.

5.1.2.2 Axial flow turbine with blades or vanes

In this test the calculation was setup to represent two subsequent stages of axial flow elements. The first element is a stationary set of vanes and the second a rotating set of blades. The areas lie in the $r\theta$-plane and are constant. Zero angular momentum was specified at the inlet boundary. Figure 33 shows that the angular momentum is changed as it flows through the stationary element and again as it flows through the rotating element. The relative and absolute velocities are calculated correctly for the rotating element.

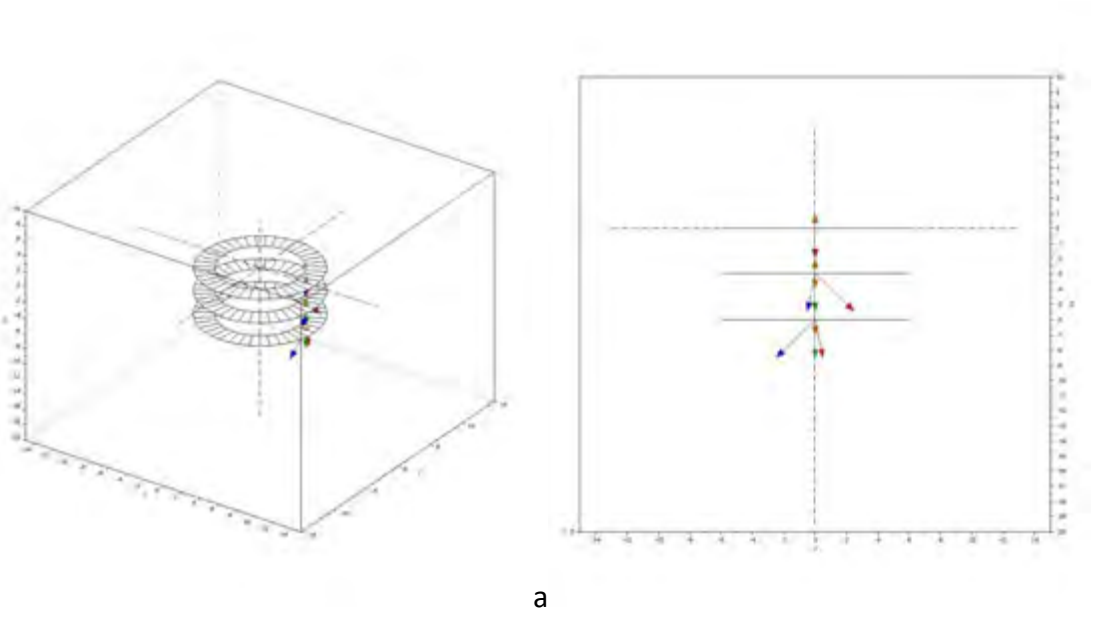

a b

Figure 33 . Isometric view a. and front view b. of verification test case axial flow turbine with blades or vanes. See Appendix C for full size images.

5.1.2.3 Radial flow elements without blades or vanes

In this test the calculation was setup to represent two subsequent stages of radial flow elements without blades or vanes. The areas are constant and this can be seen by the reduction in width of the areas as the radial distance becomes larger. An angular momentum was specified at the inlet boundary. Figure 34 shows that the tangential component of velocity becomes smaller as the flow with constant angular momentum moves outwards. This is expected for an increasing radial position.

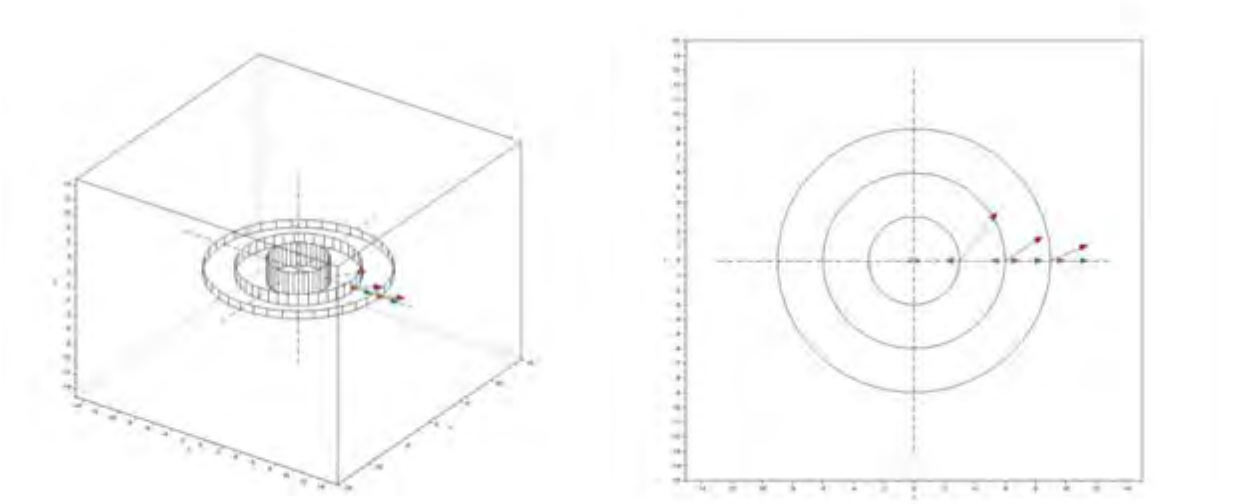

a b

Figure 34. Isometric view a. and front view b. of verification test case radial flow elements without guides or vanes. See Appendix C for full size images.

5.1.2.4 Combined axial and radial flow without blades or vanes

In this test the calculation was set up to represent two subsequent stages of combined axial and radial flow elements without blades or vanes. The areas are constant and are oriented at an angle to the z-axis. The purpose of this exercise was to confirm that the velocity vectors are calculated correctly for this type of orientation of the areas. An angular momentum was specified at the inlet boundary. Figure 40 shows that the flow is diverted from the axial direction into the radial direction and that the tangential component of velocity is decreased as the flow moves outward to a position at a larger radius.

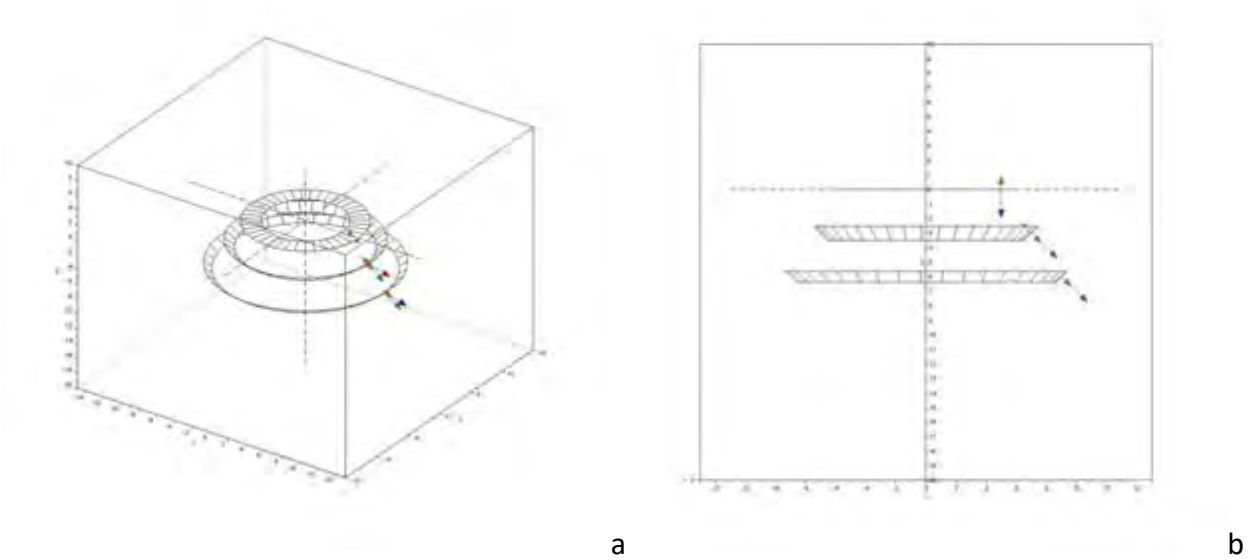

a b

Figure 35. Isometric view a. and front view b. of verification test case combined axial and radial flow. See Appendix C for full size images.

5.1.2.5 Axial areas with radial increase in diameter with blades or vanes

In this test the calculation was set up to represent two subsequent stages of combined axial and radial flow elements with blades and vanes. The first element is a stationary set of vanes and the second a rotating set of blades. The areas are constant and lie in the $r\theta$-plane. The purpose of this exercise was to confirm that the velocity vectors are calculated correctly when the flow has a radial component and the flow area is axially oriented. Figure 36 shows that the velocity vectors are correctly projected onto the normal area vectors from both the radial and tangential directions.

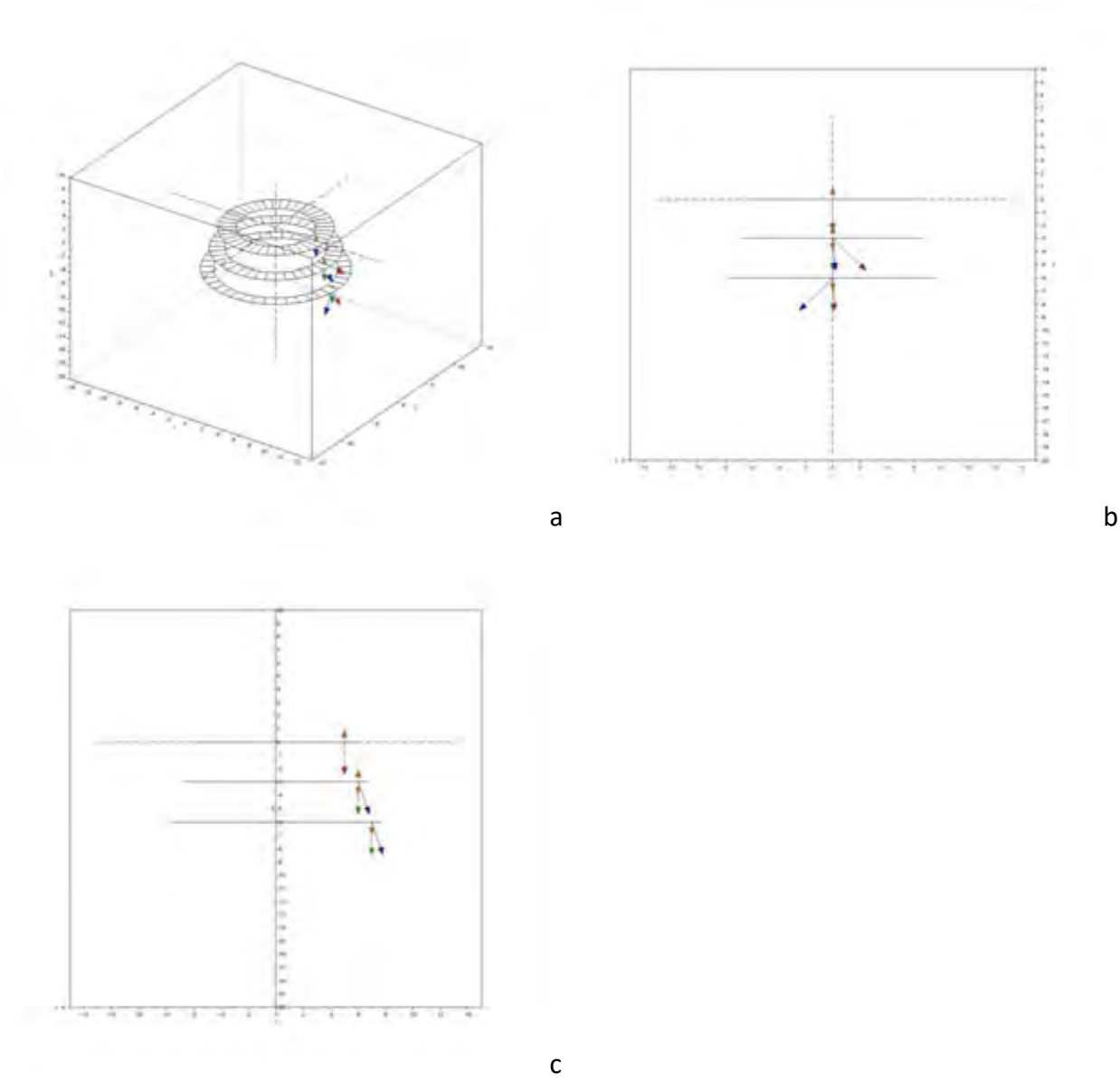

Figure 36. Isometric view a. and front view b. and side view c. of verification test case axial areas with radial increase in diameter. See Appendix C for full size images.

5.2 Validation test case

One of the goals of this project is to illustrate that the method developed is usable in practical applications, such as industrial turbines. In order to achieve this a practical test case was used to validate the method. By doing this various practical applications could be explored and evaluated, but most importantly the method could be validated. The accuracy of the model depends on the mathematical models used to describe the physical reality. Before the model

can be applied with confidence it must therefore be validated against physical measurements (Fottner, 1990).

5.2.1 Test cases considered

Some of the options that could be used to test or validate a model include analytical cases, laboratory setups and turbines in industrial settings. Theoretical cases include calculated examples from texts and comparisons with published results from other validated models. The risk with using this type of data for validation is that the valid range of assumptions and limitations of the data may not correspond with the model being tested.

Ideally, measured data from a turbine setup in a laboratory or measurement data from an industrial machine should be used. In both cases it is important to consider whether the test case represents the intended application of the model that is being validated. The quality of the measurements is also very important. Laboratory cases are often simplified turbines designed with the intention to limit variables that can influence test results, rather than to represent a broader range of application. Laboratory test rigs range from simple stationary blade rows or 2D cascades in a wind tunnel, to more complex turbines with single or multiple working stator and rotor stages. Measurements taken in laboratory test rigs are taken in a controlled environment and should therefore be of a good quality. Conversely, industrial turbines are usually complex machines that introduce many variables into the test results due to the uncontrolled nature of the industrial environment. Industrial machines may be very well equipped for monitoring the machine's health on an ongoing basis, but because the intention is not laboratory quality results, the industrial measurements are not as well set up as laboratory test rigs.

In all the options mentioned, access to such quality data is limited. Published texts rarely publish complete sets of inputs and outputs of models that would be required to validate a newly developed model (Fottner, 1990). Researchers most often only publish the results that are relevant to the topic of the specific research. Construction of an experimental test rig would entail an immense effort and financial commitment even before it could be employed and as such was not a feasible avenue.

Access to industrial test and operational measurement data could be acquired through a local utility company. The utility company also showed a lot of interest in participating in research. The company would even consider modifying their plant with additional measurement points

and high fidelity measurement equipment, but unfortunately no scheduled outages overlapped with the time window of this work.

Finally, the only viable source of validation data that could be obtained in a practical manner proved to be the report: Test Cases for Computation of Internal Flows in Aero Engine Components (Fottner, 1990). This is a report initiated and compiled by a panel of the Advisory Group for Aerospace Research and Development (AGARD) in 1990. The report aims to compile a substantive resource of validation cases for axial compressors and axial turbines.

5.2.2 Test case selected

The AGARD report contains a library of test data for analytical cases, stationary cascades and single and multiple stage working compressors and turbines. The purpose of the report is to provide test cases that address a range of different types of models and so the majority of them were not useful to the present study. Only one of the test cases represents the characteristics of a complete working industrial turbine. This is Test Case E/TU-4, which is a turbine rig with four working stator-rotor stages. the AGARD panel recommends that Test Case E/TU-4 is particularly suitable to axisymmetric through-flow calculations (Fottner, 1990).

5.2.3 Description of the test rig setup

Test Case E/TU-4 is a four stage turbine with an axially split casing. The turbine rotor is supported by two bearings mounted in the turbine casing at the turbine inlet and exhaust. The flow channel is formed by exchangeable axially split sections that are inserted into the outer casing and also serve as carriers for the stator blades. The rotor is equipped with continuous axial entry fir tree grooves that allow various blade sets to be installed. The hub has a constant diameter, but the annulus diameter increases towards the exhaust.

The turbine is driven by three screw compressors in parallel to form an open loop configuration. The compressors are capable of supplying $11 m^3/s$ of air at a maximum of 4 bar. The turbine is coupled to a direct current dynamometer which also allows the rotational speed to be modulated through voltage control.

The mass flow rate is measured by a venturi tube in the centre of the turbine inlet pipe, upstream of the turbine. The turbine speed is measured with an impulse counter and the torque by means of a torsion rod between the turbine shaft and the dynamometer.

Thermodynamic parameters of the air entering and leaving the turbine are measured with probes at these points.

Five measurement stations are located within the turbine where a pneumatic five hole probe is traversed in the radial direction to measure flow velocity, direction and temperature. The measurement stations are located 31mm upstream of the stator centrelines.

The turbine is designed by utilising the same blades for every stage. The blades are cropped at the appropriate lengths and become progressively longer towards the exhaust. The blade length varies from 64mm to 89 mm. The blading is of the free vortex type with 50 percent reaction at the mid-section of the final stage. The turbine geometry is provided as a set of coordinates describing the profiles at a few radial stations.

The stators are equipped with labyrinth seals against the rotor shaft whilst the blade tips have no seals. The clearances are given as an estimate of 0.4mm for the labyrinth sealing strips and blade tip gaps. Figure 37 shows a cross section of the CAD model of the turbine test case.

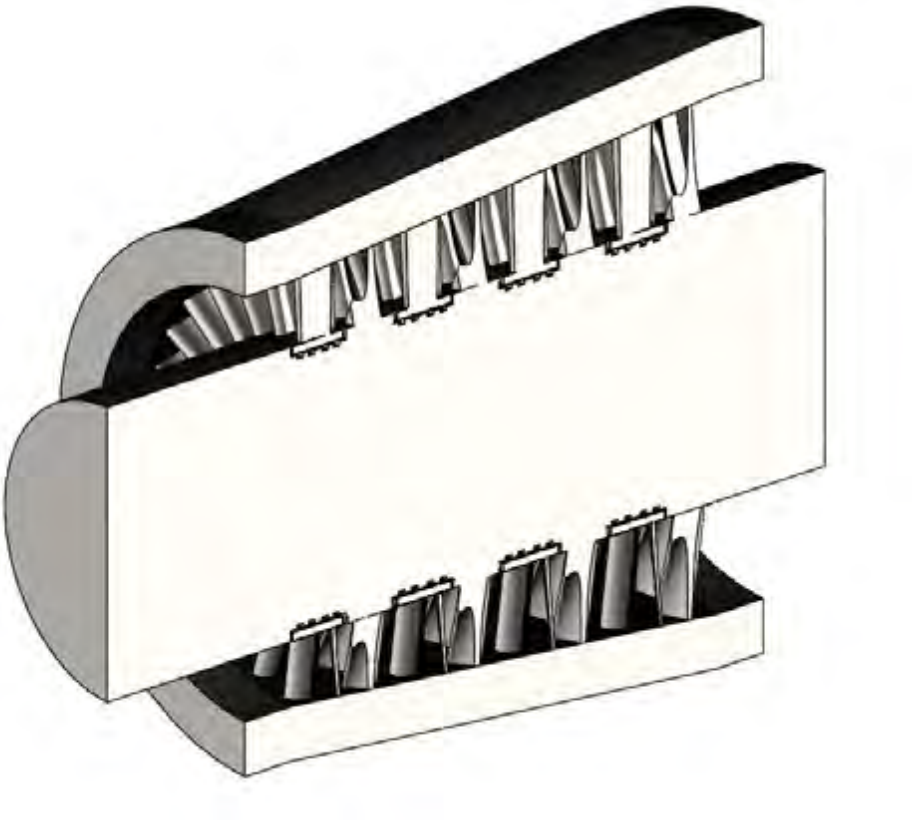

Figure 37. Turbine cross section. A detail drawing is provided in Appendix C.

Test data is provided for seven test cases with varying mass flow rates and rotational speeds given in Table 7.

Table 7. Description of the seven test cases published in AGARD.

Relative speed	**Relative mass flow rate m/m_0**					
n/n_0=1	1	0.83	-	0.59	0.53	-
n/n_0=0.75	-	-	0.71	-	0.50	0.41

5.2.4 Processing the AGARD data

The measured data is supplied in tables of the total pressure, static pressure, total temperature, velocity and direction angles of the velocity vector for each radial position of the traverse. In order to use and compare the data with calculated values from the model it was therefore necessary to calculate the mass averaged values. This was achieved by discretising the flow area into discrete annular areas with a measured point that corresponds to the radial centre distance of each of these areas. The measured pressure and temperature values were used to calculate the density and the flow angles were used to calculate the axial component of the flow which represents the mass flow direction through the machine. The first and last measurements of the traverse were located a small distance from the boundary wall. In order to obtain accurate results it was necessary to make the assumption of a zero velocity at the boundary wall and insert a velocity profile between the wall and the first measured point.

5.2.5 Obtaining geometric inputs

The blade profile data is given in tabular form at a few discrete radial stations for each blade. The rotor blade has a high degree of twist and a variation in thickness from root to tip. In order to discretise the flow, profile data is required at points that correspond to the mid-point of the discretised elements. The radial positions where the profile data is given do not necessarily correspond with the envisaged discretisation schemes. For example, for the most simple discretisation scheme of one element along the blade length the profile data would be required at the blade mid-point. However, none of the given profiles correspond with this point.

Given this, a methodology had to be developed to use the limited discrete data points provided to obtain a representative continuous description of the blade geometry for all the blades. The

development of this methodology and the associated generation of high quality geometric data required substantial effort but were unavoidable. However, having done this, this data is now also available for future studies on this topic.

In order to obtain the detailed geometry, it was necessary to interpolate between the given data points to obtain representative blade information at the points represented by the various discretisation schemes. Figure 38 and Figure 39 illustrate the profile data that was generated from the discrete data points for the nozzle blade and the rotor blade. Figure 40 shows the final generated CAD model of the rotor blade.

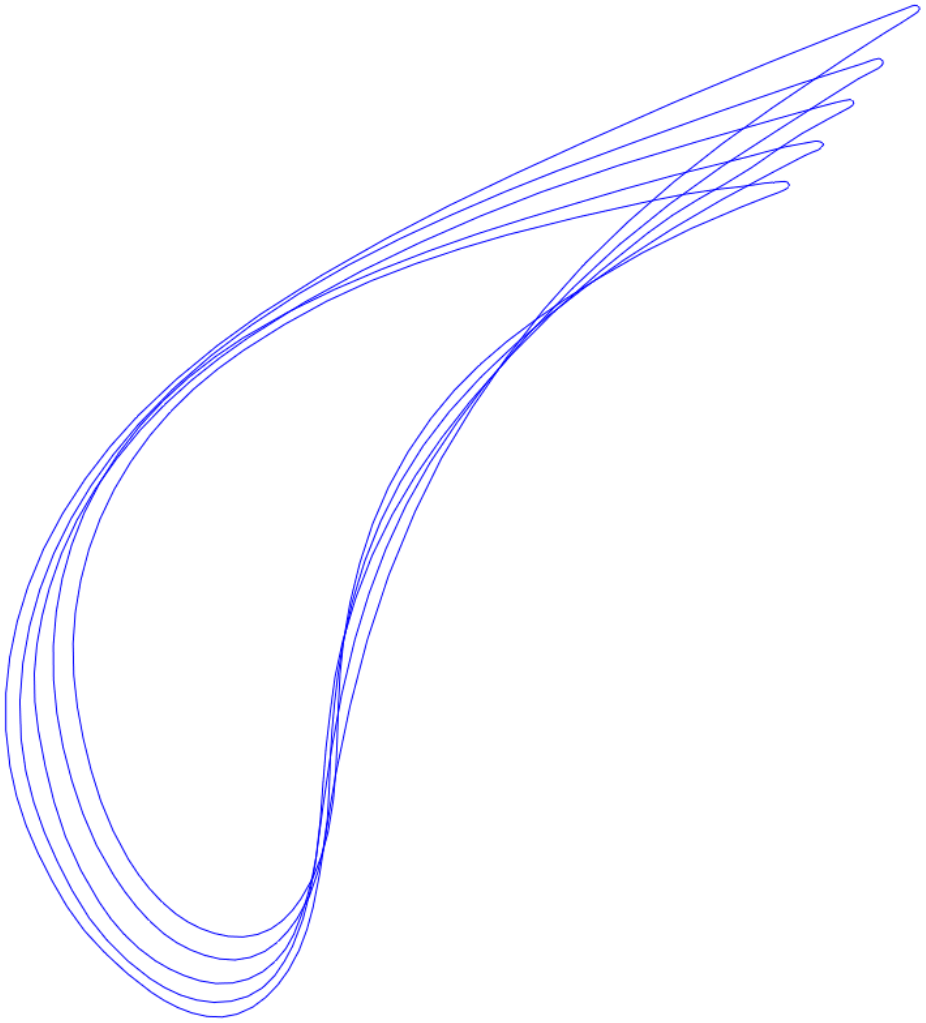

Figure 38. Nozzle/stator blade section profile data.

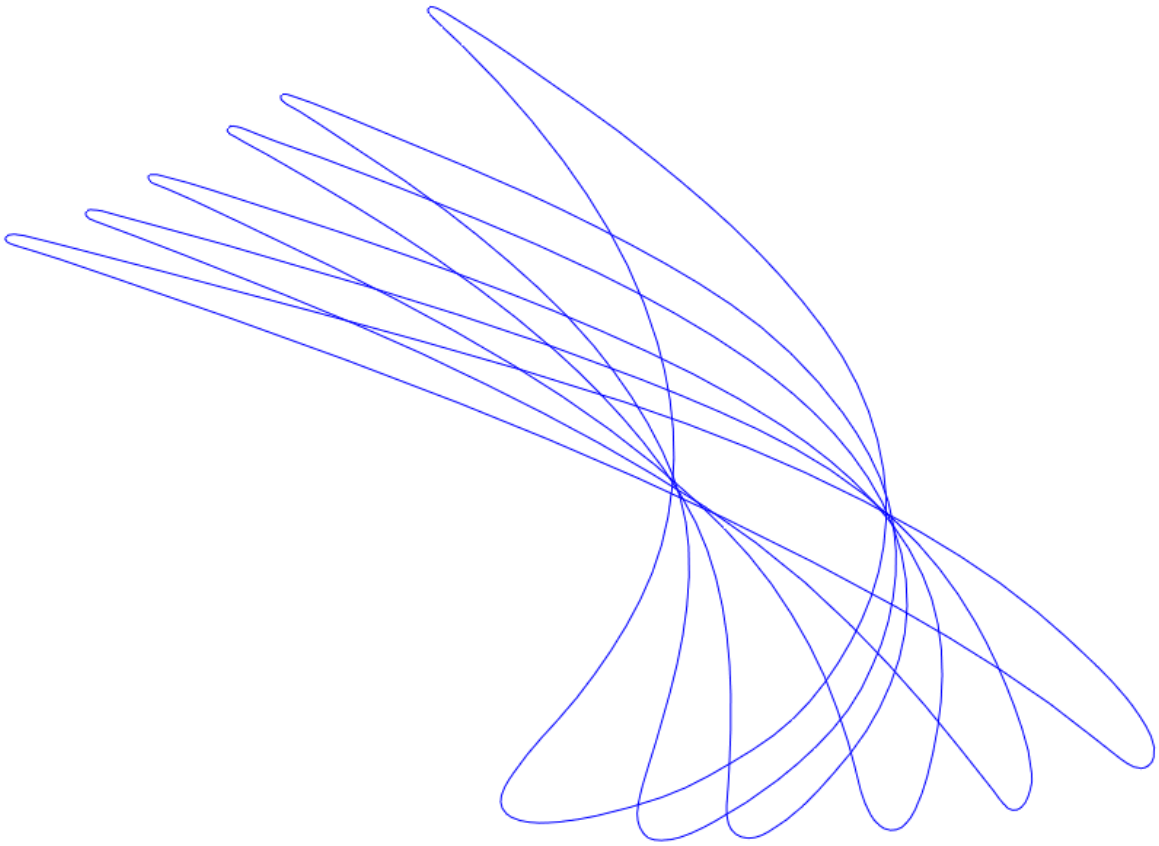

Figure 39. Rotor blade section profile data.

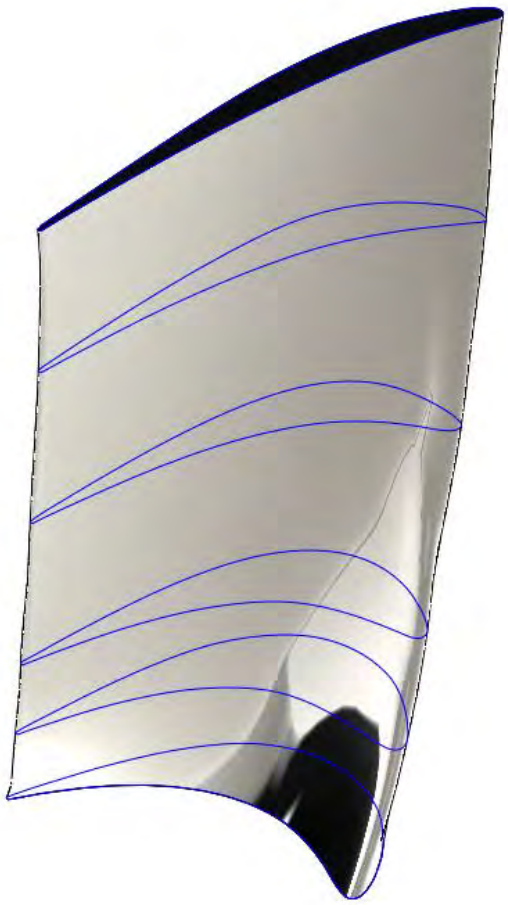

Figure 40. A turbine blade model developed by curve fitting the cross section data.

Due to the high degree of twist in the blades, linear interpolation of the data points would not result in an accurate representation of the geometrical information. A curve fitting software package, TableCurve 2D was used to fit curves to the given data points. The function of the curve could then be used to calculate geometrical data at the required radial stations depending on the discretisation scheme used.

5.2.6 Obtaining turbine geometry in an industrial setting

Another approach that was explored was to develop a complete 3D CAD model from the given data. The CAD software has built-in functions that can interpolate between the 2D profile curves in order to develop a 3D body. The premise was that it would then be possible to measure up the 3D CAD model in a conceptually similar way as to how an engineer would measure up a turbine. Following some exploratory exercises with the CAD model it became

clear that physically measuring up a turbine to obtain the required geometrical inputs for the present modelling approach is a huge endeavour in itself, but practicable. The importance of this is that the plant engineer will rarely have access to detailed drawings of turbine blades, but as the custodian of the turbine he always has access to take measurements for himself.

It is very useful to have a 3D model when developing the thermofluid model of a physical turbine. For example, the impact of the high degree of blade twist seen in Figure 40 and Figure 41 on the discretisation scheme only becomes apparent when studying the 3D model. Small gaps that are necessitated by geometrical features such as the labyrinth seal entrance and exit cavities were also highlighted. However, as explained in 5.2.5, in the present case the general input data was obtained from the design information published in Fottner (1990).

Figure 41. A View of the 3D CAD model of the turbine rotor.

5.3 Model validation

In this section the results of modelling the test case according to the methodology described in the previous chapters are compared to the test data published by AGARD (1990). The published data contains data at five measuring stations within the turbine and as such only the model results for those positions have been extracted from the complete set of model results for comparison. Three models with different discretisation schemes were developed. The general approach of discretisation illustrated in Figure 23 was used. The first model uses a mean diameter of each blade passage while the second and the third model use three and five elements in parallel to discretise each blade passage in the radial direction. Seven test cases were modelled namely; a nominal case and six off-design cases with varying degrees of relative speed and relative mass flow as described in Table 7. These cases correspond to the test data published by AGARD (Fottner, 1990).

The program performed well and converged for all the test cases. Various degrees of relaxation to the pressure correction and/or the mass flow rate calculation was required to ensure convergence. None of the test cases resulted in choked flow after convergence. During the iteration process, some of the flow elements became choked as the pressure corrections fluctuated, but converged to a Mach number of less than one for this test case.

5.3.1 Model calibration

In applying the newly developed model it was found that the loss models that have been selected slightly underestimate the losses of this test case. This results in calculated efficiencies that are approximately 4% too high through the range of tests. In the loss model of Kacker and Okapuu (1982), the authors noted that the loss models overestimated the losses for modern turbines due to improvements in efficiency and suggested correcting the profile loss by a factor of 0.66.

Benner, et al. (2004), performed wind tunnel work on a turbine blade cascade and compared measured results with that of Ainley and Mathieson (1951), Dunham and Came (1970) and Craig and Cox (1970). They observed significant differences between the losses measured and those predicted of at least a factor of two. They noted that loss correlations obtained in wind tunnel tests on cascades are normally scaled or calibrated to reproduce stage efficiencies of real turbine data and attributed the differences between their measured data and the models to this calibration process. They again highlight the fact that there are significant loss

generating mechanisms in a real turbine that are not captured in cascade testing. The result is that calibration of the model will generally be required to account for these differences.

The calibration approach used in the present work is aimed at making the least adjustments necessary to the loss models in order to fit the calculated results to the modelled data. The turbine performance curve for a range of relative mass flow rates was used to calibrate the model. The test data in Figure 42 shows that the uncalibrated model represents the stated design point efficiency well. The curve obtained by the uncalibrated model over predicts the efficiency at reduced relative mass flow rates. Therefore the losses attributed to these off-design conditions appear to be under predicted. The calculated incidence loss coefficient was multiplied by a factor of three and a factor of four in calibration tests one and two respectively. Multiplying the incidence loss coefficient by four brings the curve closer to the test data curve for a broad range of relative mass flow rates.

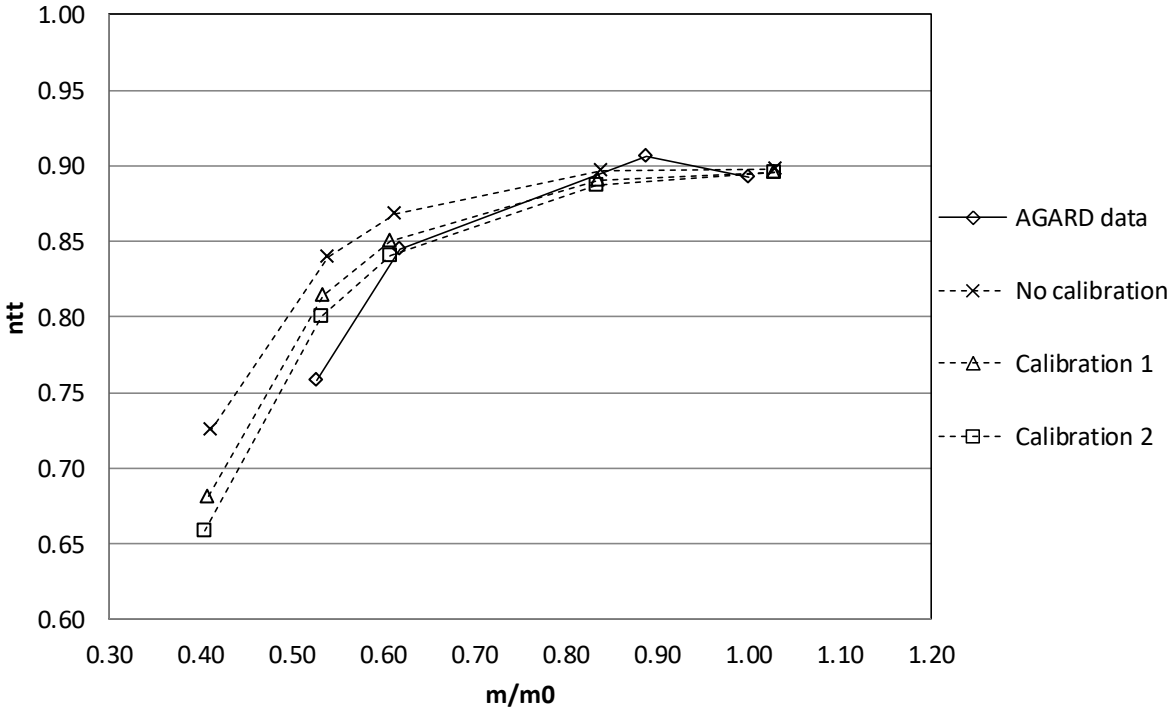

Figure 42. Comparison of three turbine performance curves at n/n0=1 with different calibrations.

5.3.2 Nominal case

The results of three models namely; model 1, model 3 and model 5, were compared to the AGARD test data. Each model differs in the discretisation scheme used to model the stator and rotor passages. The numeral refers to the number of radial elements of the stator and rotor passages in the respective models. Discretisation approaches similar to that illustrated in Figure 20 for a single radial element and Figure 23 of three radial elements were applied. An additional model was created with five radial elements. Figure 43 shows isometric views of the calculation meshes and calculated flow vectors for the three models.

A comparison of internal flow parameters is presented here for the three models at the design condition or nominal case. The modelled results and the AGARD test data are compared at five axial stations in the turbine. Station zero and four represent the turbine inlet and outlet respectively and stations one to three represent points between each stage. A stage comprises of a stator and rotor set. The data sets are named according to the description in Table 8.

Table 8. Description of model names

Model name	Simulation	Dataset name	Number of radial elements per blade row
model 1	nominal case	TF401	1
model 3	nominal case	TF402	3
model 5	nominal case	TF403	5

Figure 43 a,b and c shows the isometric views and Figure 44 a,b and c the front views of the calculated flow vectors for the three models. The vectors are coloured according to the legend given in Table 6. The three models show that there is a significant difference in the velocity vectors calculated near the root and the tip of the blade. The velocity vectors at the exit of the rotor stages are nearly in an axial direction even near the root and tip areas calculated in model 3 and model 5.

Figure 45 shows the same meshes from the side view. The radial component of the flow vectors near the blade tip is evident in this view. The results also show the significant difference in leakage between the stator shaft seal and the blade tip gap. As expected the gap at the blade tip allows more leakage.

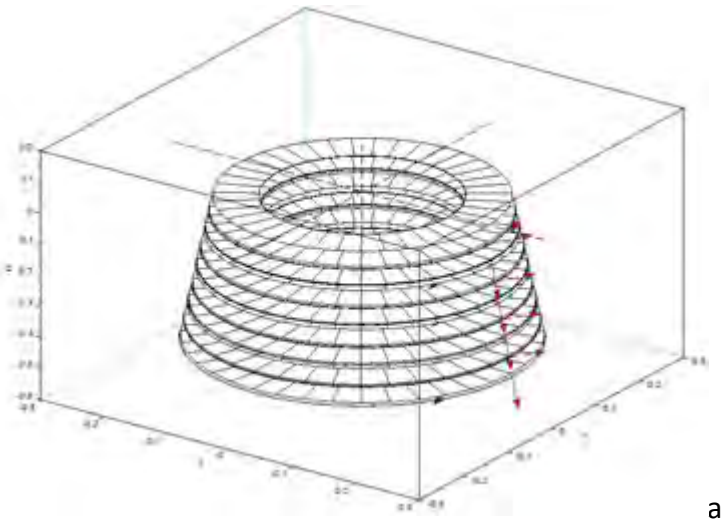

a. model 1

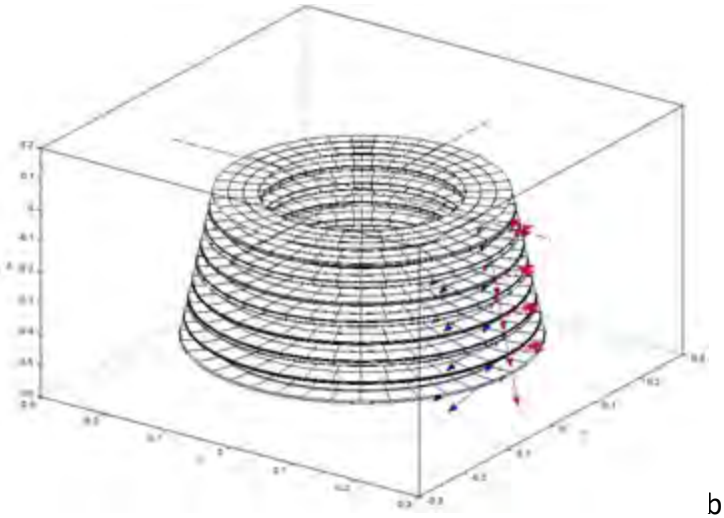

b. model 3

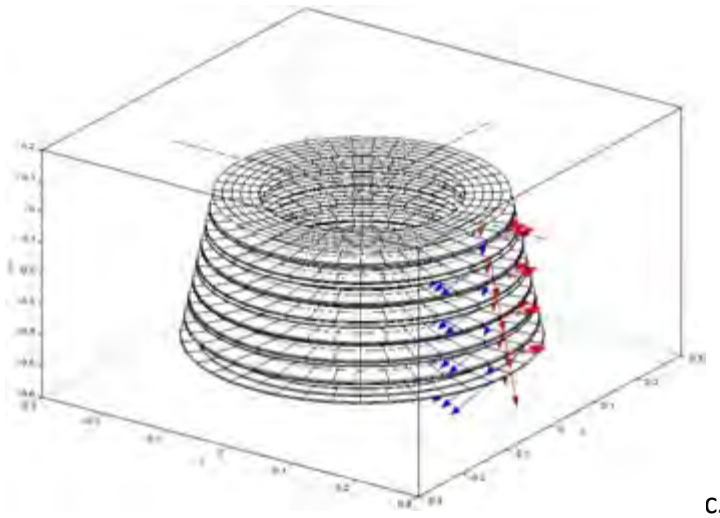

c. model 5

Figure 43. Isometric views of simulation model 1, model 3 and model 5 with one, three and five radial elements respectively representing the stator and rotor blade passages. See Appendix C for enlargements.

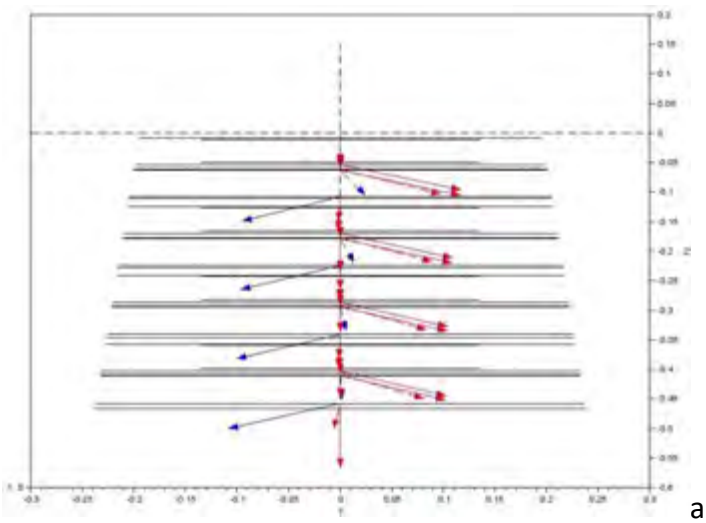

a. model 1

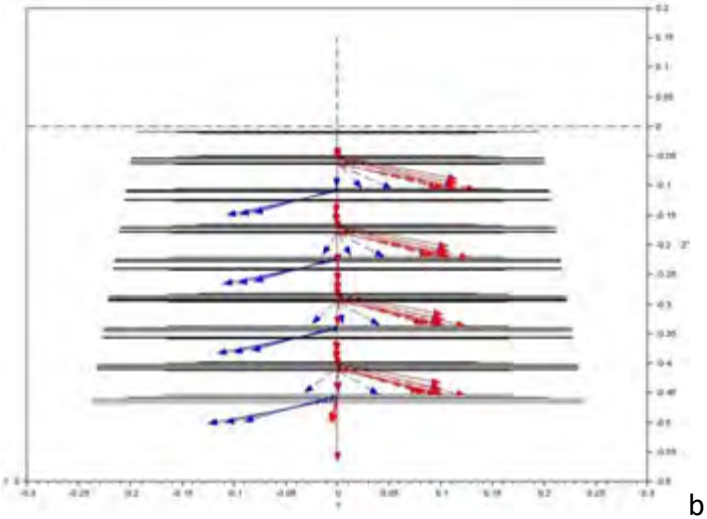

b. model 3

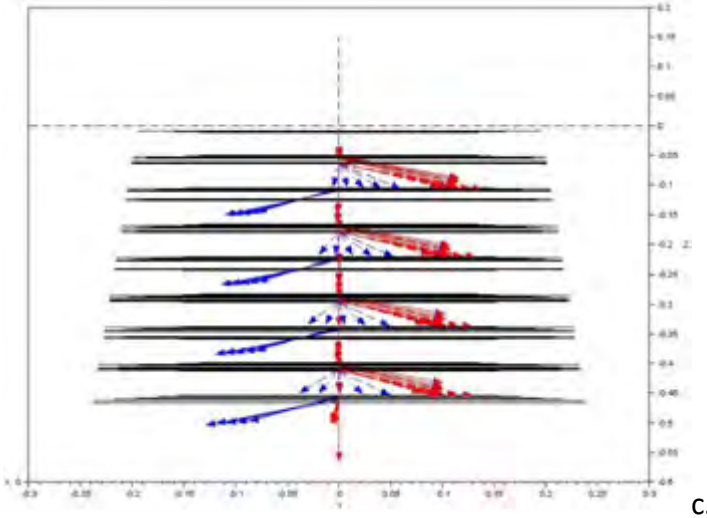

c. model 5

Figure 44 Front views of simulation model 1, model 3 and model 5 with one, three and five radial elements respectively representing the stator and rotor blade passages. See Appendix C for enlargements.

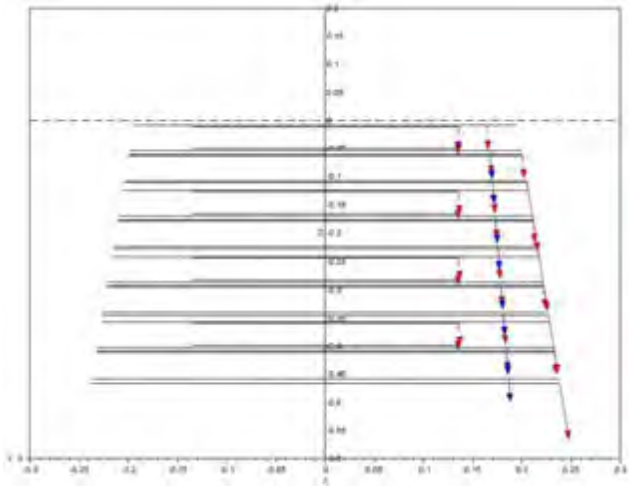

a. model 1

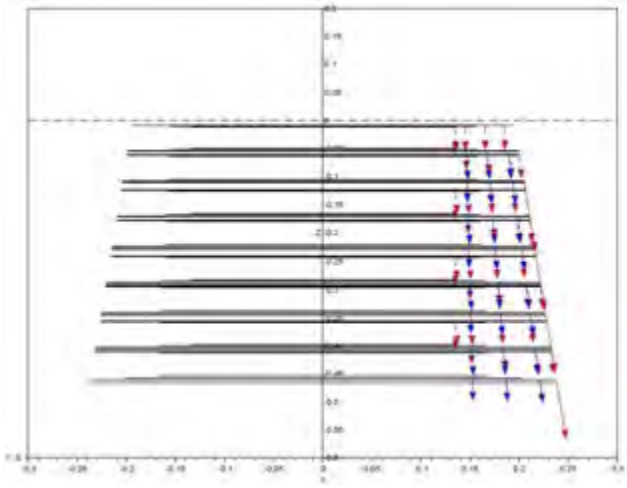

b. model 3

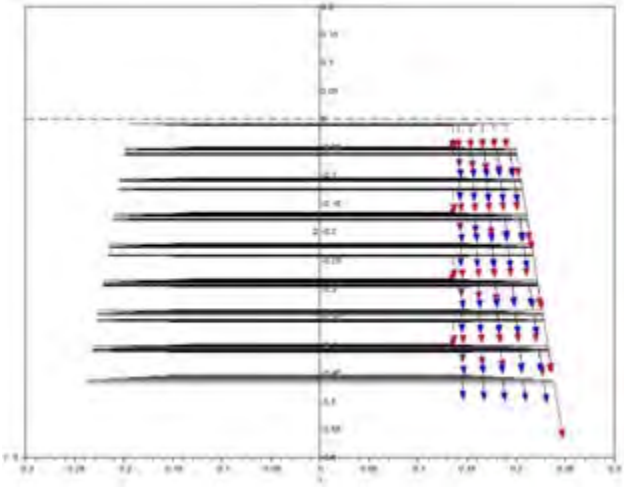

c. model 5

Figure 45. Side views of simulation model 1, model 3 and model 5 with one, three and five radial elements respectively representing the stator and rotor blade passages. See Appendix C for enlargements.

In Figure 46 and Figure 47 the measured values of total pressure and total enthalpy are compared directly to simulation results at the measuring stations described in paragraph 5.2.3. These two parameters are solved for in the conservation of momentum and conservation of energy calculations respectively. There is a good qualitative agreement between the modelled values and the measured data.

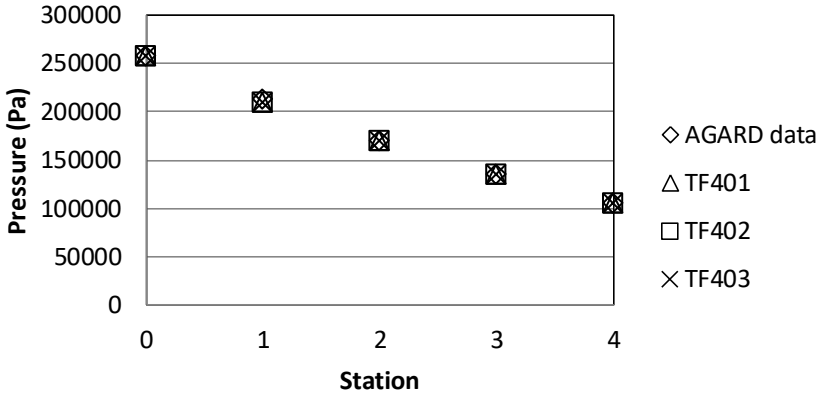

Figure 46. The total pressure data at 5 stations of the test data and calculated results.

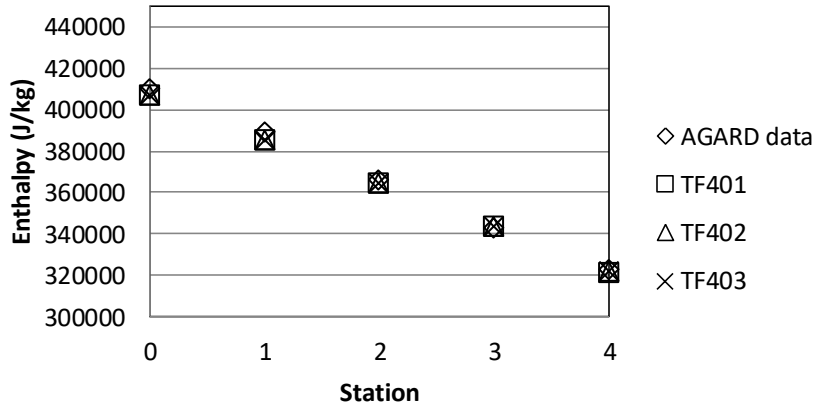

Figure 47. The total enthalpy data at 5 stations of the test data and calculated results.

In order to quantify this agreement the modelled results are also compared with the measured data by calculating the percentage difference between the calculated results and the measured data for each point. This is illustrated in Figure 48 and Figure 49

Figure 48. The percentage difference in total pressure between the test data and calculated results.

Figure 49. The percentage difference in total enthalpy between the test data and calculated results.

The maximum deviation in total pressure of 1.6% occurs at station 1 and the total enthalpy values are predicted with an error of <1%. The results obtained by all three models are similar.

The static pressure provides a representation of how well the model predicts the flow velocities. The static pressures have an accuracy with a maximum deviation of <1.7% occurring at station 4.

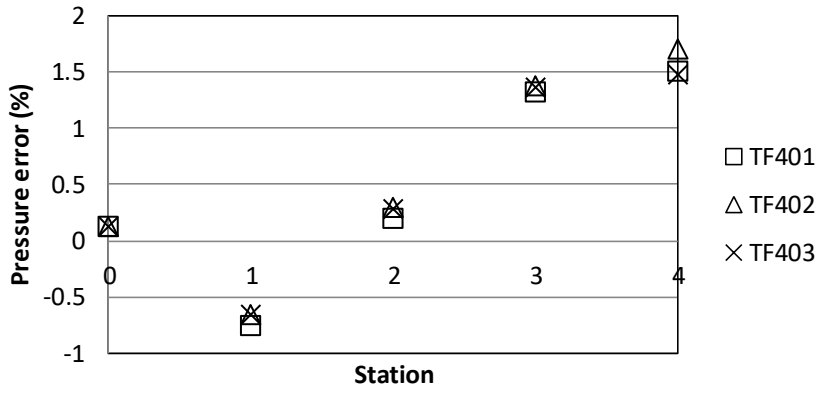

Figure 50. The percentage difference of static pressure between the calculated results and the test data.

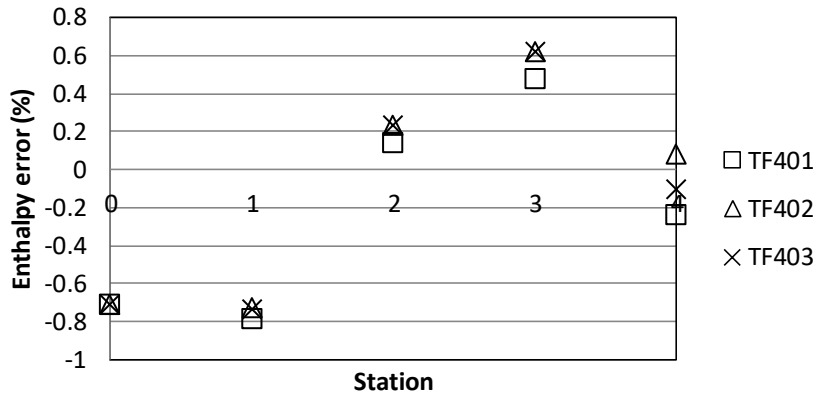

Figure 51. The percentage difference of static enthalpy between the calculated results and test data.

Although no enthalpy values are provided in the test data, it has been calculated from the measured temperatures and compared with the modelled results. The enthalpy is considered to be a good representation of the model's ability to predict the real turbine's characteristics. The static enthalpy deviates less than 3kJ/kg which results in an error of <0.7%.

The results obtained by the three models for the nominal condition are very similar.

5.3.3 Off-design operation

The model's off-design performance predictions were compared with six different off-design cases. Test data for these cases were published by AGARD (Fottner, 1990). The resulting efficiencies are plotted below for a range of relative mass flow rates and two relative velocities. These simulations were performed by specifying the pressure ratio at the boundaries and calculating the relative mass flow rate. The results of all three models namely; model 1, model 3

and model 5, were again compared to the AGARD test data. In Figure 52 the modelled efficiencies show a good agreement with the test data. At nominal conditions, the efficiency has an error of <1%. The efficiency curve at off-design conditions is represented well, but appears to be over predicted for the lower mass flow rates at nominal rotating speed.

Results of the models discretised into one, three and five radial elements are shown and the results for this exercise again show that there is very little difference in the results obtained by the three models. The models with more elements do appear to predict the losses at severe off-design conditions slightly better, predicting a lower efficiency for those mass flow rates.

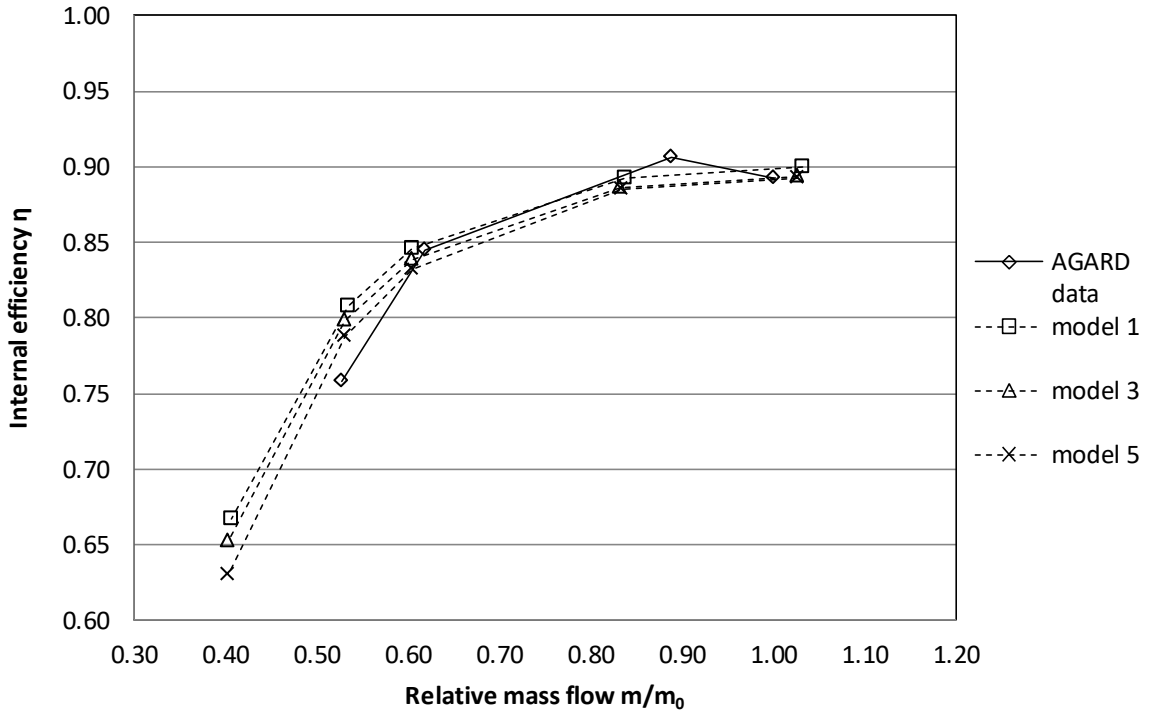

Figure 52. Plot of turbine efficiency test data and modelled results at n/n0=1.

Figure 53 shows that all three models slightly over predict the mass flow rate at the nominal condition. This improves for smaller pressure ratios. The accuracy of the calculated mass flow rate is within <3% of the test data for all three models. There is practically no difference in the results obtained by the three models.

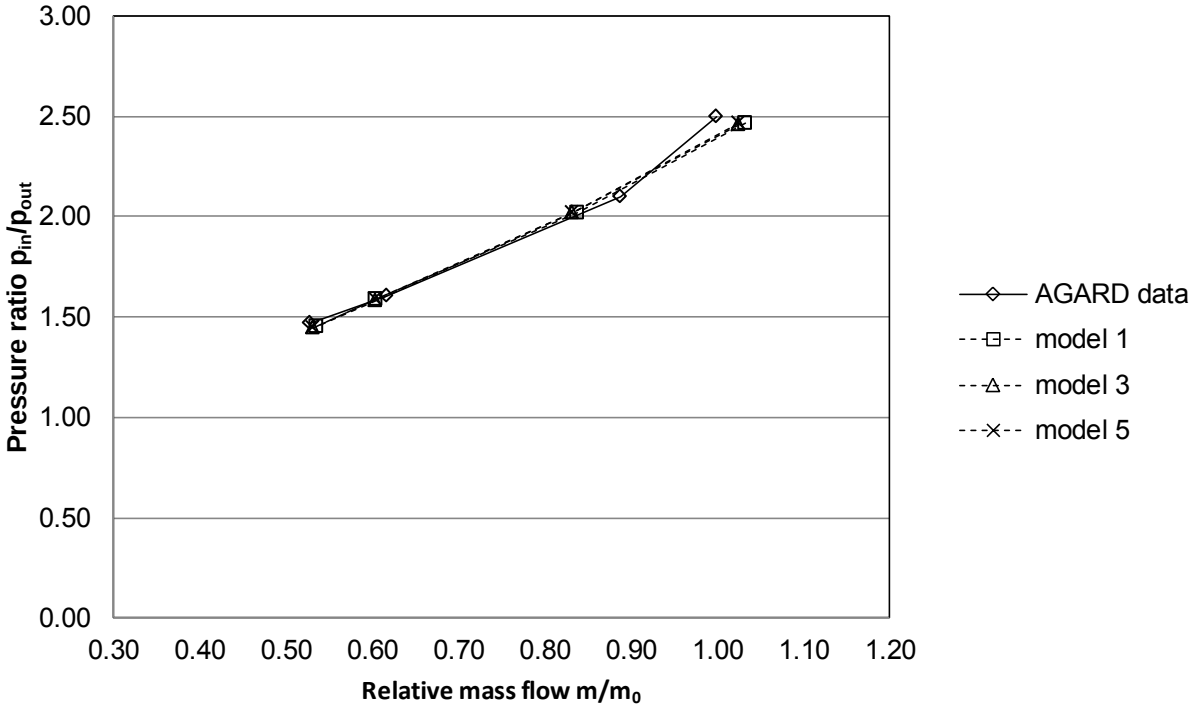

Figure 53. Plot of turbine pressure ratio test data and modelled results at n/n0=1.

Figure 54 shows that for a relative speed of 0.75, the modelled efficiency is not as well predicted as at the nominal speed ratio. The efficiency is over predicted by up to 4% for a relative mass flow rate of around 0.5.

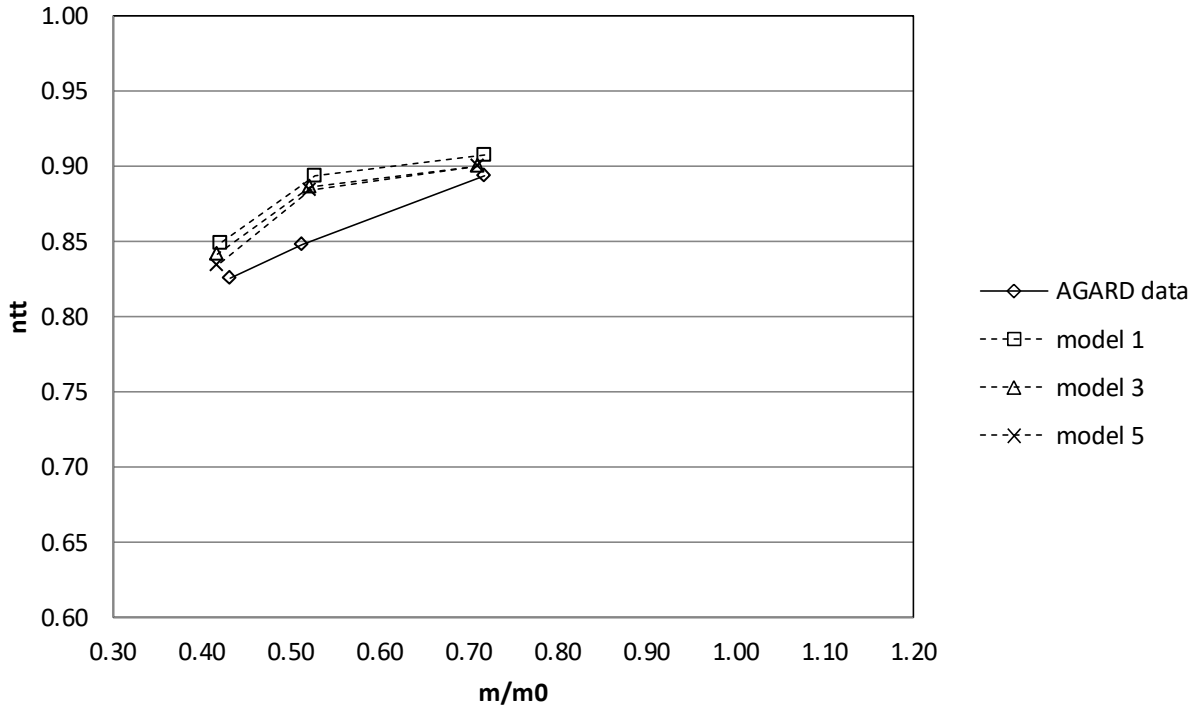

Figure 54. The turbine characteristic at a relative speed ratio of 0.75 determined from test data and calculated results.

The mass flow rates are predicted very well at the reduced relative speed ratio and reduced pressure ratios illustrated in Figure 55.

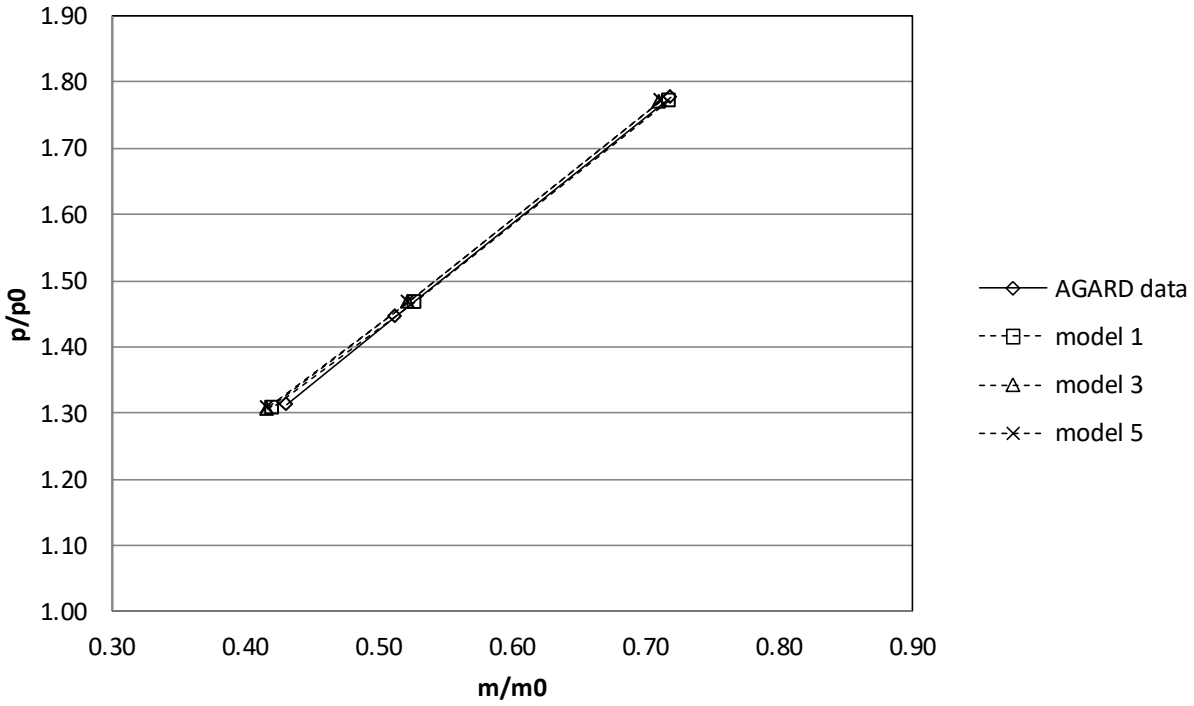

Figure 55. The turbine relative mass flow characteristic at a relative speed ratio of 0.75 determined from test data and calculated results.

From the modelled results it is possible to obtain very useful data about the turbine. In Table 9 the torque and power developed in the stator and rotor rows as calculated with model 1 at the nominal condition are provided. It is also possible to extract the pressure drop due to the fluid performing work on the rotor and the pressure loss due to losses in the flow.

Table 9. Power and torque developed on a stage-by-stage basis.

Flow element	Torque (N.m)	Power (kW)	Pressure rise due to work performed (kPa)	Pressure rise due to losses (kPa)
Stage 1 stator	233.41	-	-	-1.797
Stage 1 rotor	-233.33	-183.254	-44.128	-3.299
Stage 2 stator	228.14	-	-	-1.256
Stage 2 rotor	-221.82	-174.215	-35.784	-2.561

Stage 3 stator	221.97	-	-	-0.974
Stage 3 rotor	-221.55	-174.004	-30.364	-2.166
Stage 4 stator	227.89	-	-	-0.771
Stage 4 rotor	-236.89	-186.051	-27.150	-2.021

Table 10 shows data extracted about the mass flow rate through the individual elements. In this way it is possible to obtain the detailed mass flow rate through each stator and rotor stage and the amount of fluid that bypasses the stator and rotor via the seals. The results show that there is significantly more leakage through the rotor tip region than through the stator labyrinth seals. This is expected because of the efficacy of labyrinth seals.

Table 10. Mass flow rate data on a stage-by-stage basis.

Flow element	Blade passage flow (kg/s)	Leakage flow (kg/s)
Stage 1 stator	8.328	0.011
Stage 1 rotor	8.191	0.147
Stage 2 stator	8.330	0.008
Stage 2 rotor	8.218	0.120
Stage 3 stator	8.332	0.007
Stage 3 rotor	8.239	0.100
Stage 4 stator	8.333	0.006
Stage 4 rotor	8.254	0.085

5.4 Chapter summary

In general the three models appear to predict the efficiency well at nominal conditions. This is expected as the models were calibrated for the nominal case. The models predict the efficiency well for a range of relative mass flow rates around the nominal condition and clearly capture

the effects of off-design operation. This required some adjustment of the losses associated with off-design conditions in order to capture the magnitude of these losses in the test case. As expected, the prediction becomes less accurate at off-design operation.

Using a model with more discrete elements along the radial blade length does not result in a more accurate estimation of the turbine overall efficiency for this model, however there is a slight improvement in the prediction of losses at severe off-design conditions. This effect would possibly be more pronounced for turbines with large aspect ratio blades.

Chapter 6. Demonstration of model

6.1 Hypothetical off-design conditions

One of the objectives of this study was to develop a simplified model that is suitable for engineering studies in the plant environment. More accurate models do exist, but the benefit of simplified models is to broaden their applicability while maintaining their usefulness as engineering tools. To illustrate this, the model was applied to some hypothetical problems that plant engineers may be faced with.

The general approach in this exercise was to apply a hypothetical off-design condition to the model and then compare the modelled results with the data from the nominal modelled case. The methodology will allow the engineer to explore various aspects and the effect on the turbine performance in order to diagnose problems and investigate possible routes to address them.

6.1.1 General internal fluid leakage

In this simulation, seal gap sizes were adjusted to represent a typical case of undue wear of internal seals that is often associated with damage caused by high vibrations during start-up conditions, misalignment of the turbine internal parts or distortion of turbine internal parts. The model results are compared with the modelled nominal case data in Figure 58 and Figure 59. Thus the deviations from nominal conditions caused by the enlarged seals are calculated.

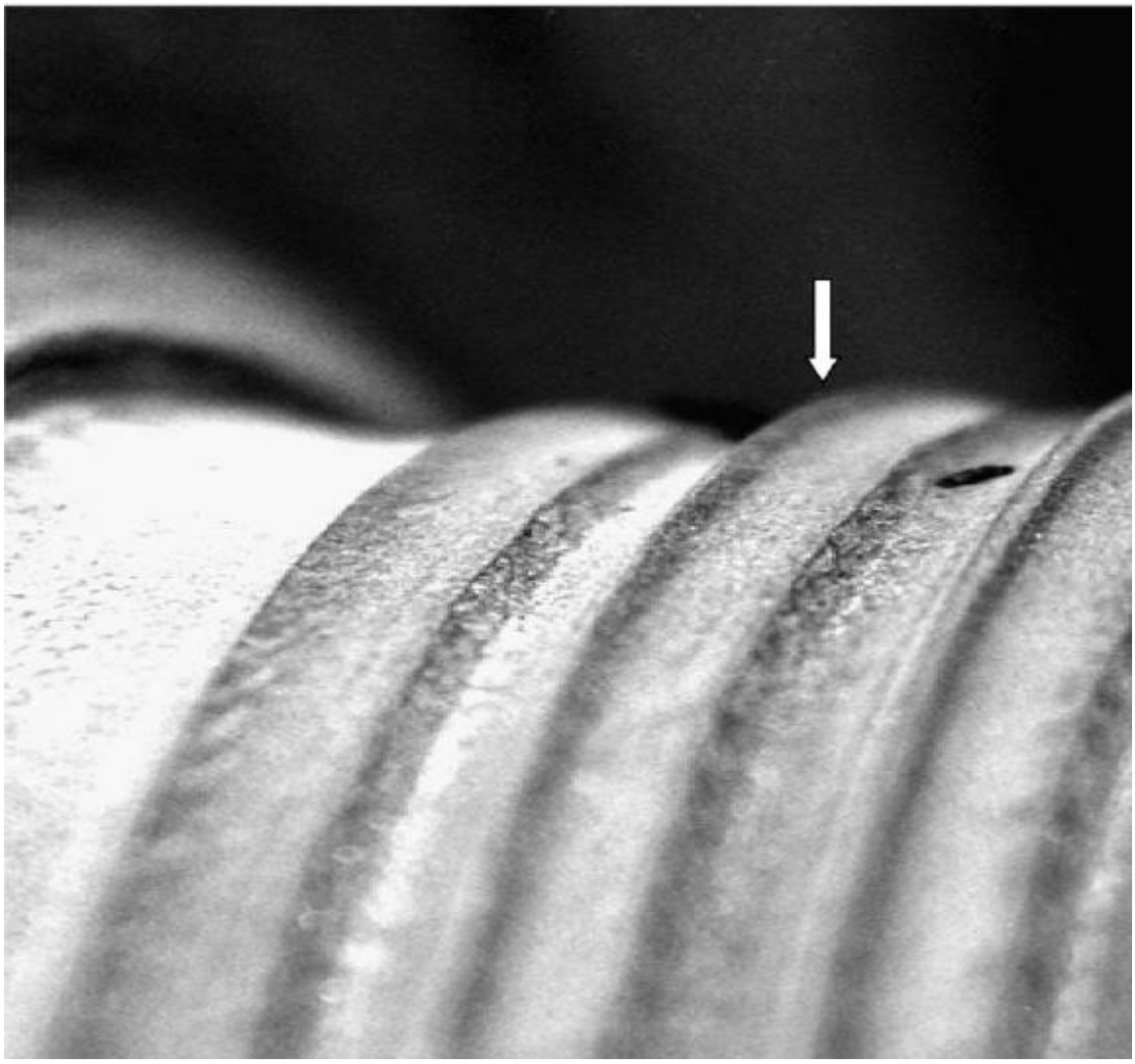

Figure 56. Sealing castellations that have been worn away by erosion (Mazur, et al., 2002).

Leakage of the internal seals causes the working fluid to bypass the stator and rotor blade elements and therefore pass through the turbine stage without performing useful work. When there is a leakage in every stage the effect accumulates. The fluid therefore exits the turbine at a higher energy condition compared with the nominal exhaust conditions. The leakage also affects the overall performance of the turbine. In Figure 57 one can see the impact on turbine efficiency through a range of relative mass flow rates for three cases compared with the nominal condition. It is also observed that for each case there is a slight increase in mass flow rate due to the enlarged seal gap area. The cases are described in Table 11.

Table 11. Description of off-design cases

Case name	Description
AG_1D	Data obtained from model with 1 radial discretisation.
AG_1D_multiseals_0.0005	Results of model with 1 radial discretisation and all internal seals enlarged to 0.5mm.
AG_1D_multiseals_0.001	Results of model with 1 radial discretisation and all internal seals enlarged to 1mm.
AG_1D_multiseals_0.0015	Results of model with 1 radial discretisation and all internal seals enlarged to 1.5mm.

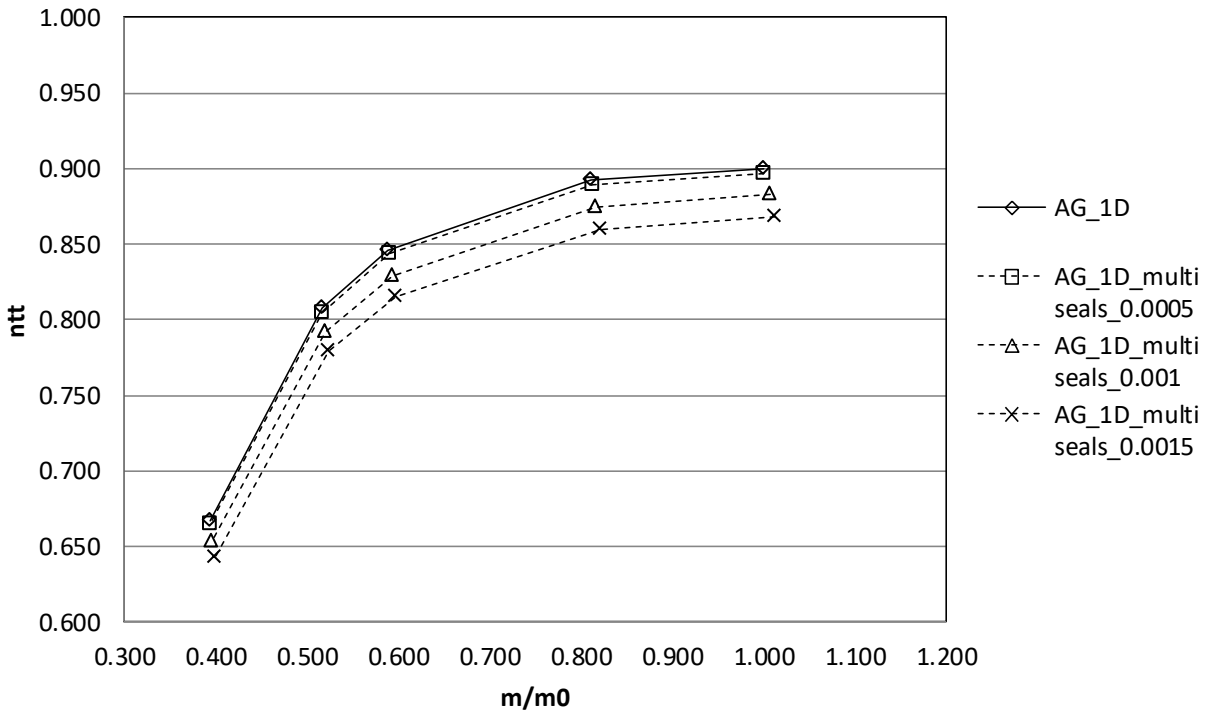

Figure 57. Turbine performance n/n_0=0.75 modelled with poor internal sealing.

The effect on the exhaust conditions can be seen in Figure 58 and Figure 59 as an increase in exit temperature resulting in a higher enthalpy condition. As the seal size is increased, the enthalpy increases at all the points modelled.

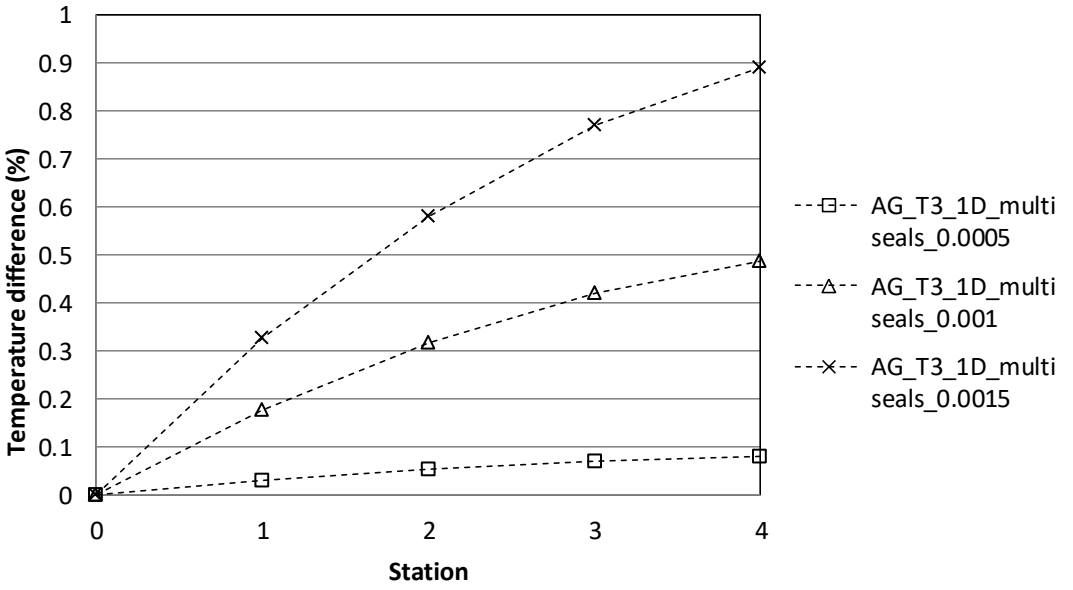

Figure 58. A comparison of total temperature between the calculated results at nominal condition and the calculated results for the turbine modelled with internal leakage.

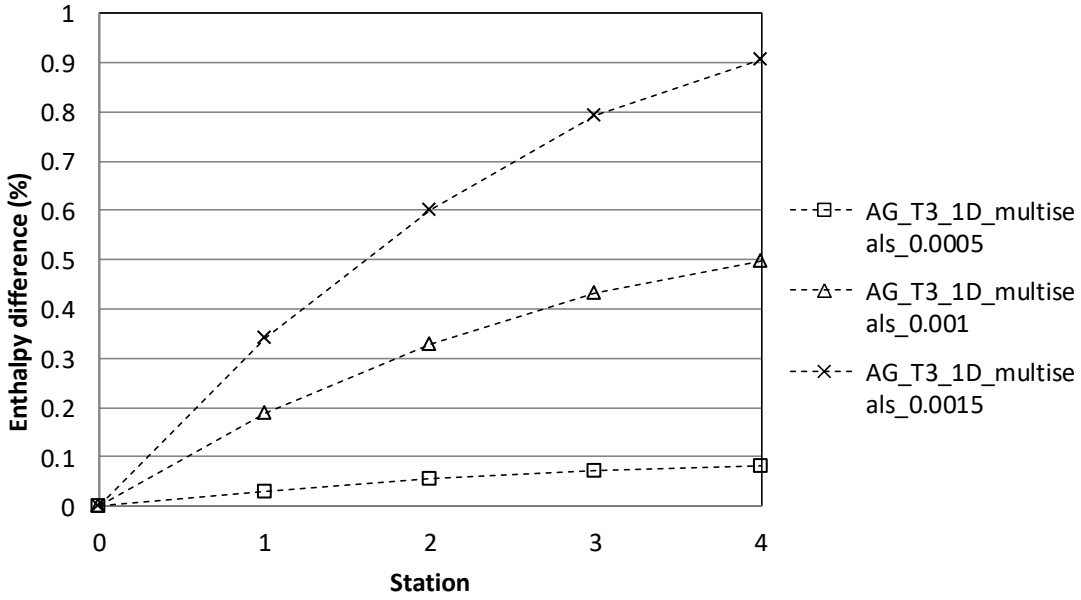

Figure 59. A comparison of total enthalpy between the calculated results at nominal condition and the calculated results for the turbine modelled with internal leakage.

6.1.2 Leakage confined to specific seals

The second investigation looks at three different cases of individual seals leaking at various positions inside the modelled turbine. The three cases are described in Table 12. Individually leaking seals can be caused by non-conformance to design seal gap specifications during assembly of the machine.

Table 12. Description and results of off-design cases of single enlarged seals.

Case name	Description	Rotor work (kW)	Efficiency	Mass flow rate (kg/s)
AG_T3_1D	Modelled case data of the nominal condition	717.524	0.900	8.339
AG_T3_1D_2nd_stage_noz_seal	Modelled case data of the modelled turbine with stage 2 stator seal enlarged to 0.5mm.	717.902	0.900	8.343
AG_T3_1D_2nd_stage_rot_seal	Modelled case data of the modelled turbine with stage 2 rotor seal enlarged to 1.0mm.	715.065	0.896	8.349
AG_T3_1D_3rd_stage_noz_seal	Modelled case data of the modelled turbine with stage 2 stator seal enlarged to 1mm.	717.729	0.900	8.341

Some interesting observations can be made from the detailed results. In the cases with leakage in the stator seals, an increase in power output is observed. This can be attributed to the slight increase in mass flow rate due to the increased flow area which results in a higher flow through the rotor blade elements. It can also be seen that this increased output comes at a cost because the efficiency of the machine is reduced.

In the case with an enlarged rotor seal, the overall power output is reduced. This can be attributed to the flow bypassing the rotor blades without doing work. In this case the overall efficiency also decreases.

In steam turbine plants pressure and temperature are typically measured at bleed points in the turbine. In Figure 60 the difference in total temperature for the three off-design cases compared to the nominal modelled case is presented. The leakages past the stage 2 and 3 stators have little effect on the temperature. For the model with leakage past stage 2 rotor, a significant rise is seen in the total temperature after that stage. This can be attributed to the flow passing the rotor without performing work.

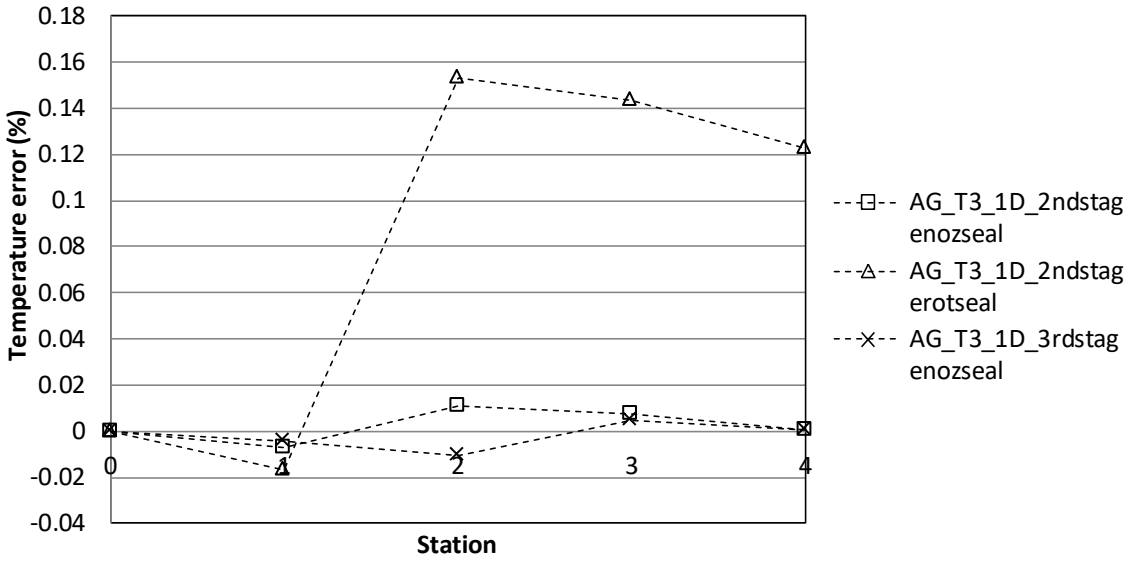

Figure 60. A comparison of total temperature between calculated results at nominal condition and the calculated results for the turbine modelled with internal leakage.

The difference in calculated static pressures between the off-design cases and the nominal modelled case is illustrated in Figure 61. The increased size of seal gaps appears to cause a slight reduction in static pressures upstream of the leakage and a slight increase in static pressures downstream of the leakage for the respective models. The static pressure reduction upstream of the leakage could be attributed to the increased mass flow rate resulting in a higher velocity. The slight increase in pressure at the downstream points may be attributed to the reduced pressure drop across the enlarged seal.

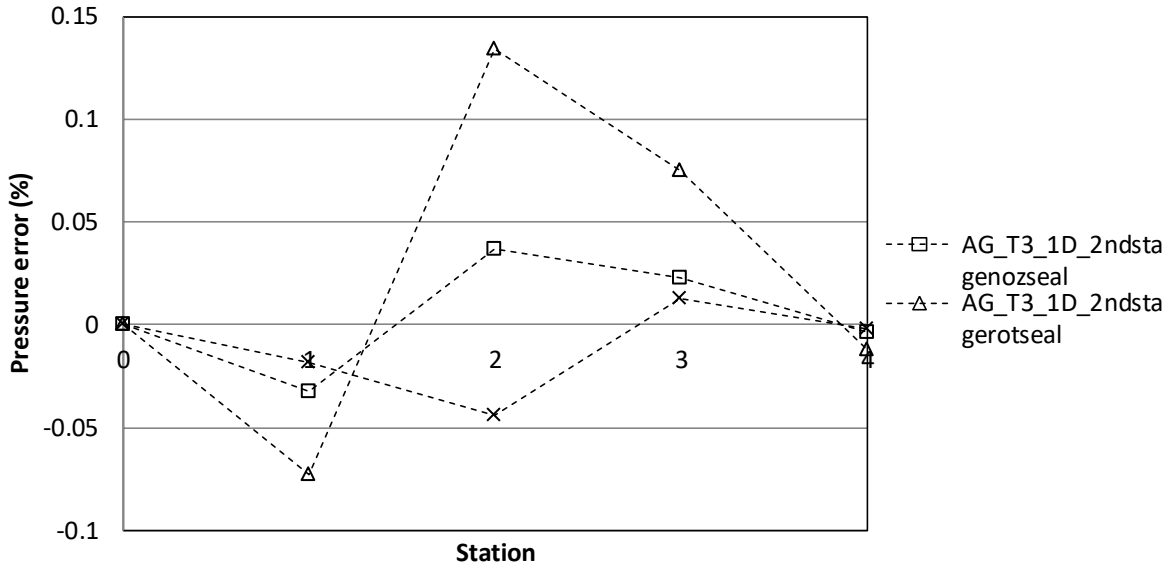

Figure 61. A comparison of static pressure between the test case data and calculated results at nominal condition and the calculated results for the turbine modelled with internal leakage.

6.1.3 Turbine blade erosion

Turbine blades can be eroded by solid particles or by water droplets that often form in steam turbines. The resulting effect is a change in the effective angles of the blade row. Often the erosion is not uniform across the length of the blade, but much more severe towards the blade tip where the tangential velocity is higher. Figure 62 shows an example of a steam turbine blade row with severe erosion. The erosion is more pronounced towards the tip of the blades.

Figure 62. An example of turbine blades eroded in the tip region (Almasi, 2011).

In the following test, the modelled blade angle is adjusted at the last stage. A three element discretisation was selected for this simulation to illustrate how the dicretisation scheme can be used to perform a detailed simulation of a localised problem. Three elements are used along the length of the blade and the change of angle is only applied to the element representing the tip area of the blade. The nominal pressure drop across the turbine is maintained in all the cases. The three off-design cases modelled are described in

Table 13.

Table 13. Description and results of off-design cases of turbine with blade erosion.

Case name	Description	Rotor work (kW)	Efficiency	Mass flow rate (kg/s)
AG_T3_3D	Modelled case data of the nominal condition	717.524	0.900	8.337
AG_T3_3D_erosion_10deg	Modelled case data of the modelled turbine with stage 4	713.379	0.893	8.354

	rotor blade tip region eroded by 5 degrees			
AG_T3_3D_erosion_20deg	Modelled case data of the modelled turbine with stage 4 rotor blade tip region eroded by 10 degrees	717.149	0.885	8.402
AG_T3_3D_erosion_30deg	Modelled case data of the modelled turbine with stage 4 rotor blade tip region eroded by 20 degrees	711.979	0.856	8.479

The first effect that is noticed is that the reduced blade angle changes the effective area of flow through the blade passage. This effect can be clearly seen by inspecting the eroded blades in Figure 62. An increase in mass flow rate of 1.7% is noted in the turbine with 20 degrees of blade tip erosion. The power output of the turbine is also adversely affected, but this effect is offset by the increased mass flow rate. The turbine efficiency is severely reduced by almost 5% for the same case. This highlights the impact that even localised blade erosion in a single stage can have on the overall performance of a turbine.

In Figure 64 an increase in velocity is observed in all stages of the turbine and in particular the exhaust. The increased velocity in the initial stages can be attributed to the increased mass flow. The reduced relative exit angle also results in a significant increase in exhaust absolute velocity as the flow retains a significant amount of angular momentum through the eroded element located in the last stage.

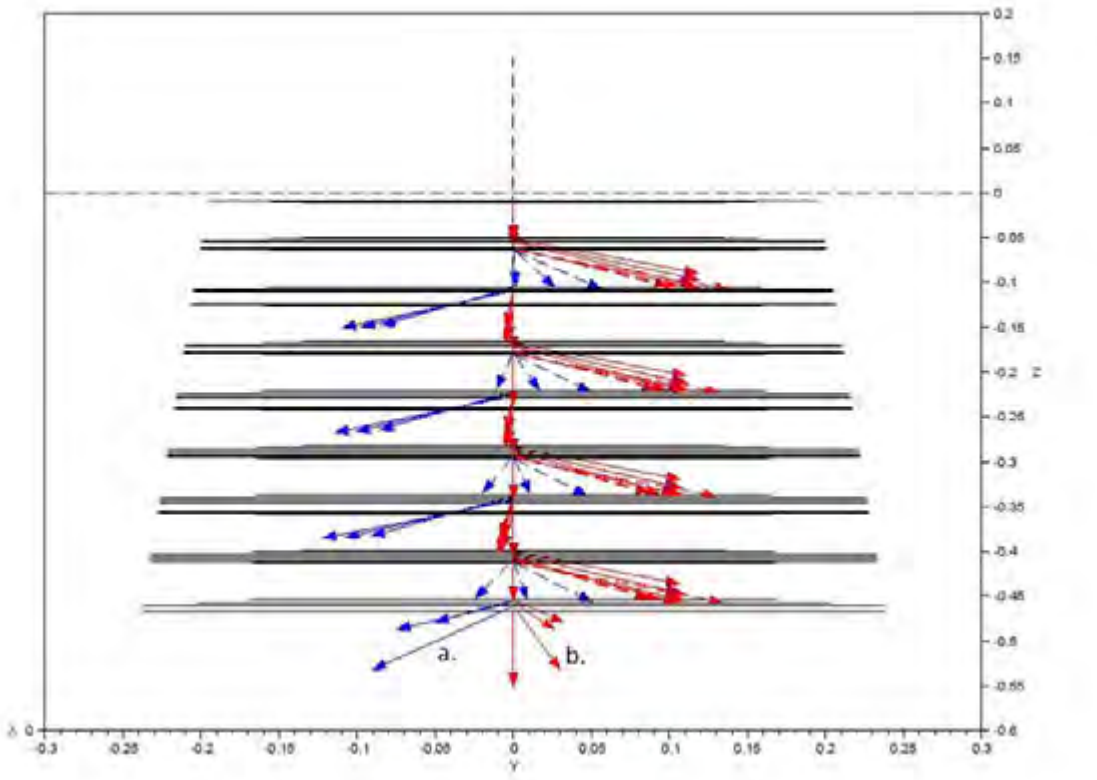

Figure 63. A front view of the simulation model with the stage 4 rotor blade outlet angle eroded in the tip region.

The impact of blade erosion is visualised in Figure 63. The significant deviation in the velocity triangle can be seen when one compares the outlet absolute velocity vector in the tip region to the same vector in Figure 44 representing the nominal condition. Vector a. represents the outlet relative velocity vector and b. represents the outlet absolute velocity vector of the eroded blade element.

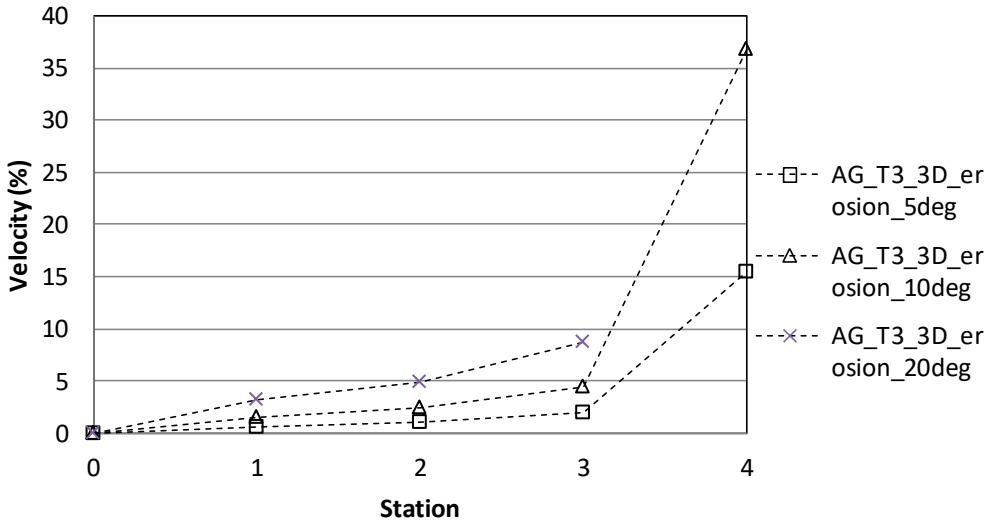

Figure 64. A comparison of absolute velocity between the test case data and calculated results at nominal condition and the calculated results for the turbine modelled with blade erosion.

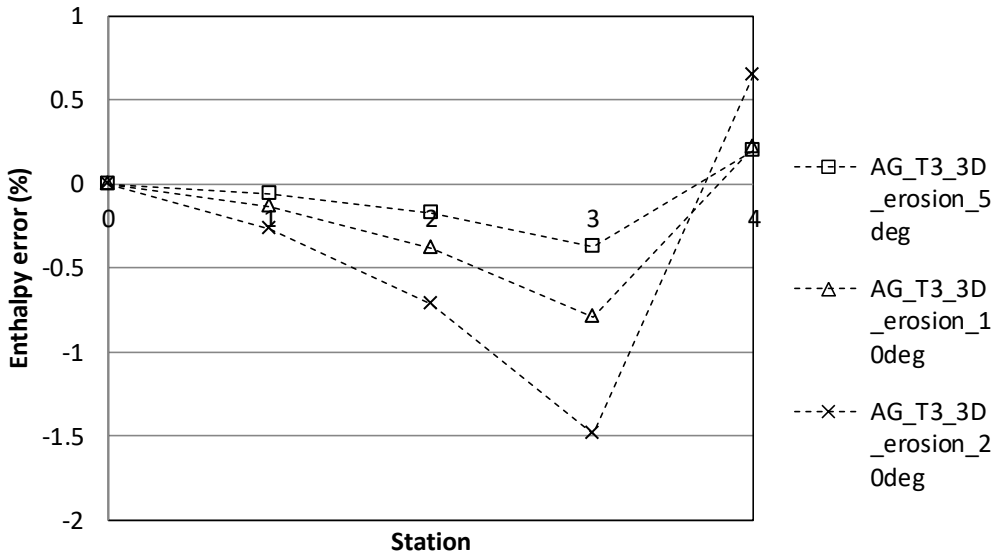

Figure 65. A comparison of total enthalpy between the test case data and calculated results at nominal condition and the calculated results for the turbine modelled with blade erosion.

Figure 65 shows that the enthalpy drop across the final stage with erosion is slightly less than the enthalpy drop across a normal stage resulting in a higher enthalpy condition at the exhaust of the turbine. Simulating localised blade erosion with this level of detail would typically require CFD. However a CFD calculation would require a complete remodelling of the eroded blade geometry and a new mesh would have to be generated for this condition.

6.1.4 Cropped rotor stage

When a turbine blade row has been damaged due to normal wear or an incident, it is often not safe to operate the machine with the blades in the damaged condition. If spare blades are not available immediately it may be justified to remove the damaged blade row completely and return the machine to service while a new set of blades are being manufactured. Figure 66 shows an example of a turbine stage with missing blades that could be temporarily repaired by cropping or cutting off the remaining blades in that stage. In such a case the blades would be cut off at the root, keeping the root intact to protect the rotor disc head and root slots from erosion.

Figure 66. An example of a turbine blade row that has been damaged so severely that the turbine cannot be operated safely with the blades (Institue of noise and vibration, 2016).

The impact on the thermofluid process has to be evaluated to ensure that the remaining blade rows are not overloaded and operated beyond their design limits. Overloading turbine blades could lead to catastrophic failure in a short time span. In order to evaluate the impact of

removing a rotor blade row, a simulation was performed with rotor stage 2 blades removed and the results compared with the simulation results for the nominal condition.

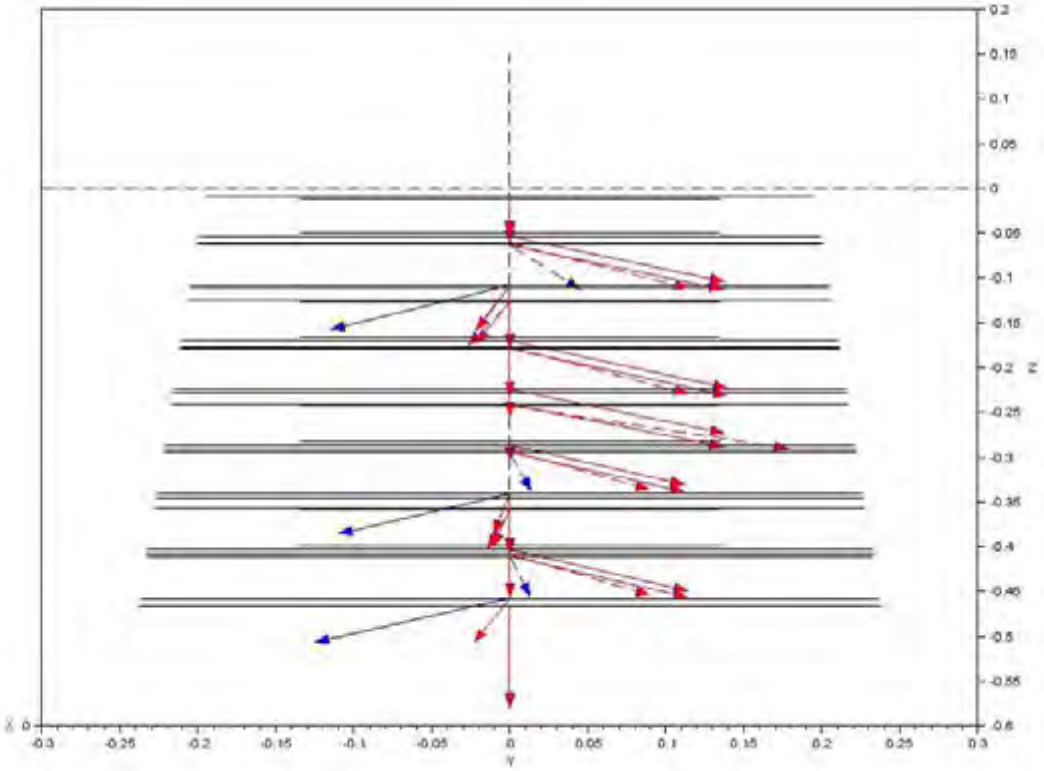

Figure 67. A front view of the simulation model with the stage 2 rotor blades removed.

When comparing Figure 67 with the Figure 44 of the nominal condition, one can see the impact of removing a rotor blade row in the region of stage 2. The absolute velocity vectors exiting the stage 2 stator are maintained through the area where the rotor blades were removed and enter the stage 3 stator with a large tangential velocity component.

The data in

Table 14 shows that the efficiency is also severely affected. When the engineer does the technical justification for cropping the blades, he needs to take into account the impact on efficiency and the additional cost to produce the power.

Table 14. Description and results of off-design cases of turbine with a blade row removed.

Case name	Description	Rotor work (kW)	Efficiency	Mass flow rate (kg/s)
AG_T3_3D	Modelled case data of the nominal condition	717.524	0.900	8.339
AG_T3_3D_missing row_nominal pressure drop	Modelled case data of the modelled turbine with stage 2 rotor blade row removed. Nominal pressure drop is applied.	771.148	0.849	9.398
AG_T3_3D_ missing row reduced pressure drop	Modelled case data of the modelled turbine with stage 2 rotor blade row removed. Reduced pressure drop is applied to match design mass flow rate.	580.795	0.864	8.367
AG_T3_3D_ missing row reduced power	Modelled case data of the modelled turbine with stage 2 rotor blade row removed. Reduced pressure drop is applied to prevent overloading of stages.	450.894	0.862	7.367

As stage 2 now lacks a pressure drop due to no work done in the rotor, the pressure distribution in the remaining stages is also affected. In

Table 15 one can see that the redistribution of the pressure drops and thus power and torque across the remaining stages is not proportionally shared by the remaining stages. The stage 1 torque increases by a substantially larger value than the torque developed by stage 3 and 4. Thus stage 1 rotor blades have a higher risk of being overloaded in this case.

Table 15. Power and torque results of off-design cases of turbine with a blade row removed.

Case name	Rotor stage 1 work (kW)	Rotor stage 3 work (kW)	Rotor stage 4 work (kW)	Rotor stage 1 torque (N.m)	Rotor stage 3 torque (N.m)	Rotor stage 4 torque (N.m)
AG_T3_1D	183.254	174.004	186.051	233.326	221.549	236.888
AG_T3_3D_missing row nominal mass flow rate	277.777	229.227	264.144	353.677	291.861	336.318
AG_T3_3D_ missing row reduced mass flow rate	224.563	172.333	183.899	285.923	219.421	234.147
AG_T3_3D_ missing row reduced power	184.852	133.071	132.972	235.361	169.431	169.305

In the first case no other parameters were changed and the pressure drop across the turbine was maintained at the nominal parameters. The result was an increase in mass flow rate of 12%. This already highlights the risk that the remaining blade rows may be overloaded. Furthermore the torque developed in the remaining blade rows can be obtained from the net change in specific angular momentum and the mass flow rate. An increase in torque of a maximum of 51% is observed in the first stage rotor. The engineer should adjust the pressure ratio in the simulation until a value is obtained that would result in a safe operating regime. In the second case the pressure ratio was reduced and the results show that the torque and power developed in stage 3 and 4 compare well with the nominal condition. However the model shows that stage 1 is still loaded excessively. A further reduction in pressure ratio would be required to ensure safe operation of the machine.

A further indication of risk is the changes in temperature distribution that is noted in Figure 68. Incorrect temperature distributions in the turbine could lead to warping of the casings or incorrect expansion of the rotor that may result in interference of the turbine internal parts.

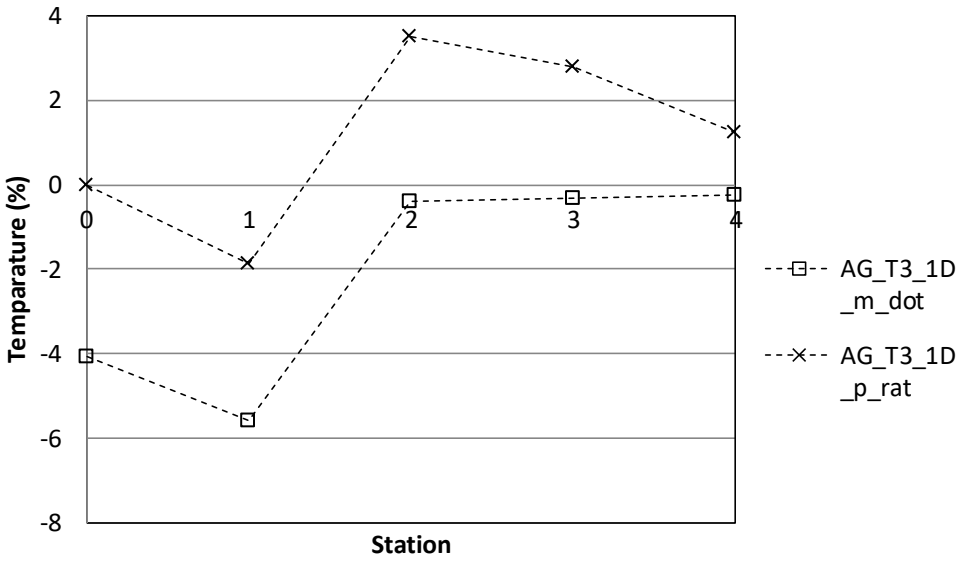

Figure 68. A comparison of total temperature between the test case data and calculated results at nominal condition and the calculated results for the turbine modelled with a missing blade row.

This experiment only required changes to the element representing the second stage rotor. The other elements in the model were left unchanged, illustrating how flexible this modelling approach is.

6.1.5 Blockage of turbine passages

Blockage of the flow through a turbine can occur when industrial steam turbine plant is operated with poor steam cleanliness parameters. A high mineral content in the fluid leads to a build-up of scale on the turbine internal surfaces. The result is that the cross sectional flow areas of these components are effectively reduced.

Figure 69. Scale formation on a turbine stator (Mitsubishi Heavy Industires, 2012).

Four cases were investigated. In the first, all cross-sectional flow areas in the turbine were reduced by 5% to simulate the reduction in flow area caused by scale formation in the blade passages. The result is a reduction in the calculated mass flow rate of 5.4%. The power developed is reduced by 5.9%.

The second, third and fourth cases involved reducing the area of individual stages in the turbine, namely stage one, two and three, respectively. In all three cases the stage area is reduced by 10%.

Table 16. Results of a simulation of scale build-up in turbine stages.

	Nominal	**Case 2**	**Case 3**	**Case 4**
Rotor work (kW)	717.524	684.121	694.699	700.769
Efficiency	0.900	0.899	0.900	0.900
Mass flow rate kg/s	8.339	7.977	8.085	8.153

The data in Table 16 shows that the simulated scaling has a severe impact on the power produced and the mass flow rate through the turbine. If an engineer finds that his turbine has a reduced consumption, scaling could be investigated as a possible cause.

Table 17. Power produced per stage of a simulation of scale build-up in turbine stages.

Stage	**Nominal power (kW)**	**%difference case 2**	**%difference case 3**	**%difference case 4**
1	183.254	10.67	-10.12	-7.48
2	174.215	-8.17	13.28	-9.80
3	174.004	-9.60	-6.78	14.67
4	186.051	-11.83	-8.40	-6.18

The power produced by the complete turbine may be reduced, however due to the incorrect pressure distribution caused by local scaling of a specific blade row the power produced by that row could be severely increased. Table 17 shows that for an area reduced by 10%, the power could increase up to 14.7%. This highlights a risk of overloading the blades which could lead to a catastrophic blade failure.

Table 18. Pressure drop per stage of a simulation of scale build-up in turbine stages.

Stage	Nominal pressure drop (kPa)	%difference case 2	%difference case 3	%difference case 4
1 stator	-30.940.42	-6.04	-8.18	18.58
1 rotor	-17.492.63	-4.31	-5.86	18.69
2 stator	-23.099	-6.21	21.58	-7.59
2 rotor	-16.216	-6.05	21.05	-6.15
3 stator	-18.080	22.41	-6.26	-6.95
3 rotor	-15.268	23.06	-5.14	-7.29
4 stator	-14.896	-5.64	-5.59	-7.93
4 rotor	-15.042	-4.79	-6.51	-9.21

In

Table 18, a comparison is given of the pressure drop under nominal conditions and the pressure drop in the simulated scaled condition. The data shows that the scaling can lead to a severe increase in the pressure drop in the affected stator and rotor rows. Increased pressure drop places undue stress on the stator diaphragm which typically has a large surface area exposed to the pressure difference. The increased pressure of the stator diaphragm may lead to distortion of this component. In severe cases distortion may cause contact of the stator and rotor in service. Distortion of the diaphragm also affects the effectivity of the stator shaft seal.

6.2 Chapter summary

In this chapter off-design conditions were simulated with the model. The anomalies that often occur in industrial turbines were applied to the test case to demonstrate how the model can be used to investigate the effect of these anomalies and how the plant engineer can use the data to diagnose potential problems. The anomalies investigated were leakage of turbine internal seals, turbine blade erosion, cropped rotor stages and scaling of the turbine passages.

The results show interesting findings that would be difficult to obtain by means of hand calculations. The exercise also illustrated that once the model has been established and calibrated for the nominal case, affecting changes to simulate off-design conditions is fairly simple and could easily be applied in an industrial setting. Such a model could therefore be used by the plant engineer to investigate suspected problems and assist him to make findings in the day-to-day maintenance and monitoring of his plant.

Chapter 7. Conclusions and recommendations for further work

7.1 Conclusions

This thesis followed a process of investigation of background knowledge, implementation, application and drawing results.

- In the literature study a range of approaches were investigated ranging from 1D simplified calculations to 3D CFD. Based on the literature it was apparent that a 1D approach is indeed a suitable methodology to achieve the objective of developing a model that can provide sufficient detail for engineering investigations while maintaining a level of simplicity. Leonid, et al (2005) illustrated that the time invested in 3D CFD is several orders of magnitude larger than 1D analysis. A CFD model of a single turbine stage developed by Gardzilewicz, et al (2003) required 2 million finite volumes. The present model of a four stage turbine required up to 55 flow elements and could be solved on a personal computer in under one minute. Once the software program was developed, various simulations could be performed on the test case with little resources required.
- Several of the commonly applied loss calculation methods were investigated. The method proposed by Benner, et al. (2006) was applied, as it is the most recent in a series of revision and improvements to the loss models originally developed by Ainley and Mathieson (1951) that have been performed over more than half a century. The method was developed based on a broad range of data obtained from test cases and industrial turbines, ensuring a broad applicability. Additional losses not directly addressed by Benner, et al. were obtained from other authors and implemented.
- Starting at the basic principles and applying the fundamental conservation equations to the stationary and rotating flow passages, a methodology was developed to solve the conservation equations as applied to a turbine consisting of a thermofluid network. The methodology was implemented in Scilab through

a pressure correction scheme and an energy balance calculation and the equations closed by applying loss models to determine the pressure losses in each of the discrete turbine control volumes. The program performed well and could be solved in most cases. It was found that the solution can be assisted by applying relaxation to the pressure correction and/or the mass flow rate calculation.

- A test case obtained in the literature was used to validate the model. The test case consisted of measurement data and geometric data of a real turbine setup in a laboratory. Seven cases were modelled, consisting of a nominal case and six off-design cases with varying degrees of specific speed and pressure ratio. The present model could be successfully applied to this real turbine in a practical manner.
- In applying the newly developed model it was found that the loss models that have been selected slightly underestimate the losses of this test case. This results in calculated efficiencies that are approximately 4% too high through the range of tests and higher at severe off design conditions. Several authors noted in their works that there can be significant differences between the losses measured and those predicted by the loss models. The observations ranged from under predicted to over predicted losses. This provided a basis for calibrating the models to suit the specific turbine. In the present work, the model could be suitably calibrated for a broad range of relative mass flow rates by adjusting the only the incidence loss factor.
- Three models with varying discretisation schemes were tested. In the first model, each of the stator and rotor passages were modelled by a single control volume. In the second and third models the stator and rotor passages were discretised into three and five radial elements respectively. All three models used discrete elements to model the flow through the stator and rotor sealing passages.
- In general the three models appear to predict the test case efficiency well at nominal conditions. This is expected as the models were calibrated for the nominal case. The models predict the efficiency well for a range of relative mass flow rates around the nominal condition and clearly capture the effects of off-design operation. This required some adjustment of the losses associated with

off-design conditions in order to capture the magnitude of these losses in the test case. As expected, it was found that the prediction becomes less accurate at severe off-design operation.

- Using a model with more discrete elements along the radial blade length does not result in a more accurate estimation of the turbine overall efficiency for this model, however there is a slight improvement in the prediction of losses at severe off-design conditions. This effect would possibly be more pronounced for turbines with large aspect ratio blades.
- Several hypothetical off-design conditions were simulated with the model. Some anomalies that often occur in industrial turbines were applied to the test case to demonstrate how the model can be used to investigate the effect of these anomalies and how the plant engineer can use the data to diagnose potential problems. The anomalies investigated were leakage of turbine internal seals, turbine blade erosion, cropped rotor stages and scaling of the turbine passages. It was found that the model is well suited to exploratory aspects of simulation as the model could be easily adjusted to simulate the impact of specific anomalies on the overall network. Detailed process parameters could be extracted at each element representing specific points in the turbine. The results of the investigated anomalies show interesting findings of flow parameters within the stages that would be difficult to obtain by means of hand calculations. The exercise also illustrated that once the model has been established and calibrated for the nominal case, affecting changes to simulate off-design conditions is fairly simple.

With further development of the user interface the present approach could be applied in an industrial setting to obtain detailed turbine process parameters on a row-by-row basis. The model can be used to simulate various anomalies that would otherwise require cumbersome hand calculations or enlisting the expertise of a CFD specialist. Such a model could therefore be used by the engineer to investigate suspected problems and assist him to make findings in the day-to-day maintenance and monitoring of his plant.

7.2 Future work

This study formed part of the work done by the Energy Efficiency research group at the University of Cape Town. One of the goals of this research group is to develop process models for improved monitoring and diagnostics of thermal power plants in South Africa. Much of the work done by this group is based on thermofluid network analysis of the water-steam cycle of these plants. The present work is focussed on the turbine as a component of such a water-steam cycle, but not limited to it. To continue this work it is suggested that:

- The developed methodology must be applied to an industrial turbine. This would pose some unique challenges. Most notably with regards to getting access to geometric input data of such a turbine. Detailed drawings of industrial machines are normally not accessible as the intellectual property is protected by the OEM. Thus it will be necessary to take measurements from a machine that is on outage. However, this activity will require careful planning to synchronise the research with a planned outage and a significant support will be required from the plant owner to provide access to the researcher to perform the required measurements.
- Integration of a thermofluid network of a turbine into a model of a complete steam or gas cycle or parts of the auxiliary steam plant. Such an investigation could consider the effect on the turbine internal flows when the operation of the auxiliary steam plant is altered.
- The implementation of the 1D rotating control volume in a network approach should allow for the implementation of two-phase flow. Tested software packages such as Flownex Simulation Environment have powerful solvers that are capable of solving the fundamental conservation equations for two phase flows in pipe networks. It would be interesting to extend this to the application of a steam turbine by applying appropriate loss models for two-phase flow and following a similar approach as the present method.
- The implementation of the labyrinth seal model can be improved by incorporating the effect that rotational friction has on the angular momentum within the seal. This would require that the node absolute pressure is converted to static pressure upstream and downstream of an element before solving the momentum equation.

References

Ainley, D. & Mathieson, G., 1951. A Method of performance estimation of axial flow turbines.

Albert, P., 2000. *Steam turbine thermal evaluation and assessment,* Schenectady, NY: GE Power Systems.

Almasi, A., 2011. *Plant Services-Perform system maintenance to slow degradation of rotating equipment.* [Online]
Available at: http://www.plantservices.com/articles/2011/09-maintenance-slows-degradation-rotating-equipment/
[Accessed 4 12 2016].

Anon., 2015. *Ansys.* [Online]
Available at: http://www.ansys.com/staticassets/ANSYS/staticassets/event/
[Accessed 4 12 2015].

Anon., 2015. *GrabCad - How to model a turbine rotor in solid works.* [Online]
Available at: https://grabcad.com/questions/how-to-model-turbine-rotor-in-solidworks
[Accessed 12 08 2015].

Axel, P., 2003. *Loss mechanisms in labyrinth seals of shrouded axial turbines.* Zurich: Swiss Institute of Technology.

Beebe, R., 2003. Condition monitoring of steam turbines by performance analysis. *Journal of quality in maintanance engineering,* 9(2), pp. 102-112.

Benner, M., Sjolander, S. & Moustapha, S., 1997. Measurements of secondary flows in a turbine cascade at off-design incidence. *ASME paper no 97-GT-382.*

Benner, M., Sjolander, S. & Moustapha, S., 2004. The influence of leading-edge geometry on secondary losses in a turbine cascade at the design incidence. *Journal of turbomachinery,* Volume 126, pp. 277-287.

Benner, M., Sjolander, S. & Moustapha, S., 2006. An emperical prediction method for secondary losses in turbines - Part 1: A new loss breakdown scheme and penetration depth correlation. *Journal of turbomachinery,* Volume 128, pp. 273-280.

Benner, M., Sjolander, S. & Moustapha, S., 2006. An empirical prediction method for secondary losses in turbines - Part 2: A new secondary loss correlation. *Journal of turbomachinery,* Volume 128, pp. 281-291.

Benner, M. W., Sjolander, S. A. & Moustapha, S. H., 2006. An empirical prediction method for secondary losses in turbines-Part II: A new secondary loss correlation. *Journal of turbomachinery,* Volume 128, pp. 281-291.

Buckingam, E., 1911. The steam turbine expansion line on the Mollier diagram and a short method of finding the reheat factor. *Bulletin of the Bureau of Standards,* 7(4).

Chaibakhsh, A. & Ghaffari, A., 2008. Steam turbine model. *Simulation and modelling practice and theory,* 16(9), pp. 1145-1162.

Church, E., 1950. *Steam turbines.* 3rd ed. New York: Mcgraw-hill bokk company, inc.

Cooke, D., 1983. Modelling of off design multistage turbine pressures by stodolas elipse.

Cooke, D., 1983. *Modelling of off-design multistage turbine pressures by Stodola's ellipse.* Richmond, Bechtel Power Corporation.

Craig, H. & Cox, H., 1970. *Performance estimation of axial flow turbines.* s.l., Instititution of mechanical engineers.

Craig, H. & Cox, H., 1970. *Performance estimation of axial flow turbines.* s.l., Institute of mechanical engineers.

Dahlquist, A., 2008. *Investigation of losses prediction methods in 1D for axial gas turbines,* Lund: Lund University.

Daniel, D., 2014. *Cation conductivity monitoring: a reality check.* [Online]
Available at: http://www.powermag.com/cation-conductivity-monitoring-a-reality-check/?pagenum=2
[Accessed 23 3 2015].

Denton, J., 1993. Loss mechanisms in turbomachines. *Journal of turbomachinery,* Volume 115.

Denton, J., 1998. Computational fluid dynamics for turbomachinery design.

Denton, J. D., 1993. Loss mechanisms in turbomachines. *Journal of turbomachinery,* Volume 115.

Denton, J. & Dawes, W., 1998. Computational fluid dynamics for turbomachine design. *Proceedings of the institution of mechanical engineers, part C: Journal of mechanical engineering science,* 213(2), pp. 107-124.

Dixon, S., 2005. *Fluid mechanics and thermodynamics of turbomachinery.* 5th ed. Burlington: Elsevier Butterworth-Heinemann.

Dunham, J. & Came, P., 1970. Improvements to the Ainley-Mathieson method of turbine performance prediction. *Journal of engineering for power,* 92(3), pp. 252-256.

Flownex, 2013. *Flownex theory manual,* s.l.: Flownex.

Fottner, L., 1990. *Test cases for computation of internal flows in aero engine components.* Essex: AGARD.

Fottner, L., 1990. *Test cases for computation of internal flows in aero engine components.* Essex: AGARD.

Gardzilewicz, A. et al., 2003. Methodology of CFD computations applied for analysing flows through turbine exhaust hood. *Transactions of the institute of fluid-flow machinery,* Volume 113, pp. 157-168.

Gill, A., 1984. *Power plant performance.* 1st ed. London: Butterwirth and Co (publishers), Ltd.

Greyvenstein, G. & Laurie, D., 1994. A segregated CFD approach to pipe network analysis. *International journal for numerical methods in engineering,* Volume 37, pp. 3685-3705.

Institue of noise and vibration, 2016. *Technical capabilities.* [Online]
Available at: http://inv.com.my/about-inv/technical-capabilities/
[Accessed 4 12 2016].

Joubert, L., 2003. *Mathematical modelling of leakage flows through labyrunth seals.* Pothcefstroom: Potchefstroom University for Christian Higher Eductaion.

Kacker, S. & Okapuu, U., 1982. A mean line prediction method for axial flow turbine efficiency. *Journal for engineering for power,* Volume 104, pp. 111-119.

Leonard, O. & Adam, O., 2008. A quasi-one-dimensional CFD model for multistage turbomachines. *Journal of thermal science,* 17(1), pp. 7-20.

Leonard, O. & Adam, O., 2008. A quasi-one-dimensional CFD model for multistage turbomachines. *Journal of thermal science,* 17(1), pp. 7-20.

Leonid, M., Govoruschenko, Y. & Pagur, P., 2005. *Axial turbine stages design: 1D/2D/3D simulation, experiment, optimization.* Reno-Tahoe, ASME.

MAN Turbomachinery, 2016. *Steam turbines.* [Online]
Available at: http://turbomachinery.man.eu/products/steam-turbines
[Accessed 12 03 2016].

Martínez, A. et al., 2012. The Density and Momentum Distributions of 2-Dimensional Transonic Flow in an LP-Steam Turbine. *Energy and Power Engineering,* 4(5), p. 7.

Mazur, Z., Garcia-Illescas, R. & Aquirre-Romano, J., 2008. Steam turbine blade failure analysis. *Engineering failure analysis,* 15(1-2), pp. 129-141.

Mazur, Z., Urguiza, G., Sierra, F. & Campos, R., 2002. Numerical analysis of erosion of the rotor labyrinth seal in a geothermal turbine. *Geothermics,* Volume 31, pp. 563-577.

Mitsubishi Heavy Industires, 2012. *Read the future no. 166.* [Online]
Available at: http://www.mhi-global.com/discover/graph/feature/no166.html
[Accessed 10 03 2016].

Moustapha, S., Kacker, S. & Tremblay, B., 1990. An improved incidence losses prediction method for turbine airfoils. *Journal of turbomachinery,* Volume 112.

Nair, L., 2015. *Steam turbine model.* [Online]
Available at: http://www.academia.edu/4993757/Steam_turbine_model
[Accessed 4 12 2015].

Ning, W., 2000. *Significance of Loss Models in aerodynamic simulation for axial turbines,* Stockholm: Royal institute of technology.

Pottas, R., Rousseau, P. & De Klerk, G., 2015. *Development of a row-by-row process model of a steam turbine.* Johannesburg, Eskom Power Plant Engineering Institute.

Rousseau, P., 2013. *Thermal-fluid systems modelling 1 course notes.* Potchefstroom: North-West University.

Rousseau, P., 2013. *Thermal-fluid systems modelling 1 course notes.* Potchefstroom: North-West University.

Sanders, W., 1996. *Turbine steam path engineering for operations and maintanance staff.* 1st ed. Ontario: Turbo-Technic Services, Incorporated.

Siemens, 2016. *Siemens Steam Turbine SST-800.* [Online]
Available at: http://www.energy.siemens.com/co/en/fossil-power-generation/steam-turbines/sst-800.htm
[Accessed 30 06 2016].

Slawomir, D., Wlodzimierz, W. & Henryk, L., 2007. Prediction of losses in the flow through the last stage of low -pressure steam turbine. *International journal for numerical methods in fluids,* Volume 53, pp. 933-945.

Soderberg, C. R., 1949. *Unpublished notes, Gas turbine laboratory, Massachusetts Institute of Technology (qouted in reference [Dixon, 2005]).* s.l.:s.n.

Spencer, R., Cotton, K. & Cannon, C., 1963. A method for predicting the performance of steam turbine generators 16500kW and larger. *Journal for engineering for power,* pp. 249-298.

White, F., 2003. *Fluid Mechanics.* New York: McGraw-Hill.

Zill, D. & Cullen, M., 2006. *Andvanced engineering mathematics.* 3rd ed. London: Jones and Bartlett Publishers, Inc..

Zimmer, G., 2008. Modelling and simulation of steam turbine processes: individual models for individual tasks. *Mathematical and computer modelling of dynamical systems,* 12(6), pp. 469-493.

Appendix A Pressure loss relation for compressible flow

Some of the other losses that the model needs to deal with are defined at the entrance of the fluid element or by the average velocity across the element. Examples are the losses caused by cavities and D'arcy friction losses respectively.

$$\Delta p_{0,loss} = Y_{loss,i}\left(p_{0,i} - p_i\right) + Y_{loss,avg}\left(p_{0,avg} - p_{avg}\right) + Y_{loss,e}\left(p_{0,e} - p_e\right) \tag{4.19}$$

From the definition of total pressure it is possible to write this equation in terms of the relative Mach numbers:

$$\begin{aligned}\Delta p_{0,loss} = {} & Y_{loss,in} p_{in}\left(\left(1+\frac{\gamma-1}{2}M_{\text{in},rel}^2\right)^{\frac{\gamma}{\gamma-1}} - 1\right) + \\ & Y_{loss,agv} p_{avg}\left(\left(1+\frac{\gamma-1}{2}M_{\text{avg},rel}^2\right)^{\frac{\gamma}{\gamma-1}} - 1\right) + Y_{loss,\text{out}} p_{out}\left(\left(1+\frac{\gamma-1}{2}M_{\text{out},rel}^2\right)^{\frac{\gamma}{\gamma-1}} - 1\right)\end{aligned} \tag{4.19}$$

The equation is rearranged and write the Mach number in terms of the relative velocity:

$$\begin{aligned}= {} & Y_{loss,\text{in}} p_{in}\left(\frac{1+\frac{\gamma-1}{2}\frac{v_{in}^2}{\gamma RT}}{\left(1+\frac{\gamma-1}{2}M_{\text{in},rel}^2\right)^{1-\frac{\gamma}{\gamma-1}}} - 1\right) + \\ & Y_{loss,avg} p_{avg}\left(\frac{1+\frac{\gamma-1}{2}\frac{v_{avg}^2}{\gamma RT}}{\left(1+\frac{\gamma-1}{2}M_{\text{avg},rel}^2\right)^{1-\frac{\gamma}{\gamma-1}}} - 1\right) + \\ & Y_{loss,\text{out}} p_{out}\left(\frac{1+\frac{\gamma-1}{2}\frac{v_{out}^2}{\gamma RT}}{\left(1+\frac{\gamma-1}{2}M_{\text{out},rel}^2\right)^{1-\frac{\gamma}{\gamma-1}}} - 1\right)\end{aligned} \tag{4.20}$$

Substitute the relative velocity with mass flow rate from the definition of mass flow rate:

$$= Y_{loss,in} p_{in} \left(\frac{1 + \left(\frac{\gamma - 1}{2} \right) \left(\frac{\dot{m}^2}{\rho_{in}^2 A_{in}^2 (\hat{n}.\hat{o})^2 \gamma R T_{in}} \right)}{\left(1 + \frac{\gamma - 1}{2} M_{\text{in},rel}^2 \right)^{1 - \frac{\gamma}{\gamma - 1}}} - 1 \right) +$$

$$Y_{loss,avg} p_{avg} \left(\frac{1 + \left(\frac{\gamma - 1}{2} \right) \left(\frac{\dot{m}^2}{\rho_{avg}^2 A_{avg}^2 (\hat{n}.\hat{o})^2 \gamma R T_{avg}} \right)}{\left(1 + \frac{\gamma - 1}{2} M_{\text{avg},rel}^2 \right)^{1 - \frac{\gamma}{\gamma - 1}}} - 1 \right) + \tag{4.21}$$

$$Y_{loss,\text{out}} p_{out} \left(\frac{1 + \left(\frac{\gamma - 1}{2} \right) \left(\frac{\dot{m}^2}{\rho_{out}^2 A_{out}^2 (\hat{n}.\hat{o})^2 \gamma R T} \right)}{\left(1 + \frac{\gamma - 1}{2} M_{\text{out},rel}^2 \right)^{1 - \frac{\gamma}{\gamma - 1}}} - 1 \right)$$

Where $\hat{n}$ and $\hat{o}$ are the unit area vector and unit vector of relative velocity, respectively. Next, we can divide out the mass flow rate:

$$\Delta p_{0L} = \dot{m}^2 \left[\begin{array}{l} Y_{loss,in} p_{in} \left(\frac{\frac{1}{\dot{m}^2} + \left(\frac{\gamma - 1}{2} \right) \left(\frac{1}{\rho_{in}^2 A_{in}^2 (\hat{n}.\hat{o})^2 \gamma R T_i} \right)}{\left(1 + \frac{\gamma - 1}{2} M_{\text{in},rel}^2 \right)^{1 - \frac{\gamma}{\gamma - 1}}} - \frac{1}{\dot{m}^2} \right) + \\ Y_{loss,avg} p_{avg} \left(\frac{\frac{1}{\dot{m}^2} + \left(\frac{\gamma - 1}{2} \right) \left(\frac{1}{\rho_{avg}^2 A_{avg}^2 (\hat{n}.\hat{o})^2 \gamma R T_{avg}} \right)}{\left(1 + \frac{\gamma - 1}{2} M_{\text{avg},rel}^2 \right)^{1 - \frac{\gamma}{\gamma - 1}}} - \frac{1}{\dot{m}^2} \right) + \\ Y_{loss,\text{out}} p_{out} \left(\frac{\frac{1}{\dot{m}^2} + \left(\frac{\gamma - 1}{2} \right) \left(\frac{1}{\rho_{out}^2 A_{out}^2 (\hat{n}.\hat{o})^2 \gamma R T} \right)}{\left(1 + \frac{\gamma - 1}{2} M_{\text{out},rel}^2 \right)^{1 - \frac{\gamma}{\gamma - 1}}} - \frac{1}{\dot{m}^2} \right) \end{array} \right] \tag{4.22}$$

The average values of area and density are defined in terms of the average velocity and mass flow rates so for the average value:

$$\Delta p_{0L} = \dot{m}^2 \left[\begin{array}{l} Y_{loss,in} p_{in} \left(\dfrac{\dfrac{1}{\dot{m}^2} + \left(\dfrac{\gamma - 1}{2} \right) \left(\dfrac{1}{\rho_{in}^2 A_{in}^2 (\hat{n}.\hat{o})^2 \gamma R T_{in}} \right)}{\left(1 + \dfrac{\gamma - 1}{2} M_{\text{in},rel}^2 \right)^{1 - \frac{\gamma}{\gamma - 1}}} - \dfrac{1}{\dot{m}^2} \right) + \\ Y_{loss,avg} p_{avg} \left(\dfrac{\dfrac{1}{\dot{m}^2} + \left(\dfrac{\gamma - 1}{2} \right) \left(\dfrac{v^2}{\dot{m}^2 \gamma R T_{avg}} \right)}{\left(1 + \dfrac{\gamma - 1}{2} M_{\text{avg},rel}^2 \right)^{1 - \frac{\gamma}{\gamma - 1}}} - \dfrac{1}{\dot{m}^2} \right) + \\ Y_{loss,\text{out}} p_{out} \left(\dfrac{\dfrac{1}{\dot{m}^2} + \left(\dfrac{\gamma - 1}{2} \right) \left(\dfrac{1}{\rho_{out}^2 A_{out}^2 (\hat{n}.\hat{o})^2 \gamma R T} \right)}{\left(1 + \dfrac{\gamma - 1}{2} M_{\text{out},rel}^2 \right)^{1 - \frac{\gamma}{\gamma - 1}}} - \dfrac{1}{\dot{m}^2} \right) \end{array} \right] \tag{4.23}$$

From the conservation of momentum for rotating elements, we can write for pressure losses:

$$\Delta p_{0,L} = -\frac{p_{avg}}{p_{0avg}} \left(p_{0,\text{out}} - p_{0,in} \right) - \frac{1}{2} \rho_{avg} C_{avg}^2 \frac{1}{T_{0avg}} \left(T_{0,out} - T_{0,in} \right) - \rho_{avg} g \left(z_{out} - z_{in} \right) + \rho_{avg} \omega X \tag{4.23}$$

substitute (4.23) into (4.23) to obtain a function of the form $\dot{m} = f\left(p_{0,in}, p_{0,\text{out}} \right)$:

$$\dot{m} = \frac{-\frac{p_{avg}}{p_{0avg}}\left(p_{0,\text{out}} - p_{0,in}\right) - \frac{1}{2}\rho_{avg}C_{avg}^2\frac{1}{T_{0avg}}\left(T_{0,out} - T_{0,in}\right) - \rho_{avg}g\left(z_{out} - z_{in}\right) + \rho_{avg}\omega X}{\left|\dot{m}\right|\left[\begin{array}{l} Y_{loss,in}p_{in}\left(\frac{\frac{1}{\dot{m}^2} + \left(\frac{\gamma-1}{2}\right)\left(\frac{1}{\rho_{in}^2 A_{in}^2(\hat{n}.\hat{o})^2\gamma RT_{in}}\right)}{\left(1+\frac{\gamma-1}{2}M_{\text{in},rel}^2\right)^{1-\frac{\gamma}{\gamma-1}}} - \frac{1}{\dot{m}^2}\right) + \\ Y_{loss,avg}p_{avg}\left(\frac{\frac{1}{\dot{m}^2} + \left(\frac{\gamma-1}{2}\right)\left(\frac{v^2}{\dot{m}^2\gamma RT_{avg}}\right)}{\left(1+\frac{\gamma-1}{2}M_{\text{avg},rel}^2\right)^{1-\frac{\gamma}{\gamma-1}}} - \frac{1}{\dot{m}^2}\right) + \\ Y_{loss,\text{out}}p_{out}\left(\frac{\frac{1}{\dot{m}^2} + \left(\frac{\gamma-1}{2}\right)\left(\frac{1}{\rho_{out}^2 A_{out}^2(\hat{n}.\hat{o})^2\gamma RT}\right)}{\left(1+\frac{\gamma-1}{2}M_{\text{out},rel}^2\right)^{1-\frac{\gamma}{\gamma-1}}} - \frac{1}{\dot{m}^2}\right) \end{array}\right]} \tag{4.24}$$

We separate the terms containing p_0 which will be solved for from the rest of the terms which are calculated and updated after each iteration.

$$\dot{m} = coeffs.\left(p_{0,\text{out}} - p_{0,in}\right) + consts \tag{4.24}$$

where

$$coeffs = \frac{-\frac{p_{avg}}{p_{0,avg}}}{\left|\dot{m}\right|\left[\begin{array}{l} Y_{loss,in}p_{in}\left(\frac{\frac{1}{\dot{m}^2}+\left(\frac{\gamma-1}{2}\right)\left(\frac{1}{\rho_{in}^2A_{in}^2(\hat{n}.\hat{o})^2\gamma RT_i}\right)}{\left(1+\frac{\gamma-1}{2}M_{\text{in},rel}^2\right)^{1-\frac{\gamma}{\gamma-1}}}-\frac{1}{\dot{m}^2}\right)+ \\ Y_{loss,avg}p_{avg}\left(\frac{\frac{1}{\dot{m}^2}+\left(\frac{\gamma-1}{2}\right)\left(\frac{v^2}{\dot{m}^2\gamma RT_{avg}}\right)}{\left(1+\frac{\gamma-1}{2}M_{\text{avg},rel}^2\right)^{1-\frac{\gamma}{\gamma-1}}}-\frac{1}{\dot{m}^2}\right)+ \\ Y_{loss,\text{out}}p_{out}\left(\frac{\frac{1}{\dot{m}^2}+\left(\frac{\gamma-1}{2}\right)\left(\frac{1}{\rho_{out}^2A_{out}^2(\hat{n}.\hat{o})^2\gamma RT}\right)}{\left(1+\frac{\gamma-1}{2}M_{\text{out},rel}^2\right)^{1-\frac{\gamma}{\gamma-1}}}-\frac{1}{\dot{m}^2}\right) \end{array}\right]} \tag{4.24}$$

and

$$consts = \frac{-\frac{1}{2}\rho_{avg}C_{avg}^2\frac{1}{T_{0avg}}\left(T_{0,\text{out}}-T_{0,in}\right)-\rho_{avg}g\left(z_{out}-z_{in}\right)+\rho_{avg}\omega X}{\left|\dot{m}\right|\left[\begin{array}{l} Y_{loss,in}p_{in}\left(\frac{\frac{1}{\dot{m}^2}+\left(\frac{\gamma-1}{2}\right)\left(\frac{1}{\rho_{in}^2A_{in}^2(\hat{n}.\hat{o})^2\gamma RT_{in}}\right)}{\left(1+\frac{\gamma-1}{2}M_{\text{in},rel}^2\right)^{1-\frac{\gamma}{\gamma-1}}}-\frac{1}{\dot{m}^2}\right)+ \\ Y_{loss,avg}p_{avg}\left(\frac{\frac{1}{\dot{m}^2}+\left(\frac{\gamma-1}{2}\right)\left(\frac{v^2}{\dot{m}^2\gamma RT_{avg}}\right)}{\left(1+\frac{\gamma-1}{2}M_{\text{avg},rel}^2\right)^{1-\frac{\gamma}{\gamma-1}}}-\frac{1}{\dot{m}^2}\right)+ \\ Y_{loss,\text{out}}p_{out}\left(\frac{\frac{1}{\dot{m}^2}+\left(\frac{\gamma-1}{2}\right)\left(\frac{1}{\rho_{out}^2A_{out}^2(\hat{n}.\hat{o})^2\gamma RT}\right)}{\left(1+\frac{\gamma-1}{2}M_{\text{out},rel}^2\right)^{1-\frac{\gamma}{\gamma-1}}}-\frac{1}{\dot{m}^2}\right) \end{array}\right]} \tag{4.24}$$

Appendix B Labyrinth leakage loss

To model the leakage through the rotor shaft seals, the Saint Venant Wantzel model for a labyrinth seal is applied (Axel, 2003).

$$\dot{m} = C_{ke} C_d A_g \sqrt{\frac{2\gamma}{\gamma - 1} \frac{p_i^2}{RT_0} \left(\left(\frac{p_e}{p_i} \right)^{\frac{2}{\gamma}} - \left(\frac{p_e}{p_i} \right)^{\frac{\gamma+1}{\gamma}} \right)} \tag{4.25}$$

This model assumes that $\Delta p_0 = \Delta p_{0,loss}$ for a seal (no work done no heat transferred). Therefore the effect of rotational friction within the seal is not incorporated in equation (4.25), In the solver, the angular momentum is conserved between the inlet and the outlet of a labyrinth seal.

This equation can be rewritten for a case with multiple sealing strips. The equation must also be written in the form of a pressure loss coefficient so that it can be implemented in the model.

$$\dot{m} = C_{ke} C_d A_g \frac{p_{in}}{\sqrt{RT_0}} \sqrt{\frac{1 - \left(\frac{p_{out}}{p_{in}} \right)^2}{z - \frac{2}{\gamma} \ln \left(\frac{p_{out}}{p_{in}} \right)}} \tag{4.26}$$

$$\dot{m}^2 = \left(C_{ke} C_d A_g \right)^2 \frac{p_{in}^2}{RT_0} \frac{1 - \left(\frac{p_{out}}{p_{in}} \right)^2}{z - \frac{2}{\gamma} \ln \left(\frac{p_{out}}{p_{in}} \right)} \tag{4.27}$$

$$\dot{m}^2 = \left(C_{ke} C_d A_g \right)^2 \frac{\Delta p_0 \left(p_{in} + p_{out} \right)}{RT_0} \frac{}{z - \frac{2}{\gamma} \ln \left(\frac{p_{out}}{p_{in}} \right)} \tag{4.28}$$

$$\Delta p_0 = \frac{\dot{m}^2}{\left(C_{ke} C_d A_g\right)^2 \frac{\left(p_{in} + p_{out}\right)}{RT_0\left(z - \frac{2}{\gamma}\ln\left(\frac{p_{out}}{p_{in}}\right)\right)}}$$

From the definition of a total pressure loss we can therefore write:

$$Y_{seal} = \frac{\dot{m}^2}{\left(C_{ke} C_d A_g\right)^2 \frac{\left(p_{iin} + p_{out}\right)\left(p_{0,\text{out}} - p_{out}\right)}{RT_0\left(z - \frac{2}{\gamma}\ln\left(\frac{p_{out}}{p_{in}}\right)\right)}} \tag{4.29}$$

with z number of seal strips, the discharge coefficient, C_d, and the kinetic carry-over coefficient, C_{ke}, given by:

$$C_d = \frac{\pi}{\pi - 7\left(\frac{P_{in}}{P_{out}}\right)^{\frac{\gamma-1}{\gamma}} + \left(\frac{P_{in}}{P_{out}}\right)^{\frac{2\gamma-2}{\gamma}} + 8} \tag{4.30}$$

$$C_{ke} = \frac{1}{\sqrt{1 - \frac{8.52}{\frac{S-L}{cl} + 7.23}}} \tag{4.31}$$

Appendix C Full sized images of graphs

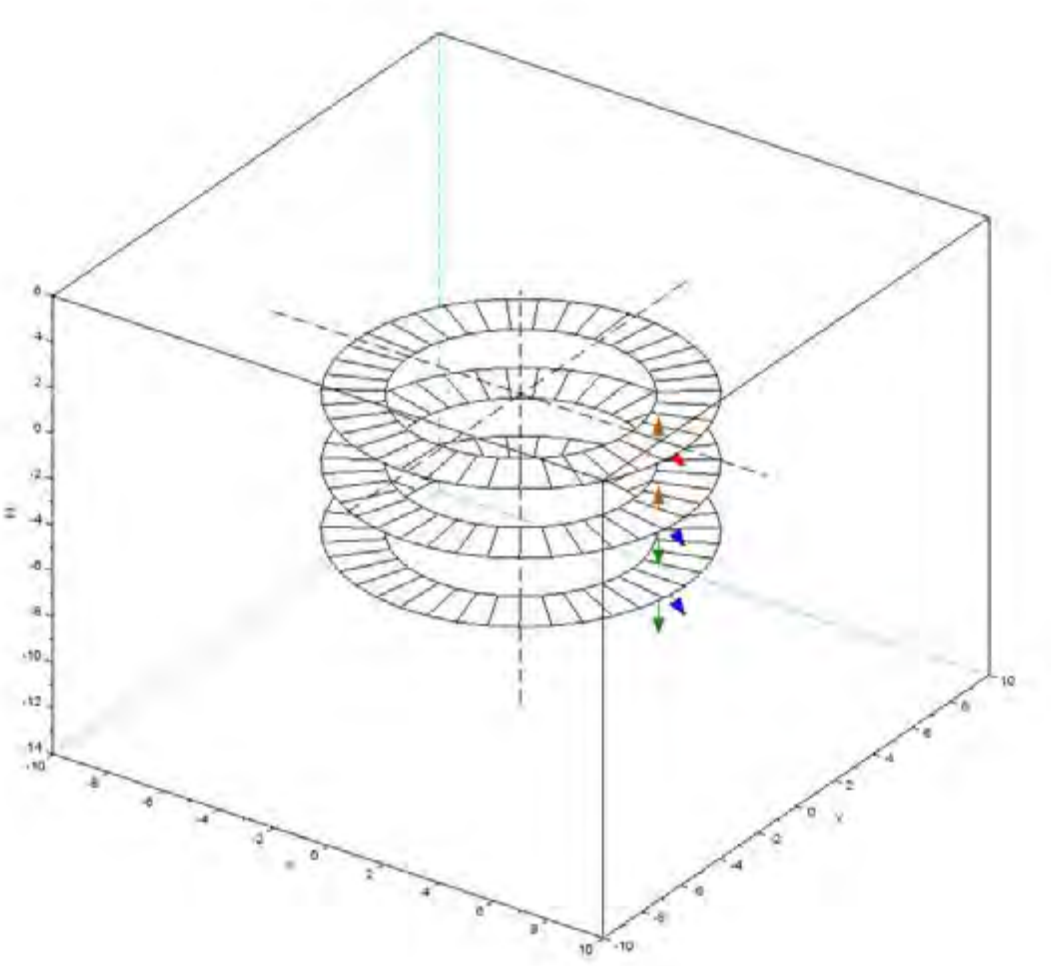

a.

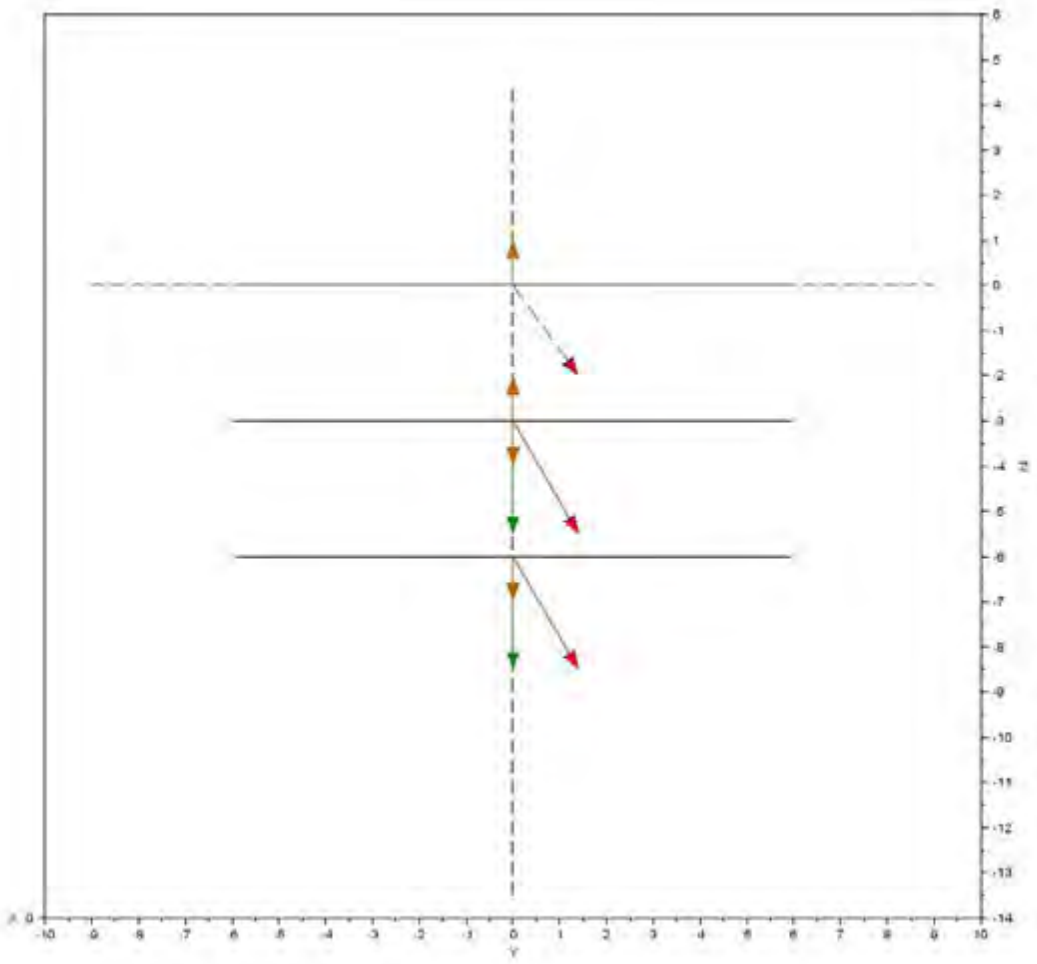

b.

Figure 32. Isometric view a. and front view b. of verification test case axial flow elements without blades or vanes.

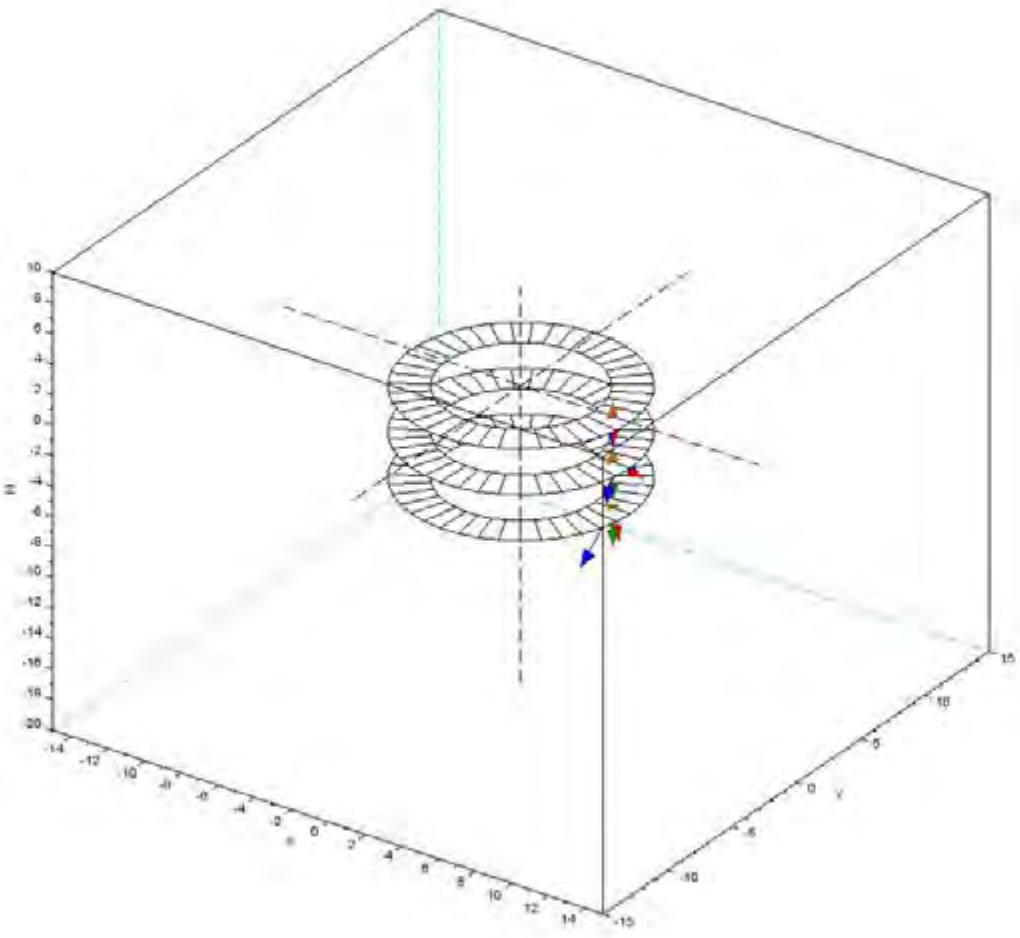

a.

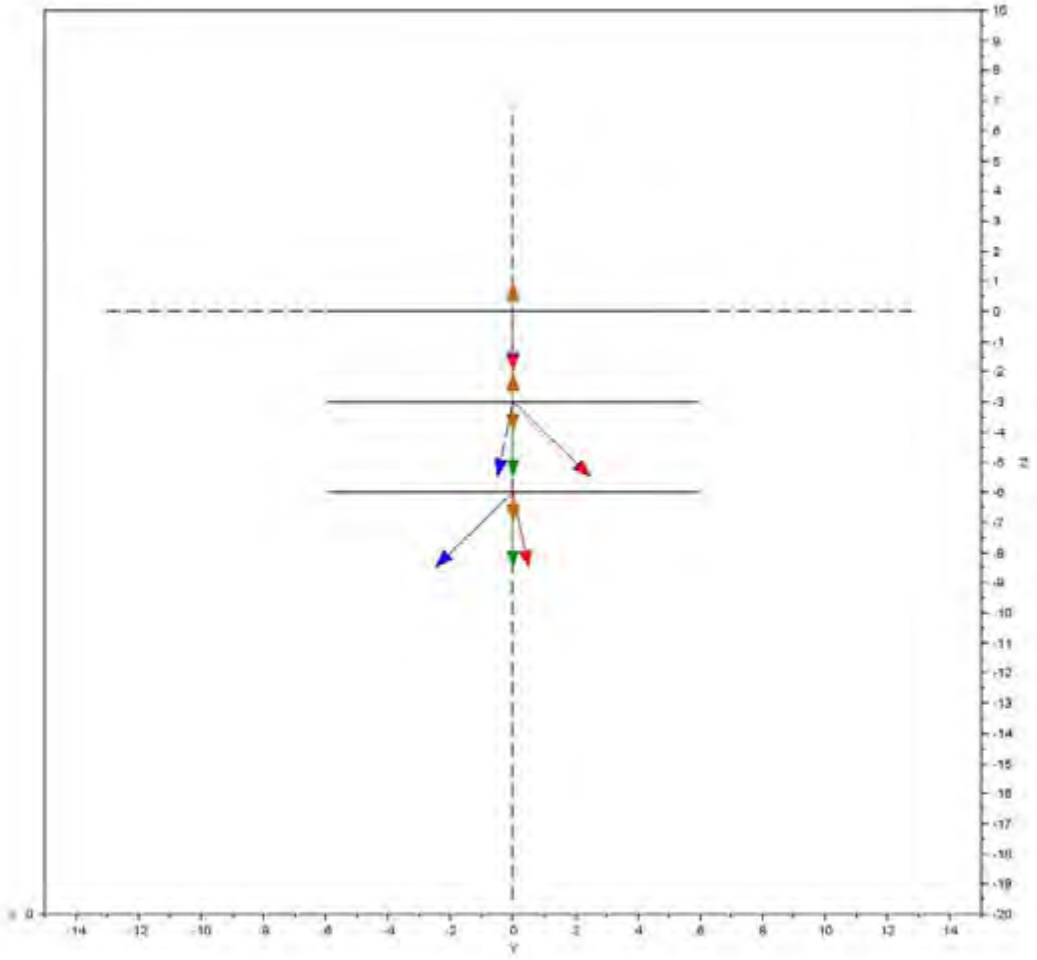

b.

Figure 33. Isometric view a. and front view b. of verification test case axial flow turbine with blades or vanes

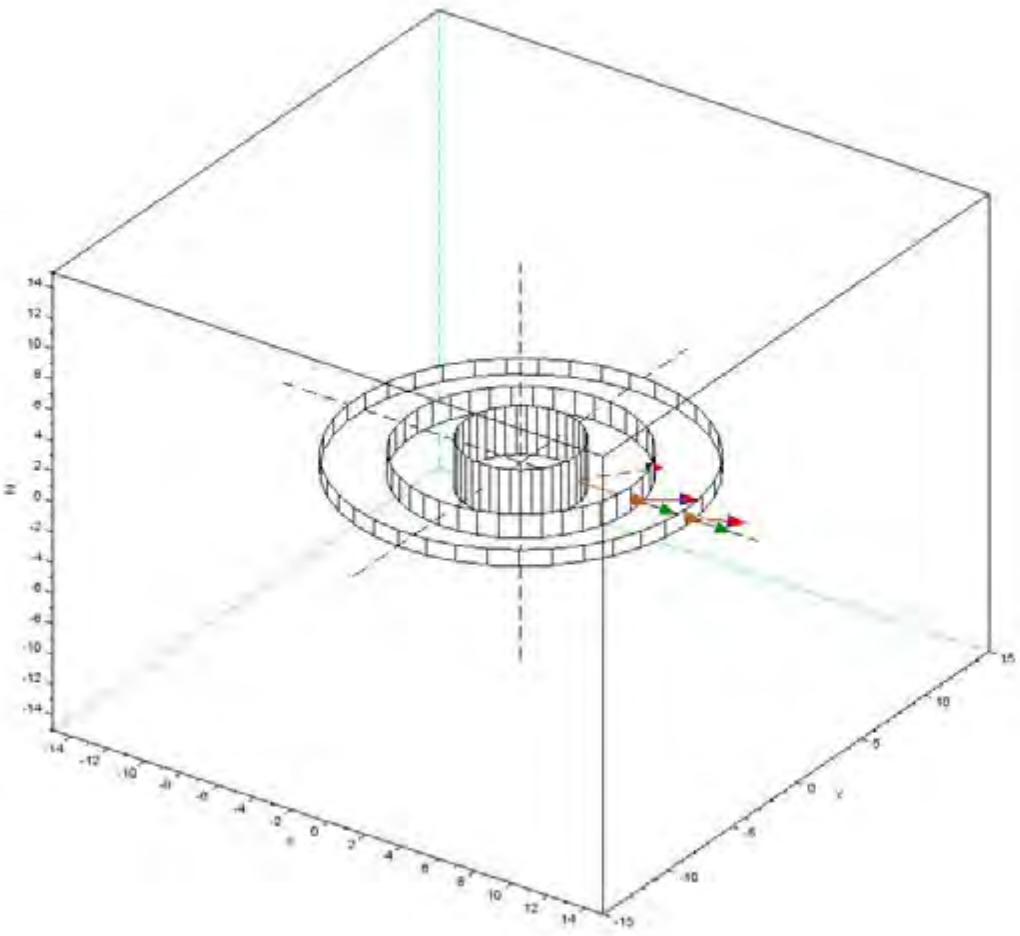

a.

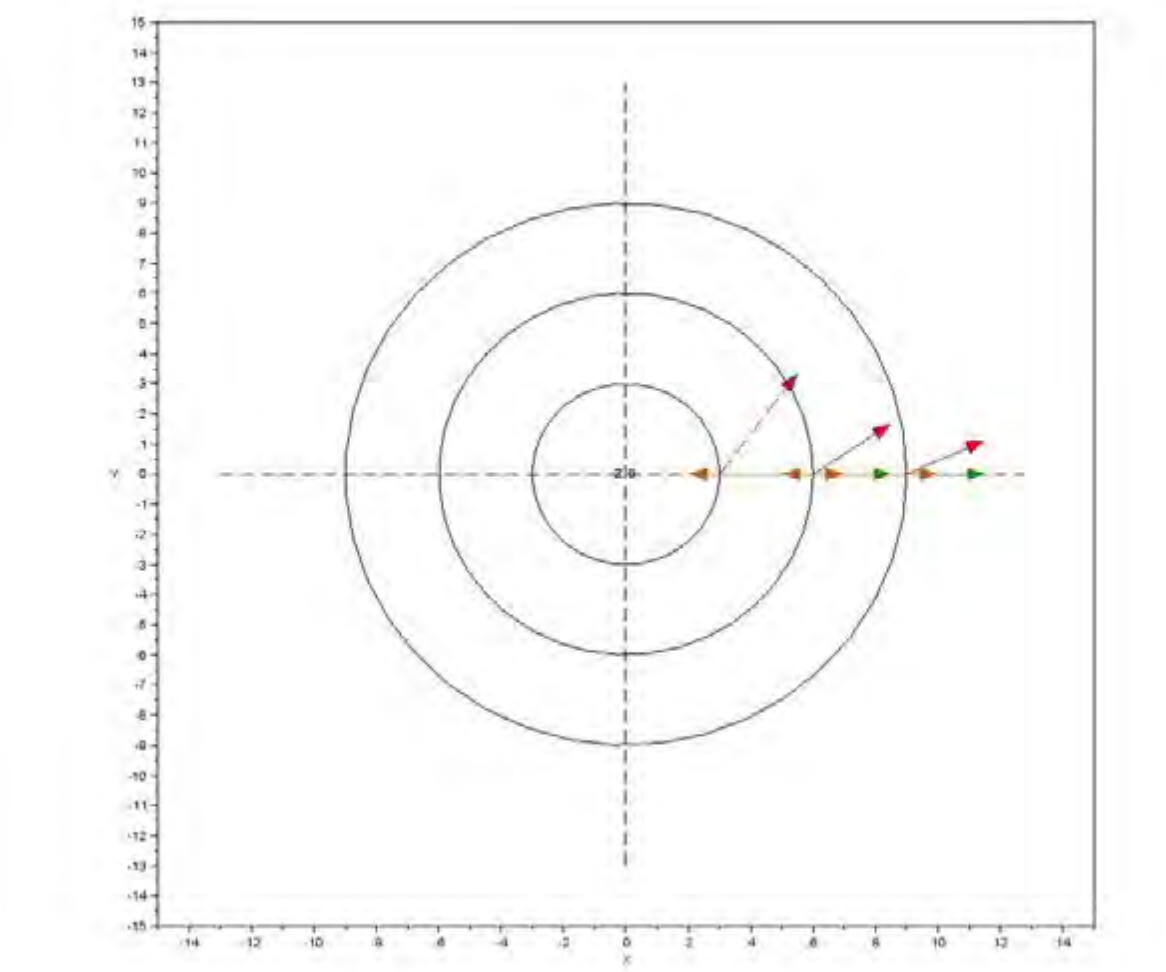

b.

Figure 34. Isometric view a. and front view b. of verification test case radial flow elements without guides or vanes.

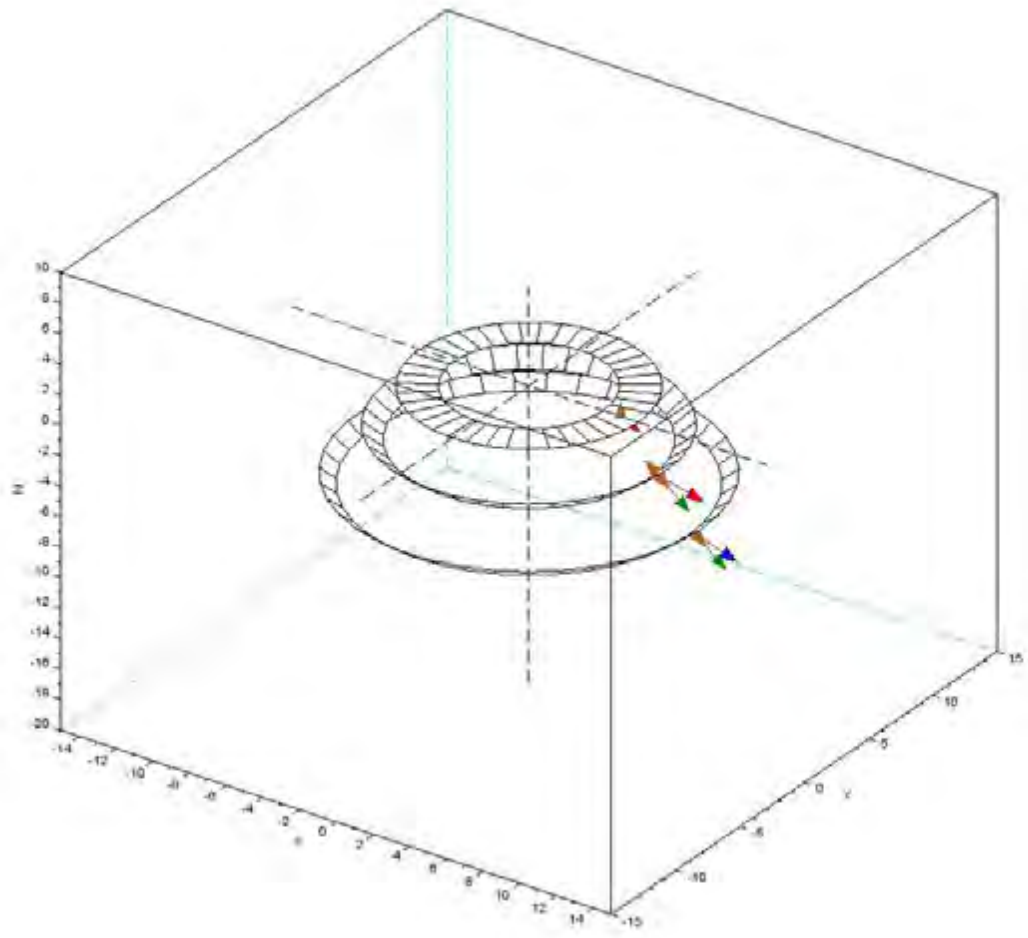

a.

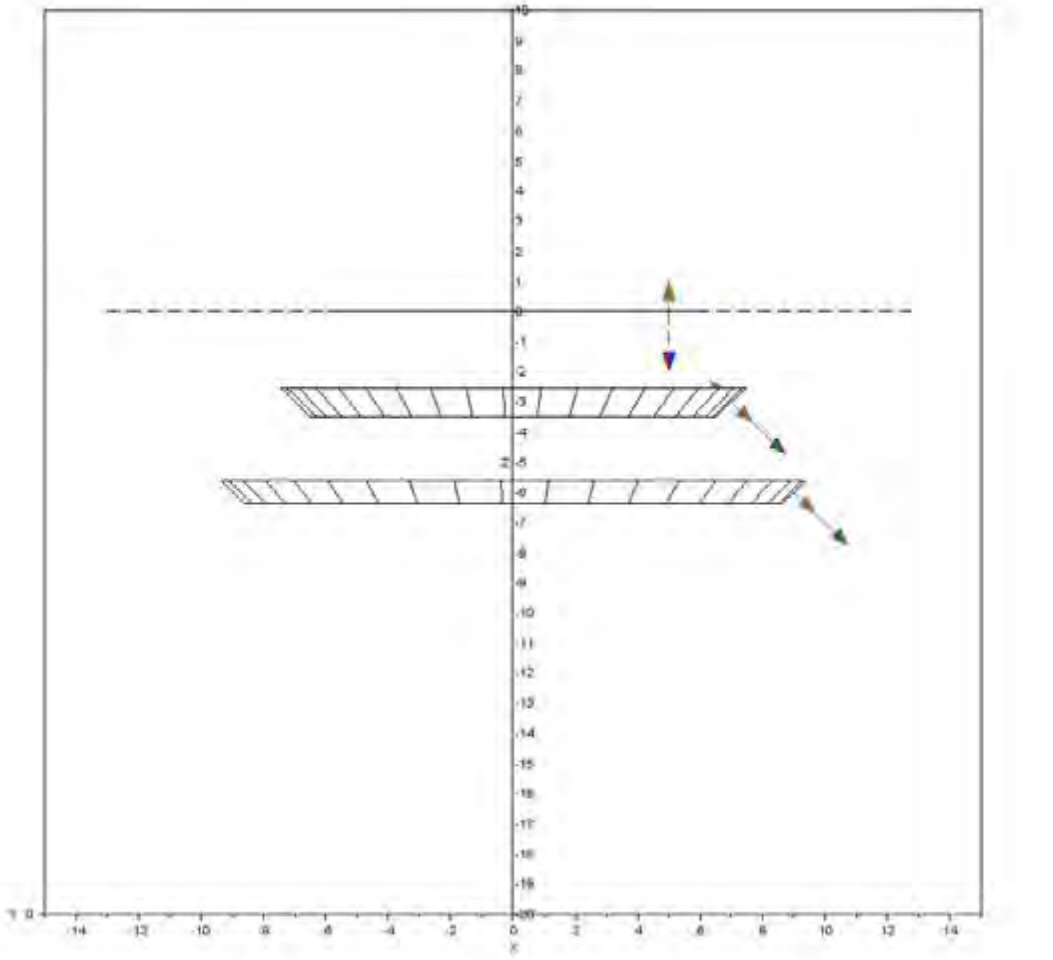

b.

Figure 35. Isometric view a. and front view b. of verification test case combined axial and radial flow.

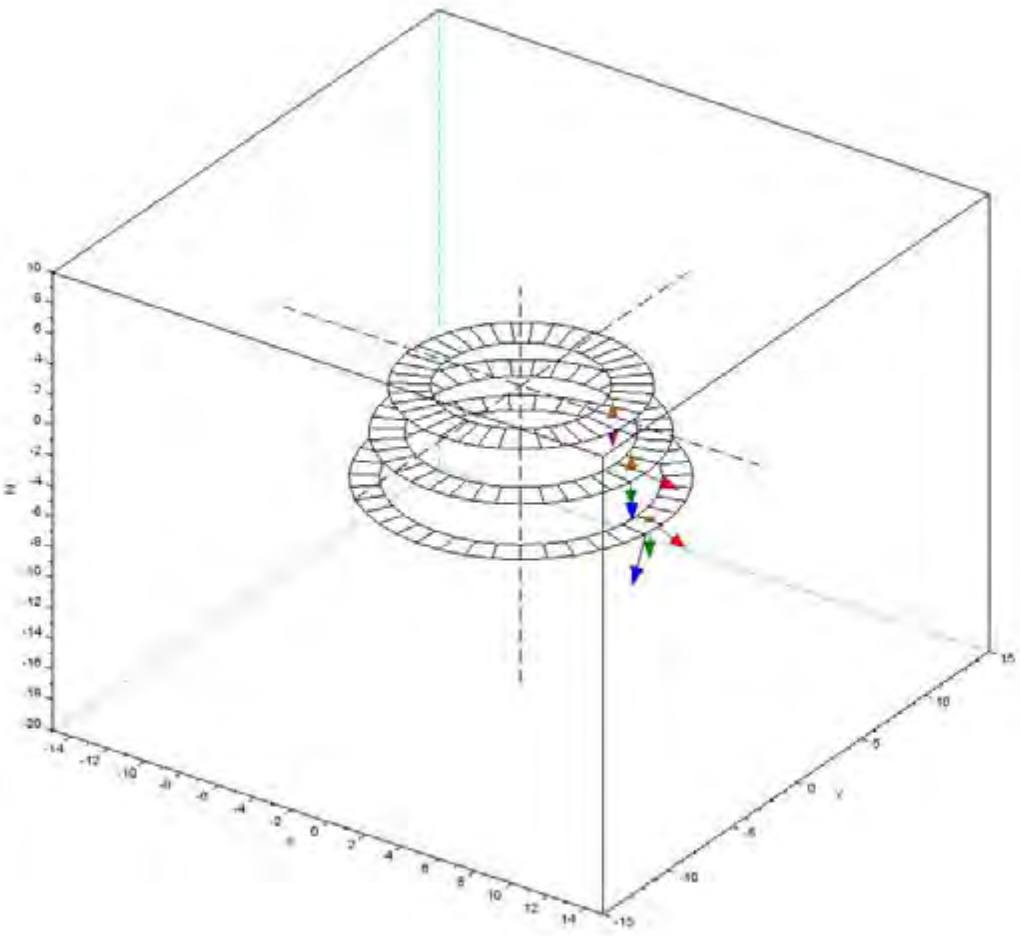

a.

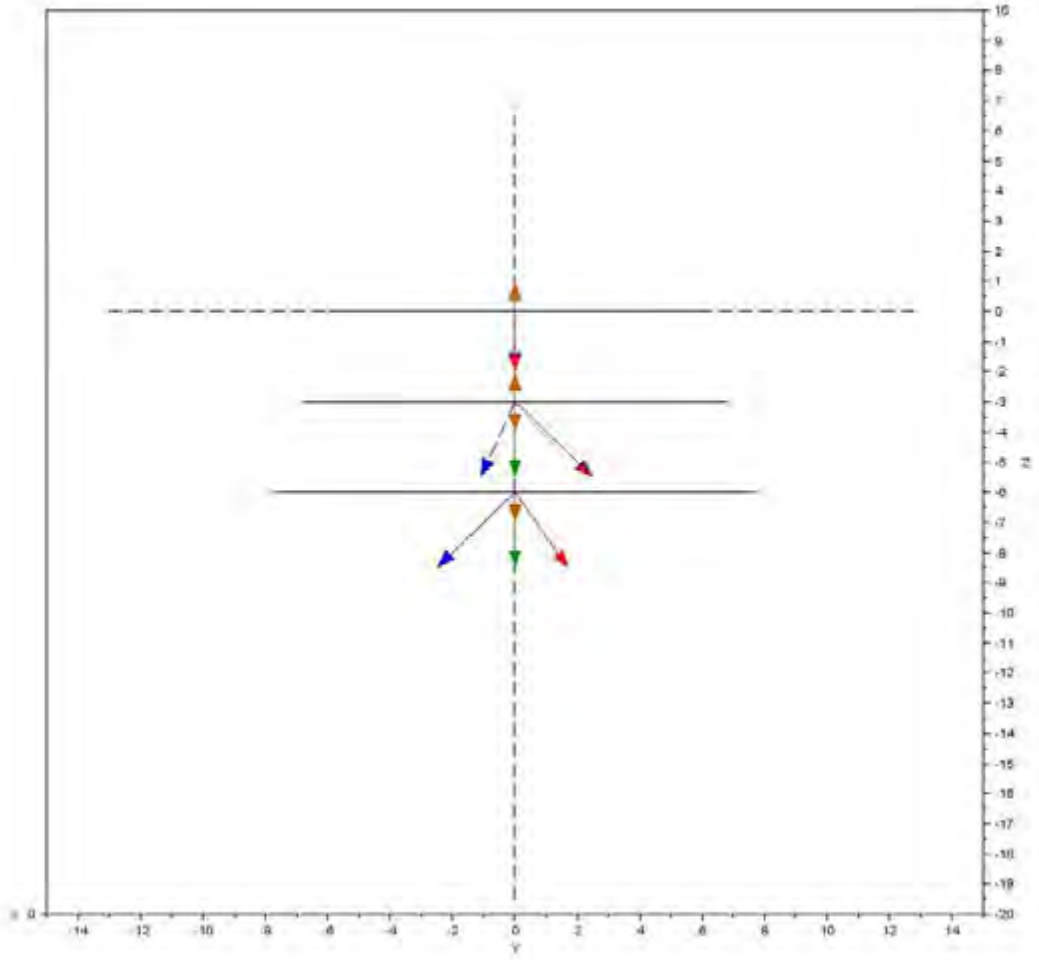

b.

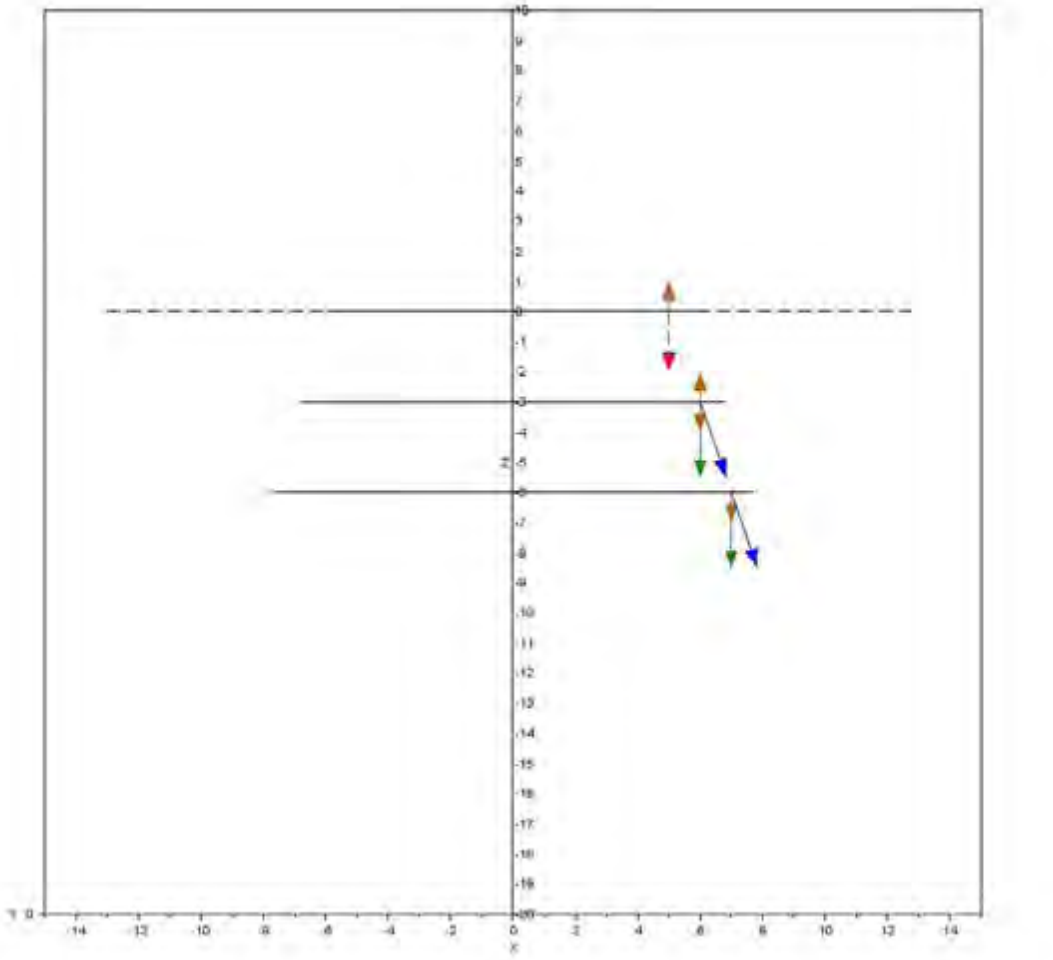

c.

Figure 36. Isometric view a. and front view b. and side view c. of verification test case axial areas with radial increase in diameter.

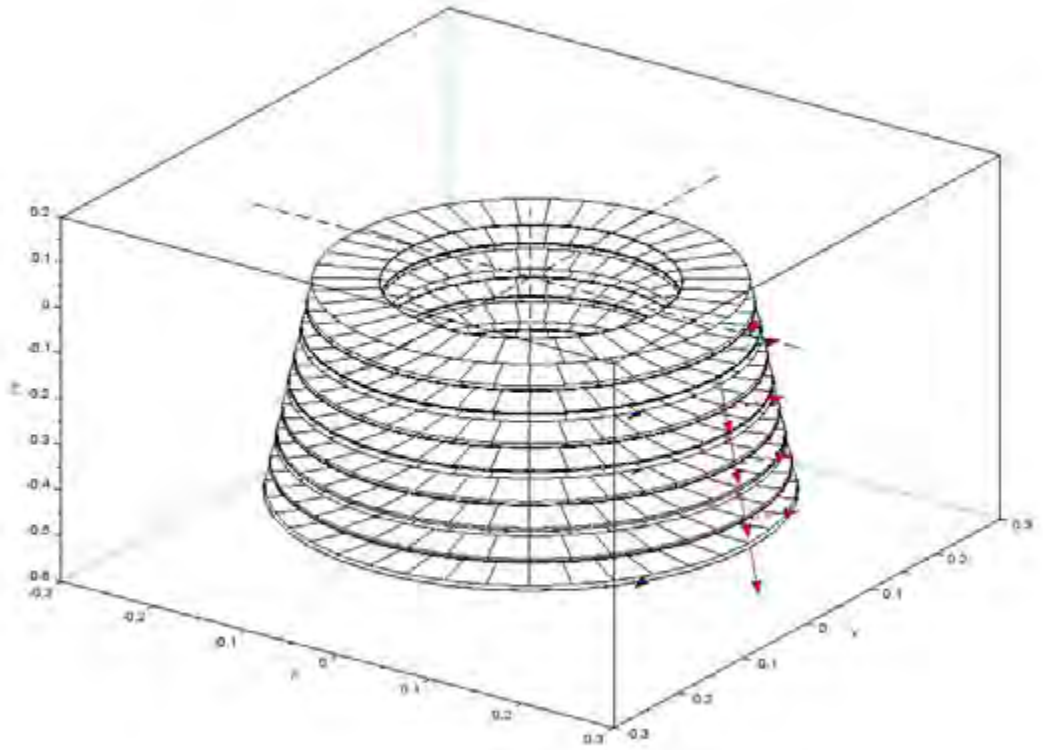

a.

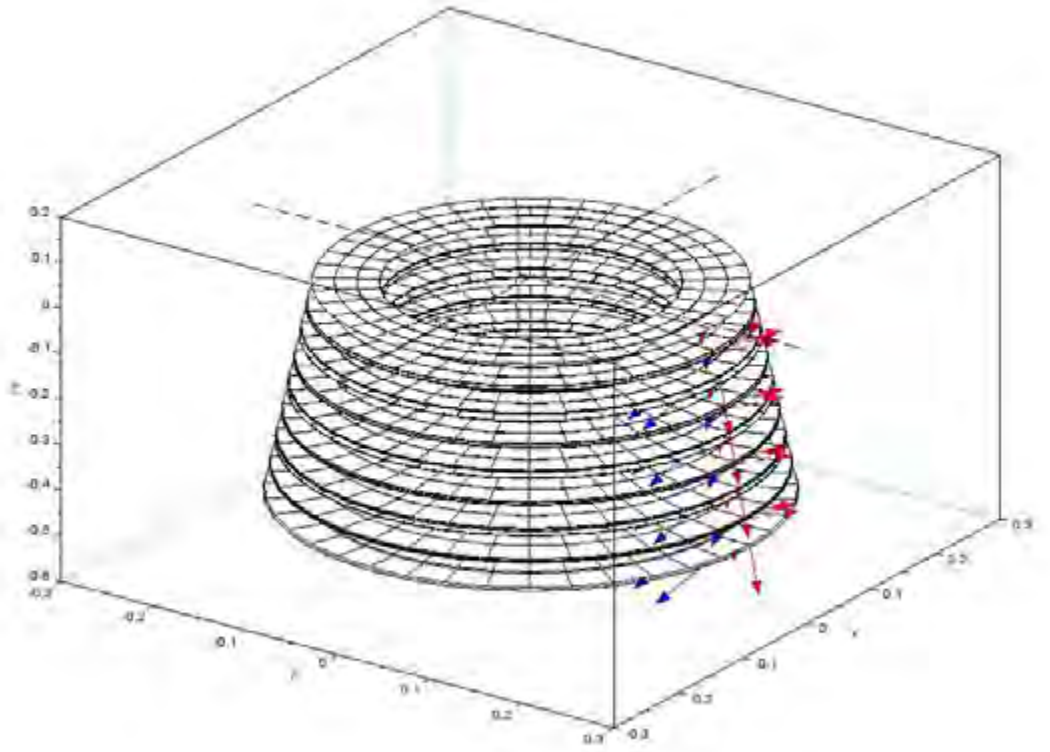

b.

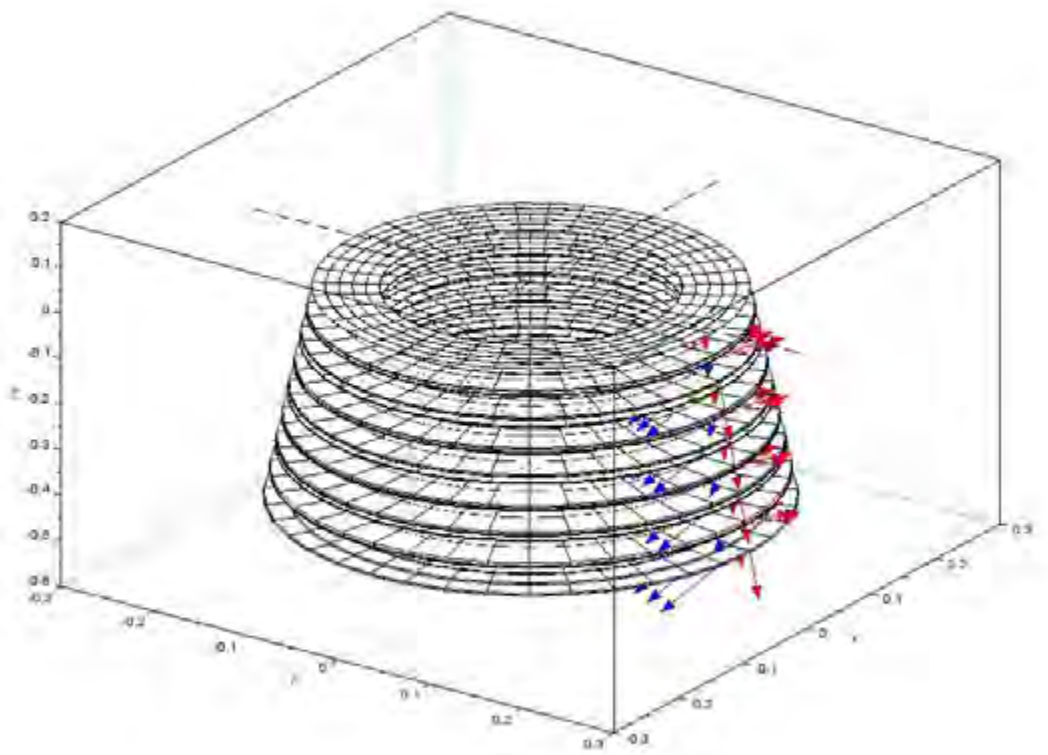

c.

Figure 43. Isometric views of simulation model 1, model 3 and model 5 with one, three and five radial elements respectively representing the stator and rotor blade passages.

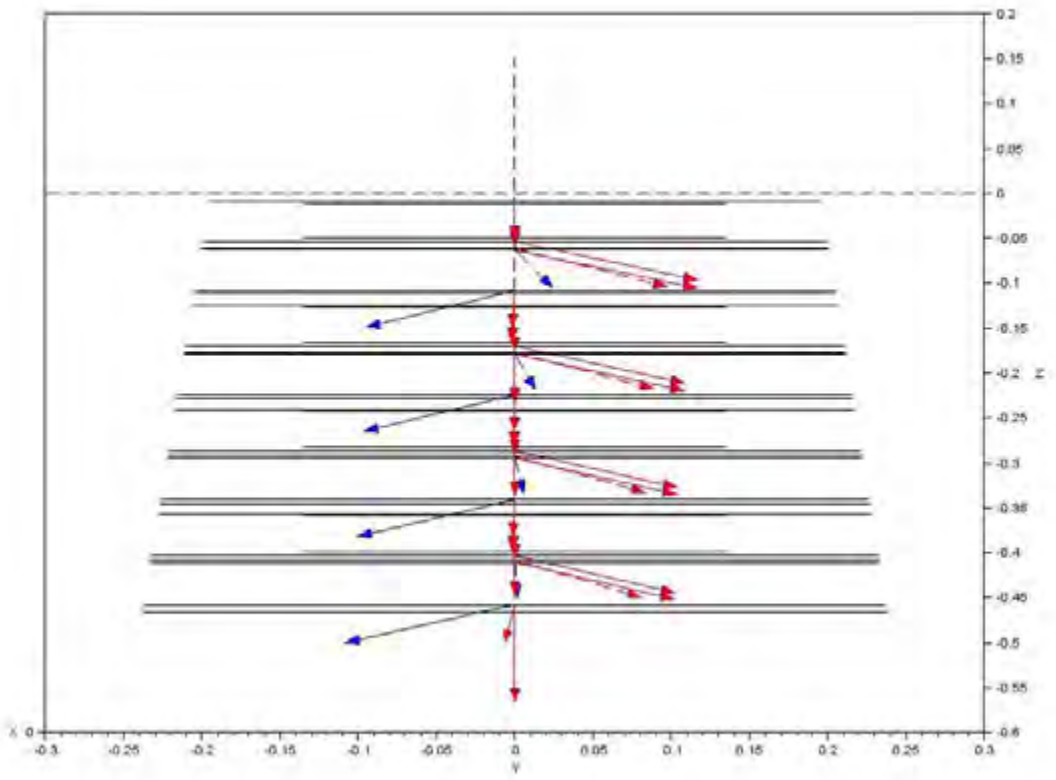
0.2
0.15
0.1
0.05
0
-0.05
-0.1
-0.15
-0.2
-0.25
-0.3
-0.35
-0.4
-0.45
-0.5
-0.55
-0.6
Z
X
0
-0.3
-0.25
-0.2
-0.15
-0.1
-0.05
0
0.05
0.1
0.15
0.2
0.25
0.3
Y

a.

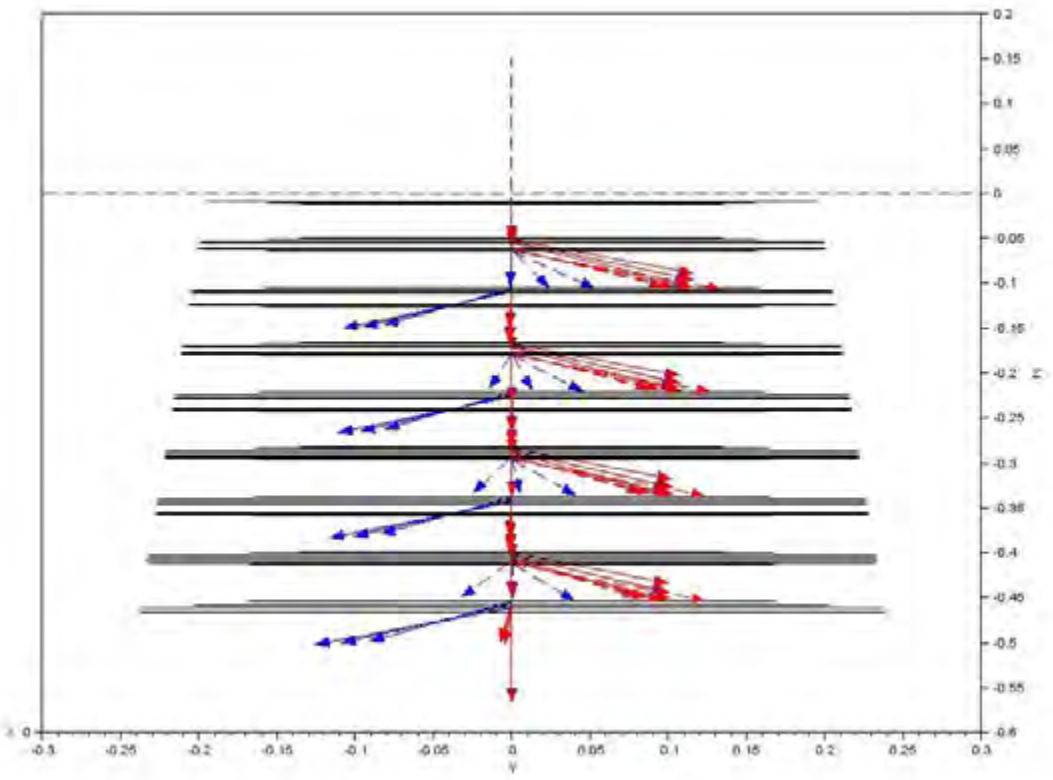
0.2
0.15
0.1
0.05
0
-0.05
-0.1
-0.15
-0.2
-0.25
-0.3
-0.35
-0.4
-0.45
-0.5
-0.55
-0.6
z
-0.3
-0.25
-0.2
-0.15
-0.1
-0.05
0
0.05
0.1
0.15
0.2
0.25
0.3
y

b.

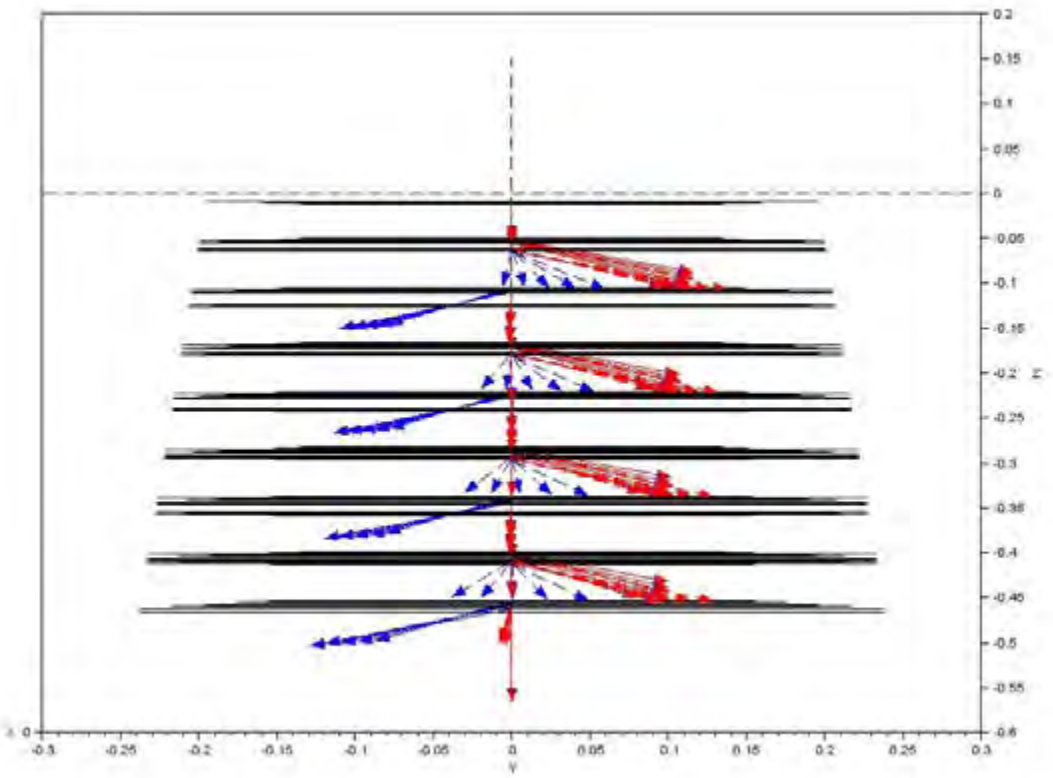

c.

Figure 44. Front views of simulation model 1, model 3 and model 5 with one, three and five radial elements respectively representing the stator and rotor blade passages.

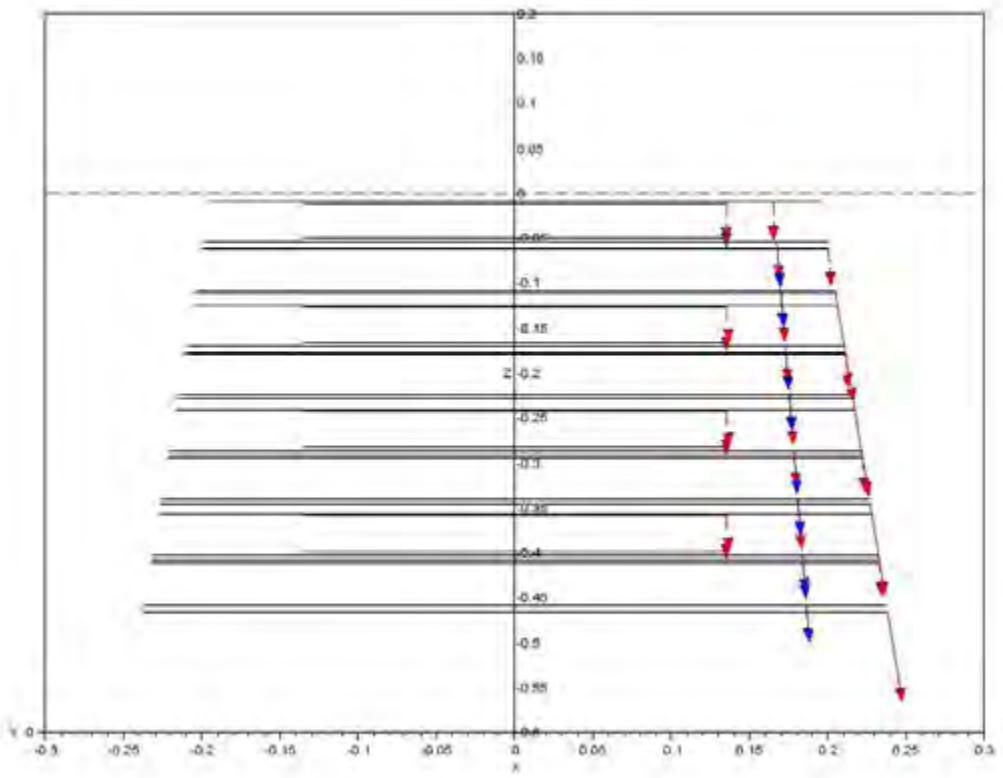
0.2
0.15
0.1
0.05
0
-0.1
-0.2
-0.25
-0.3
-0.4
-0.45
-0.5
-0.55
-0.6
Z
-0.5
-0.25
-0.2
-0.15
-0.1
-0.05
0
0.05
0.1
0.15
0.2
0.25
0.3
X

a.

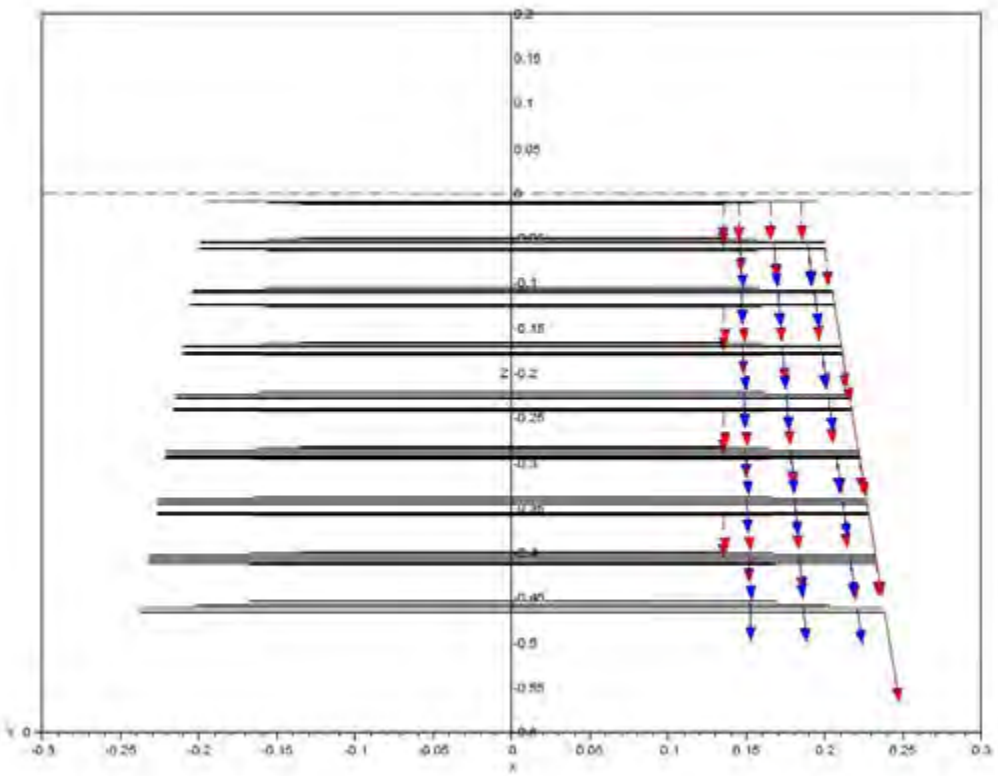
0.2
0.15
0.1
0.05
0
-0.1
-0.15
-0.2
-0.25
-0.3
-0.5
-0.55
-0.5
-0.25
-0.2
-0.15
-0.1
-0.05
0
0.05
0.1
0.15
0.2
0.25
0.3

b.

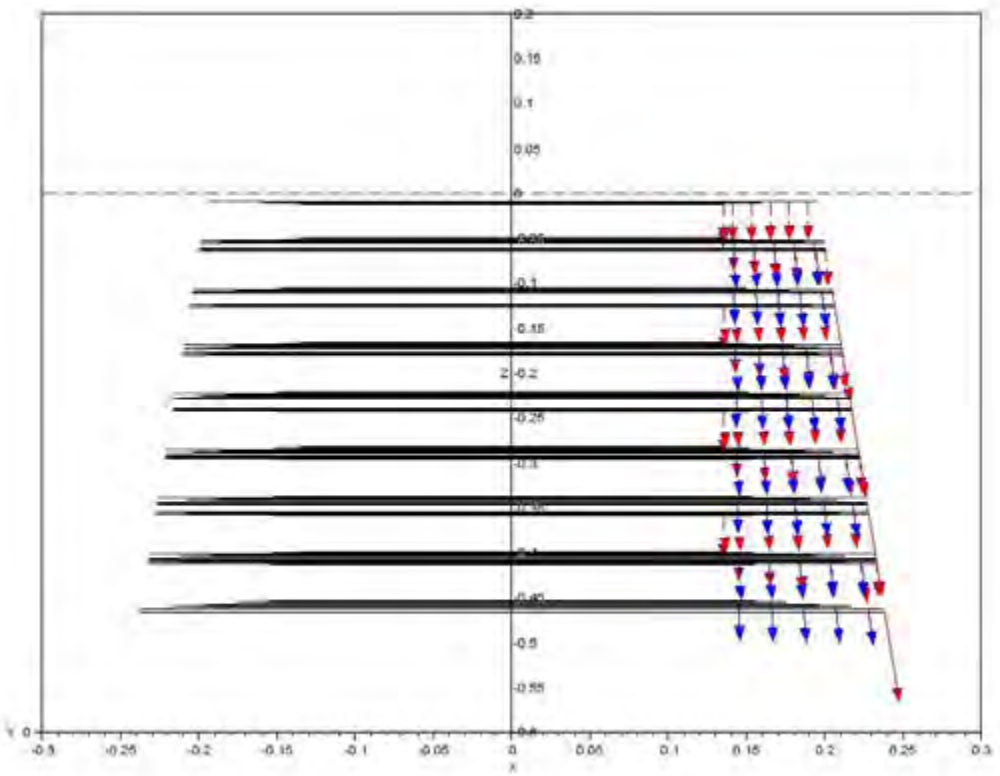

c.

Figure 45. Side views of simulation model 1, model 3 and model 5 with one, three and five radial elements respectively representing the stator and rotor blade passages.

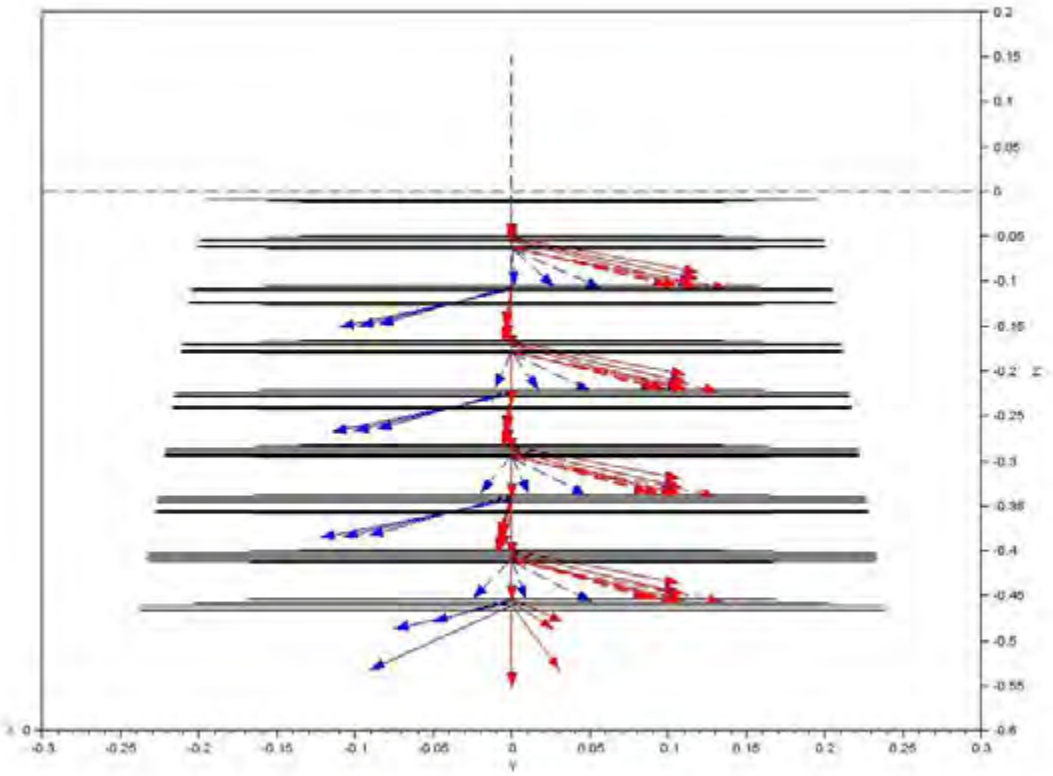

Figure 63. A front view of the simulation model with the stage 4 rotor blade outlet angle eroded in the tip region.

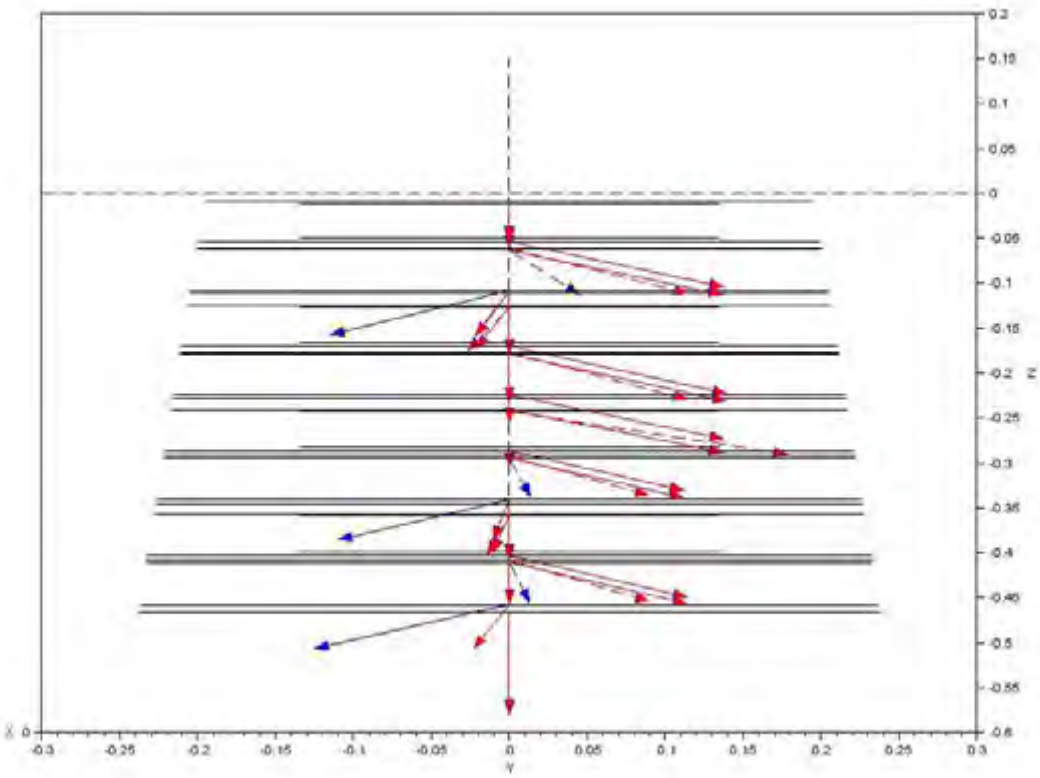

Figure 67. A front view of the simulation model with the stage 2 rotor blades removed.

Appendix D

Nominal case

Notes	Station	Table 3	AG_T3_1D	AG_T3_1D	AG_T3_1D
RPM		7500	7500	7500	7500
Rotor work		704327.3	717524.7	708041.1	708163.7
Efficiency		0.89273	0.900104	0.893035	0.89266
Mass flow rate		8.076967	8.33863	8.295197	8.299149
Total pressure	0	257431.4	257431.3	257431.3	257431.3
Total pressure	1	211625.2	208132	208195.6	208187.5
Total pressure	2	169821.5	168487.6	168493.7	168476.1
Total pressure	3	134637.3	134956.3	134906.2	134890.7
Total pressure	4	104997.9	104997.8	104997.8	104997.8
Static pressure	0	252739.4	253034	253034	253034
Static pressure	1	206533.4	204926.3	205025.7	205014.2
Static pressure	2	165560.3	165837.9	165870.4	165850
Static pressure	3	130961.9	132656.9	132628.1	132610
Static pressure	4	101275.9	102798.5	102987.3	102771.5
Total Temperature	0	404.4915	401.7643	401.7643	401.7643
Total Temperature	1	384.7176	381.078	381.2276	381.2266
Total Temperature	2	362.9873	361.1856	361.4535	361.4513

Total Temperature	3	340.3798	341.0983	341.5099	341.5125
Total Temperature	4	321.1071	319.3825	320.0603	320.0857
Absolute velocity	0	62.95709	62.95709	62.95709	62.95709
Absolute velocity	1	70.34878	58.20522	57.88026	57.91246
Absolute velocity	2	-	57.26222	56.99481	57.0286
Absolute velocity	3	70.42134	57.9353	57.7092	57.7458
Absolute velocity	4	78.42681	62.18304	59.51106	62.6178
Total enthalpy	0	409834.9	406918.3	406918.3	406918.3
Total enthalpy	1	388789.7	384941.8	385099.8	385098.8
Total enthalpy	2	365932.1	364049.3	364329.1	364326.8
Total enthalpy	3	342439.8	343182	343607.4	343610.1
Total enthalpy	4	322633	320870.1	321562.8	321588.6
Static enthalpy	0	407853.1	404936.5	404936.5	404936.5
Static enthalpy	1	386315.2	383247.9	383424.8	383421.9
Static enthalpy	2	361968	362409.8	362704.9	362700.7
Static enthalpy	3	339960.2	341503.8	341942.2	341942.8
Static enthalpy	4	319557.6	318707.8	319714.8	319211.1

Table 4

Notes	Station	Table 4	AG_T4_1D	AG_T4_3D	AG_T4_5D
RPM		7500	7500	7500	7500
Rotor work		485256.2576	444653	439042.6	439098.1
Effeciency		0.905730026	0.892326	0.885784	0.884862
Mass flow rate		7.178150143	6.764497	6.72898	6.732063
Total pressure	0	214521.2939	214521.3	214521.3	214521.3
Total pressure	1	178718.5376	177537.1	177568.7	177561.5
Total pressure	2	148806.4049	148623.4	148619.3	148604.4
Total pressure	3	124387.1879	125291.2	125256.6	125243.2
Total pressure	4	105936.7971	105936.3	105936.3	105936.3
Static pressure	0	217282.1177	210868.2	210868.2	210868.2
Static pressure	1	174036.4297	175103.3	175155.5	175146.7
Static pressure	2	145310.284	146564	146576.8	146561.1
Static pressure	3	121600.7215	123487	123468.4	123454.4
Static pressure	4	103630.5215	104291.6	104270.2	104294
Total Temperature	0	387.1348817	385.3486	385.3486	385.3486
Total Temperature	1	369.9357623	367.5266	367.6425	367.641
Total Temperature	2	351.8731792	351.358	351.5612	351.5584
Total	3	335.3664441	336.3746	336.6761	336.6771

Temperature					
Total Temperature	4	322.1969689	322.174	322.6497	322.6708
Absolute velocity	0	61.56261749	61.56262	61.56262	61.56262
Absolute velocity	1	71.91750744	53.90997	53.68384	53.70298
Absolute velocity	2	66.75671994	52.99608	52.79197	52.80657
Absolute velocity	3	63.34342021	52.86621	52.66035	52.67265
Absolute velocity	4	61.60356082	53.72116	54.1257	53.71452
Total enthalpy	0	391349.7355	389457.7	389457.7	389457.7
Total enthalpy	1	373210.8628	370683.9	370805.5	370803.9
Total enthalpy	2	354347.1639	353811.8	354023	354020
Total enthalpy	3	337268.5735	338307.4	338618.2	338619.2
Total enthalpy	4	323747.8815	323724.3	324211.1	324232.8
Static enthalpy	0	389454.7576	387562.7	387562.7	387562.7
Static enthalpy	1	370624.7989	369230.8	369364.5	369361.9
Static enthalpy	2	352118.9341	352407.6	352629.5	352625.8
Static enthalpy	3	335262.3791	336910	337231.6	337232
Static enthalpy	4	321850.3822	322126.6	322757.8	322520

Table 5

Notes	Station	Table 5	AG_T5_1D	AD_T5_3D	AG_T5_5D
RPM		7500	7500	7500	7500
Rotor work		201650.7748	194365.8	191675.4	191643.2
Effeciency		0.844399273	0.846331	0.838925	0.832381
Mass flow rate		4.988230589	4.909468	4.881865	4.883948
Total pressure	0	164557.1618	164557.2	164557.2	164557.2
Total pressure	1	142705.6889	141510.1	141554.2	141546.2
Total pressure	2	125058.6977	124603.1	124687.8	124673.5
Total pressure	3	112213.1992	112544.2	112621.5	112606.7
Total pressure	4	104546.1667	104546.3	104546.3	104546.3
Static pressure	0	162033.0303	162225	162225	162225
Static pressure	1	139508.4894	139579.6	139634.7	139627.1
Static pressure	2	122331.42	122699.7	122801.8	122788.9
Static pressure	3	109486.4171	110532.3	110642	110628.4
Static pressure	4	101147.9718	102230.6	102432.4	102299.8
Total Temperature	0	362.6398509	361.9193	361.9193	361.9193
Total Temperature	1	349.8775382	348.4907	348.5736	348.571
Total Temperature	2	337.6626748	337.6821	337.8366	337.8325
Total	3	328.4221611	329.3752	329.5996	329.6005

Temperature					
Total Temperature	4	323.5604249	323.6407	323.9603	323.9831
Absolute velocity	0	54.3993784	54.39938	54.39938	54.39938
Absolute velocity	1	64.70283615	52.36731	52.21504	52.21096
Absolute velocity	2	62.67340379	54.56495	54.30556	54.28915
Absolute velocity	3	65.24584599	58.3231	57.84873	57.83465
Absolute velocity	4	75.18984355	64.40263	61.55456	63.4458
Total enthalpy	0	365568.8156	364815.7	364815.7	364815.7
Total enthalpy	1	352274.3899	350835.3	350921.3	350918.5
Total enthalpy	2	339635.4463	339655.5	339814.8	339810.6
Total enthalpy	3	330127.763	331106.3	331336.7	331337.6
Total enthalpy	4	325143.5043	325225.7	325553	325576.3
Static enthalpy	0	364089.1695	363336.1	363336.1	363336.1
Static enthalpy	1	350181.1614	349464.1	349558.1	349555.5
Static enthalpy	2	337671.4685	338166.9	338340.3	338337
Static enthalpy	3	327999.2528	329405.5	329663.5	329665.2
Static enthalpy	4	322316.748	323095.4	323752.6	323373.7

Table 6

Notes	Station	Table 6	AG_T6_1D	AG_T6_3D	AG_T6_5D
RPM		7500	7500	7500	7500
Rotor work		124972.5774	130798.6	128697.7	128636.4
Effeciency		0.758136355	0.807567	0.798654	0.787731
Mass flow rate		4.256733773	4.309313	4.282972	4.28476
Total pressure	0	149683.8311	149683.8	149683.8	149683.8
Total pressure	1	132449.7377	130925	131000.1	130991.8
Total pressure	2	118968.0771	117748.4	117888.4	117874.5
Total pressure	3	109600.4228	109216.4	109334.4	109321.7
Total pressure	4	104755.5897	104756.1	104756.1	104756.1
Static pressure	0	147730.4387	147860.9	147860.9	147860.9
Static pressure	1	129440.8705	129048	129131.9	129124.6
Static pressure	2	116207.4061	115757.5	115917.6	115905.6
Static pressure	3	106905.681	106951.3	107113.1	107100.9
Static pressure	4	100811.7462	101965.9	102327.3	102070.7
Total Temperature	0	357.1821227	356.6572	356.6572	356.6572
Total Temperature	1	346.4776694	344.9575	345.0388	345.0357
Total Temperature	2	337.3441703	336.1782	336.3355	336.3315
Total	3	330.7017329	330.2567	330.4765	330.4805

Temperature					
Total Temperature	4	328.797838	327.2965	327.5927	327.6189
Absolute velocity	0	50.04203144	50.04203	50.04203	50.04203
Absolute velocity	1	64.66405313	53.41821	53.28213	53.26916
Absolute velocity	2	64.80721074	57.29426	56.9814	56.95744
Absolute velocity	3	66.05316867	62.93705	62.3084	62.30539
Absolute velocity	4	81.73857761	71.08165	66.3221	69.73987
Total enthalpy	0	359872.2159	359325.2	359325.2	359325.2
Total enthalpy	1	348748.2303	347173.7	347257.9	347254.6
Total enthalpy	2	339306.9736	338105	338267.1	338263
Total enthalpy	3	332469.0341	332011.7	332237.5	332241.7
Total enthalpy	4	330513.4202	328972.7	329276.5	329303.4
Static enthalpy	0	358620.1134	358073.1	358073.1	358073.1
Static enthalpy	1	346657.5104	345746.9	345838.4	345835.8
Static enthalpy	2	337206.9863	336463.7	336643.7	336640.9
Static enthalpy	3	330287.5236	330031.2	330296.4	330300.7
Static enthalpy	4	327172.8226	326421.9	327208.1	326692

Table 7

Notes	Station	Table 7	AG_T7_1D	AG_T7_3D	AG_T7_5D
RPM		5625	5625	5625	5625
Rotor work		307567.2559	308994.9	304412.3	304391.9
Effeciency		0.893642787	0.908039	0.900645	0.900269
Mass flow rate		5.806869722	5.796169	5.758161	5.760093
Total pressure	0	186890.2616	186890.3	186890.3	186890.3
Total pressure	1	160362.8234	158709	158768.7	158763.8
Total pressure	2	136832.192	136793.1	136822.5	136810
Total pressure	3	118581.2129	119285.2	119271.5	119258.9
Total pressure	4	104951.3867	104951.5	104951.5	104951.5
Static pressure	0	183847.8727	184056.6	184056.6	184056.6
Static pressure	1	157024.2878	156620.5	156724	156717.7
Static pressure	2	134254.7092	135244.3	135299.7	135285.8
Static pressure	3	116739.7849	118067.3	118069.9	118056.3
Static pressure	4	103510.6425	103919.7	103954.4	103913.9
Total Temperature	0	373.3905428	372.24	372.24	372.24
Total Temperature	1	358.8668545	357.2781	357.4256	357.4297
Total Temperature	2	345.2229896	343.8904	344.1172	344.1216
Total	3	332.174963	331.797	332.1037	332.1121

Temperature					
Total Temperature	4	322.3204782	320.8017	321.2358	321.2566
Absolute velocity	0	57.07370916	57.07371	57.07371	57.07371
Absolute velocity	1	63.01635155	52.07295	51.52086	51.54089
Absolute velocity	2	59.04371534	47.37137	46.98127	47.00442
Absolute velocity	3	52.57907271	44.17791	43.90277	43.92389
Absolute velocity	4	48.72357419	42.61536	41.92544	42.76055
Total enthalpy	0	376840.3677	375630.9	375630.9	375630.9
Total enthalpy	1	361628.8674	359972.3	360126	360130.2
Total enthalpy	2	347448.5637	346069.2	346303.8	346308.4
Total enthalpy	3	333983.5969	333594.9	333910.3	333918.9
Total enthalpy	4	323874.2654	322320.7	322764.6	322785.9
Static enthalpy	0	375211.6636	374002.2	374002.2	374002.2
Static enthalpy	1	359643.3371	358616.5	358798.8	358802
Static enthalpy	2	345705.4836	344947.2	345200.2	345203.7
Static enthalpy	3	332601.3175	332619	332946.5	332954.3
Static enthalpy	4	322687.2721	321289.6	321858.4	321657.9

Table 8

Notes	Station	Table 8	AG_T8_1D	AG_T8_3D	AG_T8_5D
RPM		5625	5625	5625	5625
Rotor work		129127.1635	145975.3	143951.5	143961.1
Effeciency		0.84728535	0.892562	0.885632	0.883017
Mass flow rate		4.139866782	4.254087	4.227207	4.228892
Total pressure	0	147746.4769	151289.4	151289.4	151289.4
Total pressure	1	131784.2847	133415.4	133441.7	133439.2
Total pressure	2	118618.8306	120127	120134.9	120128.1
Total pressure	3	108557.1102	110191.9	110188.3	110181.2
Total pressure	4	102947.5618	102947	102947	102947
Static pressure	0	146159.8421	149545.7	149545.7	149545.7
Static pressure	1	129742.5719	132246.9	132286.6	132283.2
Static pressure	2	117094.2591	119151	119167.2	119160.1
Static pressure	3	116610.2628	109256.8	109262.2	109255.2
Static pressure	4	101138.8473	101923.7	101946.2	101936.8
Total Temperature	0	354.1116133	355.3771	355.3771	355.3771
Total Temperature	1	345.2653123	344.1696	344.2506	344.2506
Total Temperature	2	335.6916503	335.0157	335.1467	335.1461
Total	3	328.17463	327.7035	327.8839	327.8855

Temperature					
Total Temperature	4	323.8925755	322.1285	322.3831	322.3942
Absolute velocity	0	48.93631216	48.5891	48.5891	48.5891
Absolute velocity	1	53.56321512	41.66155	41.42221	41.43784
Absolute velocity	2	47.73354918	39.58625	39.42089	39.42826
Absolute velocity	3	46.17427768	40.01431	39.83366	39.8329
Absolute velocity	4	54.85831307	42.94621	42.49101	42.6842
Total enthalpy	0	356674.7757	357992	357992	357992
Total enthalpy	1	347492.3898	346358	346441.9	346441.9
Total enthalpy	2	337603.6122	336907.2	337042.2	337041.6
Total enthalpy	3	329873.6964	329390.3	329575.3	329577
Total enthalpy	4	325483.6359	323677.8	323938.4	323949.7
Static enthalpy	0	355477.3943	356811.5	356811.5	356811.5
Static enthalpy	1	346057.8808	345490.2	345584	345583.4
Static enthalpy	2	336464.3663	336123.7	336265.2	336264.3
Static enthalpy	3	328807.6645	328589.7	328781.9	328783.7
Static enthalpy	4	323978.9186	322694.6	323059.8	322924.5

Table 9

Notes	Station	Table 9	AG_T9_1D	AG_T9_3D	AG_T9_5D
RPM		5625	5625	5625	5625
Rotor work		82033.87599	79480.01	78290.23	78286.35
Effeciency		0.82502684	0.84628	0.838702	0.831619
Mass flow rate		3.481909316	3.39191	3.369269	3.370649
Total pressure	0	134231.4928	134238.9	134238.9	134238.9
Total pressure	1	121775.6586	121595.6	121618.8	121614.6
Total pressure	2	112763.3103	112641.4	112679.1	112670.9
Total pressure	3	106587.9068	106582.5	106617.1	106608.1
Total pressure	4	102988.423	102988.2	102988.2	102988.2
Static pressure	0	132620.7846	132881.7	132881.7	132881.7
Static pressure	1	120588.3849	120660.4	120690.1	120685.8
Static pressure	2	111329.9446	111699.2	111744.3	111736.5
Static pressure	3	105105.4559	105504.7	105555.5	105547.2
Static pressure	4	101066.3811	101638.2	101782.7	101677.1
Total Temperature	0	358.656077	355.7411	355.7411	355.7411
Total Temperature	1	349.3605523	346.9385	347.0014	346.9999
Total Temperature	2	343.0485254	340.3527	340.4589	340.4563
Total	3	337.9951633	335.7764	335.9213	335.9212

Temperature					
Total Temperature	4	335.9297792	333.1035	333.2936	333.304
Absolute velocity	0	45.51921984	45.51922	45.51922	45.51922
Absolute velocity	1	43.58662732	39.19042	39.05259	39.05578
Absolute velocity	2	48.26421705	40.48679	40.32583	40.31611
Absolute velocity	3	49.95672178	44.22688	43.89483	43.88203
Absolute velocity	4	57.73888765	50.18288	47.42607	49.46016
Total enthalpy	0	361409.0034	358371	358371	358371
Total enthalpy	1	351737.7853	349225.8	349291	349289.5
Total enthalpy	2	345198.1887	342411.8	342521.5	342518.9
Total enthalpy	3	339978.399	337691	337840.2	337840.1
Total enthalpy	4	337848.9769	334938.8	335134.4	335145.1
Static enthalpy	0	360373.0037	357335	357335	357335
Static enthalpy	1	350787.8883	348457.9	348528.4	348526.8
Static enthalpy	2	344033.4714	341592.2	341708.4	341706.2
Static enthalpy	3	338730.5619	336713	336876.8	336877.3
Static enthalpy	4	336182.0873	333654.1	334051.7	333836.6

Appendix E Ethics in research assessment

Application for Approval of Ethics in Research (EIR) Projects
Faculty of Engineering and the Built Environment, University of Cape Town

APPLICATION FORM

Please Note:
Any person planning to undertake research in the Faculty of Engineering and the Built Environment (EBE) at the University of Cape Town is required to complete this form **before** collecting or analysing data. The objective of submitting this application prior to embarking on research is to ensure that the highest ethical standards in research, conducted under the auspices of the EBE Faculty, are met. Please ensure that you have read and understood the **EBE Ethics in Research Handbook** (available from the UCT EBE, Research Ethics website) prior to completing this application form: http://www.ebe.uct.ac.za/uct/ebe/researchethics.pdf

APPLICANT'S DETAILS		
Name of principal researcher, student or external applicant:		Roelof Pottas
Department:		Mechanical Engineering
Preferred email address of applicant:		potsen1@gmail.com
If a Student:	Your Degree: e.g., MSc, PhD, etc.,	MSc
	Name of Supervisor (if supervised):	Prof PG Rousseau
If this is a research contract, indicate the source of funding/sponsorship:		
Project Title:		A row-by-row axial turbine process model based on a one-dimensional thermofluid network approach

I hereby undertake to carry out my research in such a way that:

- there is no apparent legal objection to the nature or the method of research; and
- the research will not compromise staff or students or the other responsibilities of the University;
- the stated objective will be achieved, and the findings will have a high degree of validity;
- limitations and alternative interpretations will be considered;
- the findings could be subject to peer review and publicly available; and
- I will comply with the conventions of copyright and avoid any practice that would constitute plagiarism.

SIGNED BY	Full name	Signature	Date
Principal Researcher/ Student/External applicant	Roelof Pottas		**26 Aug 2016**

APPLICATION APPROVED BY	Full name	Signature	Date
Supervisor (where applicable)	Prof PG Rousseau		26/08/2016
HOD (or delegated nominee) Final authority for all applicants who have answered NO to all questions in Section1; and for all Undergraduate research (including Honours).	Tunde Bello-Ochende		30/08/2016
Chair: Faculty EIR Committee For applicants other than undergraduate students who have answered YES to any of the above questions.			

Page 1 of 1